STIMULI-RESPONSIVE NANOMATERIALS FOR CONTROLLED DELIVERY BY LIGHT, MAGNETIC AND ELECTRICAL TRIGGERS

Meng Bi Zhang

December 2017

Australian National University

A thesis submitted for the degree of Doctor of Philosophy of
The Australian National University

Declaration

I certify that this thesis does not include any material that has previously been submitted for a degree in any university. To the best of my knowledge, it does not contain any material previously published or written by another person except where due and clear reference is made in the text. The work in this thesis is my own, except for the contributions made by others as described in the Acknowledgements.

Meng Bi Zhang

12th of December, 2017

Word Count: 42,295

This work is dedicated to the wonderful teachers I have had over the years, from Mrs. H through to Prof. L, and with special mention to my mother for being the first.

Acknowledgements

This accomplishment does not belong to me alone. I owe much and more to the following fine folk.

First and foremost, I thank the many wiser minds who aided me along the way. The road was often long and winding, and some days it seemed to go uphill on both sides. In particular, Dr Antonio Tricoli, thank you for giving me the freedom and support to pursue my many ideas, even the mad ones. Especially the mad ones. In the end, we did some fascinating science together.

Secondly, I thank the many collaborators who made this work possible. It was a privilege to have worked with you. Special thanks must go to the many technicians who helped along the way. Many of the most interesting results presented here would have been impossible without your time, expertise and patience.

Thirdly, I thank my immediate colleagues in the Nanotechnology Research Group. Your company made the good times much more enjoyable and the bad times almost tolerable. Special mention goes to Noushin Nasiri who was there since the beginning. We battled many dragons together.

I would like to acknowledge the Australian government for giving me food to eat and a roof to sleep under for the duration. Without such funding, the work may indeed have happened, but I would surely be poorer, colder, thinner, and sadder.

To my friends good and true, thank you for keeping me sane with tea, cake, crafts and laughs. You know who you are.

And finally, to the ones who supported me from coast-to-coast, thank you for your patience in the whole affair. As the days weathered in weeks and months and years, your resolve remained strong even as my own began to crumble, and that made all the difference in the end. Your love stretched wider and warmer than the desert between us, and I am grateful every day for it.

"So long and thanks for the fish."

Abstract

The use of nanomaterials for biomedical applications is an emerging and important field. This is particularly true of advancements in targeted and controlled drug delivery, which offer several important improvements over traditional drug administration. The clinical efficacy of small-molecule therapeutics is currently limited by many factors, including: poor solubility, inefficient cellular uptake, overly rapid renal clearance and an inability to target only desired locations such as diseased tissues. The use of nanocarriers for drug delivery may greatly improve the efficacy over traditional therapeutics by lowering the total dosage, limiting the exposure to affected areas only, and giving greater temporal control over drug elution. These materials often make use of both organic and inorganic components, exploiting the unique and useful properties of each constituent to achieve novel, synergistic functions.

This dissertation presents a study of nanocomposites comprising the three most important materials in this field: titania, iron oxides and polypyrrole. Titania is a strong photocatalyst, iron oxides provide useful responses to applied magnetic fields, and polypyrrole is a polymer with unique electrochemical properties. Studies in this dissertation were aimed at combining these three materials to create a novel structure that is responsive towards light, magnetic fields and electrical stimulation to serve as an enabling platform for the loading and release of biologically interesting compounds.

These nanomaterials have been paired with amino acids L-lysine and L-glutamic acid, two organic molecules of interest due to their ability to bind to DNA and proteins, and to form prodrugs that exhibit enhanced performance compared to

traditionally administered medicines. Two model compounds have been loaded and released on these carriers: Ketoprofen, an important anti-inflammatory that is traditionally hindered by its limited cellular uptake levels; and fluorescein isothiocyanate, a fluorescent dye molecule that is a common tool used in this field for nanocarrier location and easy visualisation of release-related kinetics.

First, an investigation into the effect of pH on the binding of amino acids to titania, iron oxide and polypyrrole is presented with a view towards optimising the functionalised material for subsequent loading and release of the model drugs (in this case, amine-reactive molecules). The release mechanism of photo-activated TiO_2 is studied in detail with a particular focus on the competition between the cleavage of bonds versus organic degradation on the catalyst's surface. Both mechanisms are currently reported in literature and studies were aimed at identifying the more dominant pathway in the system developed alongside understanding the crucial role of reaction time scales on this photochemistry.

Then, the pH-tuneable flocculation of the amino acid-functionalised nanoparticles via electrostatic attractions is exploited to create a novel, anisotropic assembly of iron oxides. These filaments display a dynamic and unique response towards a rotating magnetic field by creating local microscale vortices. This motion is used to enhance local delivery rate of molecules through magnetic-field triggered microscale mixing.

Finally, this anisotropic iron oxide structure is combined with polypyrrole to create a unique, novel material that possesses directional conductivity, a photothermal response, and magnetic field-triggered release of loaded molecules at enhanced and controllable rates compared with traditional diffusion-limited systems.

Thesis Organisation

A detailed review of literature is given in ***Chapter 1 Background and Literature Review***. This comprises an introduction to metal oxide nanomaterials and their role in nanomedicine (*Section 1.2*), magnetic nanomaterials and their unique magnetic field responsive character (*Section 1.3*), synthesis of metal oxide nanomaterials (*Section 1.4*), functionalisation strategies (*Section 1.5*), intrinsically conductive polymers (*Section 1.6*), and biocompatibility (*Section 1.7*). The key research questions arising from this literature review and associated research aims are presented in *Section 1.8*. The results of experiments on the effect of pH on amino acid functionalisation of TiO_2 and Fe_3O_4 will be presented in ***Chapter 2***. ***Chapter 3*** investigates the flocculation effect of this functionalised material and presents a method to exploit this for self-assembly of Fe_3O_4 under a magnetic field to create novel, anisotropic structures. An analogous functionalisation of PPy with amino acids is presented in ***Chapter 4***. Finally, the findings of previous chapters are combined to produce a composite material of amino acid-functionalised, light-responsive, conductive and magnetically responsive material that is presented in ***Chapter 5.*** Conclusions and recommendations for future work will be presented in ***Chapter 6***. Methods and materials are given at the end of each chapter where appropriate. References will follow at the end of the document.

List of publications

Journal Papers

T. Zhang, P. Costigan, N. Varshney, A. Tricoli, *RSC Advances* **2016**, 6, 33843-33850.

T. Zhang, M. A. Go, C. Stricker, V. R. Daria, A. Tricoli, *J. Mater. Chem. B* **2015**, *3*, 1677-1687.

J. Ou, F. Wang, Y. Huang, D. Li, Y. Jiang, Q.-H. Qin, Z. Stachurski, A. Tricoli, T. Zhang, *Colloids and Surfaces B: Biointerfaces* **2014**, *117*, 466-472.

Conference Proceedings

T. Zhang, M. A. Go, C. Stricker, V. R. Daria, A. Tricoli, *Journal of Materials Chemistry B* **2015**, *3*, 1677-1687.

In Submission

K.Bruggeman, T.Zhang, A.Tricoli, D.Nisbet, *Pharmaceutical Research*, "Reverse UV-Triggered Growth Factor Delivery from TiO_2 Nanoparticles in a Self-Assembling Peptide Hydrogel"

Nomenclature

3D	Three-dimensional
AA	Amino Acid
APS	Ammonium persulfate
ATF	Amino-terminal fragment
BDNF	Bovine-derived nerve factor
BET	Brunauer, Emmett and Teller
BSA	Bovine serum albumin
DMSO	Dimethyl sulfoxide
EtOH	Ethanol
Fe_2O_3	Iron oxide, hematite phase
Fe_3O_4	Iron oxide, magnetite phase
$FeCl_3$	Iron (III) chloride
FSP	Flame Spray Pyrolysis
FTIR	Fourier Transform Infrared
Glut	(L)-Glutamic Acid
H_2O	Water
HCl	Hydrochloric Acid
HFMF	High Frequency Magnetic Field
HSA	Human serum albumin
IEP	Isoelectric Point
Lys	(L)-Lysine
NaOH	Sodium Hydroxide
NIR	Near Infrared
NPs	Nanoparticles
PAni	Polyaniline
PEDOT	Poly(3,4-ethyl-enedioxthiophene)
pK_a	Acid dissociation constant
PPy	Polypyrrole
PTX	Paclitaxel
SEM	Scanning Electron Microscopy
SiO_2	Silica, Silicon Dioxide
SnO_2	Tin Dioxide
SP	Superparamagnetic
TEM	Transmission Electron Microscopy
TiO_2	Titanium Dioxide
TMX	Tamoxifen
UV	Ultraviolet
Vis	Visible
XRD	X-ray Diffraction

Table of Contents

List of Figures

List of Tables

CHAPTER ONE

Background and Literature Review

1.1 Overview

The application of nanomaterials for biomedical applications is a field that has been gaining increasing importance in the past decade. This scientific discipline involves the design, synthesis and application of precisely engineering structures in the nano-to-microscale for novel therapeutic and diagnostic functions. This enabling technology makes use of both organic and inorganic components, exploiting the unique and useful properties of each constituent to novel, synergistic functions.

In particular, the development of such nanomaterials that are designed to undergo predetermined responses towards anticipated or applied stimuli has gained increasing importance in medicine. Such structures make use of endogenous or exogenous stimuli (or combination thereof) and translate these triggers into desirable and useful actions of some medical benefit.

Endogenous stimuli (that is, a stimulus that originates from the body itself) that are currently known include pH[1] and temperature[2] changes, or response towards particular enzymes[3]. Endogenous stimulation has the advantage of being naturally occurring, meaning no addition technology is required and there is therefore no additional health risk arising from the application of the stimulus. Additionally, changes in local pH, temperature and enzymes are often signals of important changes in biological function that may be a direct symptom of disease and is an indicator that the intervention offered by the nanomaterial is required.

On the other hand, exogenous (externally applied) stimuli are currently popular due to the greater degree of control and predictability that is afforded by such systems. Popular exogenous stimuli include light, magnetic field and ultrasound[4] (Figure 1).

These methods differ on several terms, including depth of penetration within human tissues, cost of operation, and potential side effects.

The nanocarrier is typically designed to undergo useful responses to stimulation by undergoing physical changes such as by swelling or shrinking[5] and opening or closing[6], or chemical changes such as by oxidising or reducing[7]. These responses may be used for applications such as drug release[8], photo[9] /chemo[10]/magnetotherapies[11] and directed cell growth[12].

The potential of such materials towards drug delivery is particularly significant. The clinical efficacy of traditionally administered medicine is currently limited by many factors, including: poor solubility[13], inefficient cellular uptake[14], and an inability to target only at the desired location of diseased tissues[15]. The use of nanocarriers for drug delivery may greatly improve the efficacy of treatment by addressing these issues. Tethering a pharmaceutical to a nanomaterial that can be directed to an affected site such as a tumour using, for example, a magnetic field, and then being able to control the release time and rate of the drug for maximum efficiency would represent a significant advancement.

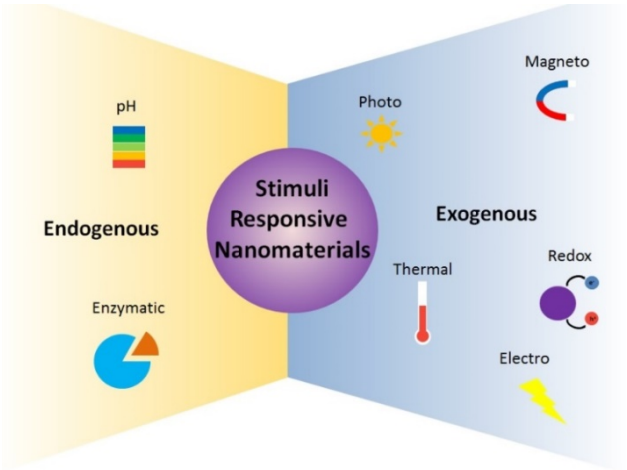

Figure 1. Overview of different endogenous and exogenous stimuli for stimulation of nanomaterials.

Over the past decade, the field has exploded with solutions of ever-increasing sophistication to achieve these aims. Here, a survey of relevant literature has been provided with a focus towards the following:

- *Material type*: Metals, ceramics, polymers and various composites of all three material classes have been proposed for these applications. This thesis will focus primarily on ceramics and polymers.
- *Synthesis strategie*s: The most prominent strategies for the synthesis of the above materials are outlined with a particular emphasis on flame-spray pyrolysis, a high-throughput solution for production of ceramic nanoparticles.
- *Functionalisation strategies*: The key methods for modifying the nanomaterial surfaces with functional organic molecules will be studied. The importance of amino acids in this role and the challenges of using them are discussed.
- *Biocompatibility issues:* Finally, a literature survey is conducted to ascertain the biocompatibility of the materials used in this thesis.

1.2 Ceramic Nanomaterials for Drug Release

Ceramic nanomaterials, particularly nanostructured metal oxides, have emerged as an important class of materials for bio-applications due to several key desirable properties. The most prominent and important ceramic nanomaterials are titanium dioxide (TiO_2), silicon dioxide (SiO_2) and iron oxides (Fe_xO_y). TiO_2, particularly in the Anatase phase, is a strong photocatalyst that has been used for light-triggered drug release[16]. SiO_2 is commonly used as an inert coating or carrier for functional

moieties[17]. Magnetic phases of iron oxides, such as magnetite (Fe_3O_4), maghemite (γ-Fe_2O_3) and hematite (α-Fe_2O_3) provide useful magnetic functionality while being inherently less toxic than other magnetic materials that contain heavy metal species (e.g. Co, Ni)[18]. The following section will discuss in detail the state-of-the-art in terms of the design, synthesis and application of TiO_2 and SiO_2. Due to the prominence of iron oxides, they are discussed separately in *Section 1.2 Magnetic Nanomaterials*.

1.2.1 Titanium dioxide the photocatalyst

Titanium dioxide is of key interest in applications such as controlled drug delivery as it is one of the strongest photocatalysts that is currently known. The photocatalytic behaviour of TiO_2 is reasonably well-understood. Upon illumination with ultraviolet light corresponding to the bandgap of TiO_2, ca. 3.05eV for anatase and 2.98eV for rutile,[19] an electron is excited from the valence band to the conductance band, generating charge carriers (electron and hole). The photogenerated holes react with water to create hydroxyl radicals and together begin to oxidise the nearby organic molecules at the particle surface (Figure 2). At the same time, electrons in the conduction band will be involved in reduction reactions with dissolved oxygen to generate peroxide.[20] This a property that has been exploited in other disciplines to great effect (e.g. solar cells, water splitting, self-cleaning coatings) and has recently been exploited in the context of drug delivery systems.[21]

$$H_2O + h^+ \rightarrow OH\cdot + H^+ \qquad \text{(Equation 1)}$$

$$O_2 + 2e^- + 2H^+ \rightarrow H_2O_2 \qquad \text{(Equation 2)}$$

Designs that use TiO_2 for drug delivery typically involve first the adsorption of functional molecules onto the TiO_2 surface (either a drug directly or via a linking

molecule), then release of this bound molecule is triggered by exploiting the photocatalytic redox events at the nanoparticle surface[22]. The mechanism behind this is not yet entirely understood. For example, although it has been widely observed that whole, undamaged organic molecules such as pharmaceuticals[23] may be delivered by this method, there have been studies suggesting that adsorbed molecules, e.g. oxalic acid, are likely to be photocatalytically decomposed when TiO_2 is exposed to light[24]. At the same time, other authors hypothesise that the redox events prefer to cleave the TiO_2-organic ligand bond first and there is therefore little decomposition recorded at shorter time frames such as is typically required for drug release.[25]

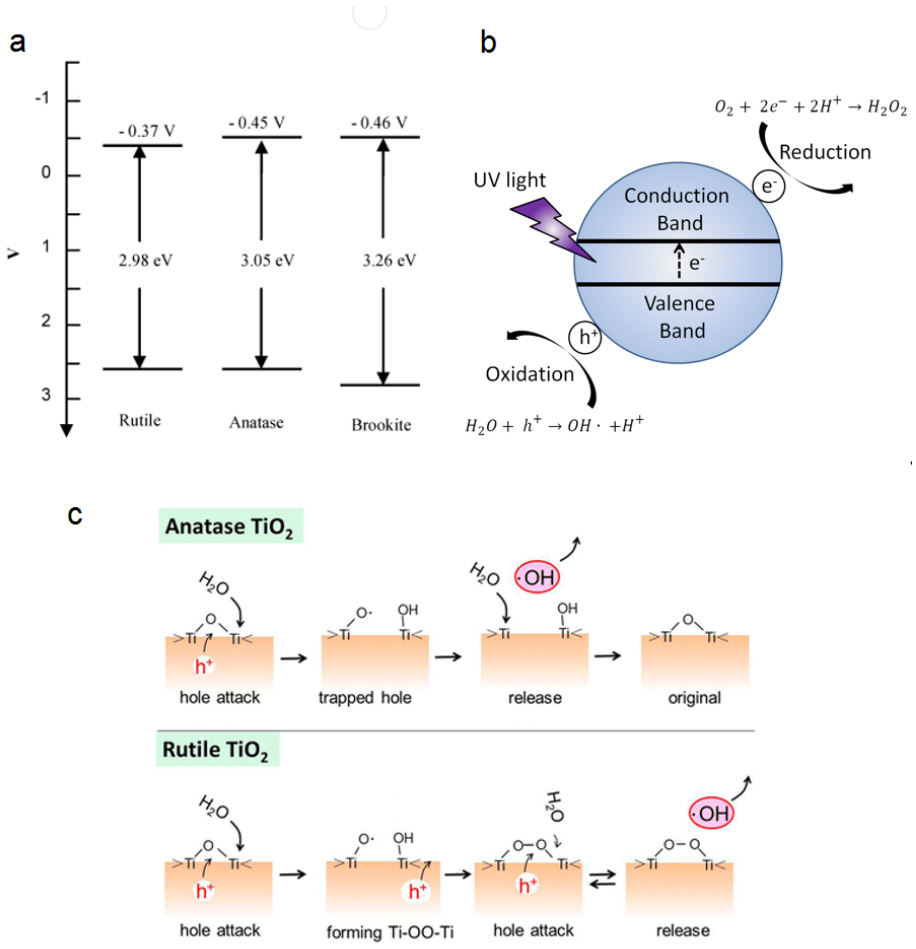

Figure 2. (a) Bandgaps of rutile, anatase and brookite.[19] (b) General scheme for photocatalytic reactions at TiO_2 nanoparticle surface in aqueous conditions. (c) Detailed hole-attack pathways for anatase and rutile. [26]

This area has been heavily researched in the past decade and remains an important topic today. A summary of key results to date have been presented in Table 1. The literature has been reviewed with respect to the following criteria:

(i) *Nanostructure*

Currently known TiO_2 nanostructures include simple nanoparticle[27], porous nanoparticle[28], nanotube[29], and porous film[30]. Porous structures, particularly mesoporous structures have the advantage of high surface area that can be used for the binding of the target drugs[31]. However, simple nanoparticles have the advantage of smaller size and therefore ease of injection/ diffusion at the desired sites[32]. Porous films are suitable for implants designed for longer term application.

(ii) Drug loaded/ delivered

An attempt has been made to catalogue the range of currently known drugs that can be delivered using the photocatalytic response of TiO_2. However, it should be noted that the identity of the delivered molecule is arguably one of the less important parameters. Given a good understanding of the mechanism behind attachment and release mechanism, it is possible to engineer the material to deliver any molecule of interest.

(iii) Functional molecule (if present)

Studies differ in the strategy used for loading the target drug onto the TiO_2. Some adsorb the target molecule directly onto the metal oxide surface[33], while others use a linking functional molecule[34]. The use of a tethering molecule may result in a more robust binding of the drug, reducing unintended passive leaching of the drug out of the nanoparticle. However, this also introduces an additional complexity to the structure. For example, upon UV illumination, bonds may break between the TiO_2 surface and the linking molecule and/or between the linking molecule and the target drug. Furthermore,

many drug molecules are highly specific and cannot be modified by a linker without losing efficacy, with the exception of modifications that result in easily metabolised prodrugs such as lysine-modified Ketoprofen, a transformation that in this case increases the effectiveness of the anti-inflammatory in question[35].

(iv) Excitation wavelength

The excitation wavelength is significant as UV light has high attenuation within tissue[36]. This means the penetration depth is typically low and damage to the surrounding tissue may be expected as the light energy dissipates. Light at longer wavelengths / lower energy is preferable in this respect.

(v) Illumination time

Similarly, the time scale over which the drug release happens is important both in terms of limiting the damage to healthy tissues[37] and determining the time required for effective elution of the drug away from the nanocarrier. For these reasons, it is desirable to minimise the time required for the release, or to consider pulsed release profiles.

(vi) Drug loading content

The final payload content as calculated as a weight ratio to the nanoparticle carrier is an important parameter as it serves as an efficiency metric for the drug delivery system. Due to the unknown toxicity of nanoparticles in general (in part due to their novelty and therefore lack of long-term studies), it is important to maximise this parameter.

A survey of literature has been presented below (Table 1) on the use of TiO_2 for release of drugs. There are two points of interest in the research to date. Firstly, it should be noted that, despite the photocatalytic character of TiO_2, the majority of papers found did not make use of this directly. Instead, porous forms of TiO_2 (commonly the nanotubes formed by anodic oxidation of Ti metal) were used as a passive base for the

loading and diffusion-limited release of the loaded drug out of the pore spaces. In such cases, the photocatalytic character of the TiO_2 carrier has no bearing on the effectiveness of the platform, and a similar effect can be expected for any base material of similar surface area and porosity. As I will discuss in *Section 1.2.3*, this is the basis behind the popular use of mesoporous SiO_2. In these porous structures based on passive release, the time-frame for delivery of the payload molecule is usually in the range of several hours[38], and even up to the month scale[39] for full elution. On the other hand, photocatalysis is fast-acting. It should be noted that Shrestha et al. were able to achieve a remarkable release "within a few seconds" due to their use of a Siloxane linker that bound covalently to the TiO_2 surface and then cleaved by the action of UV light illumination.[21] However, Shrestha et al.'s work is in the minority here, and highlights an opportunity for further studies of a photocatalytic-driven drug release system.

Perhaps part of the hesitation in the use of light-activated release systems based on TiO_2 is due to the inherent limitation of using UV in a biomedical context. The excitation wavelengths required to excite TiO_2 are usually in the ultraviolet B (UV-B) region, the band gap of pure Anatase and Rutile being ca. 3.2 eV (387 nm) and 3.0 eV (413 nm) respectively[40]. Ultraviolet light is cytotoxic, causing inflammatory and immunosuppressant effects even after short-term exposure[41]. Furthermore, it attenuates quickly within tissues with low penetration past the epidermis[36] and is therefore unsuitable for triggering any internal devices. This is undesirable and must be improved if TiO_2-based structures are to have a future in drug release. Strategies have emerged to improve this property. For example, X-rays may also be used to excite photochemical reactions at the TiO_2 surface to trigger photocatalytic drug release.[42, 43] Although X-rays carry the inherent risk of high energy ionising radiation, this may be justified by

the benefits of targeted drug delivery and partially mitigated by the short exposure times typically required for photocatalysis to occur in a similar risk management strategy to the current use of X-rays for diagnosis.

Alternatively, the band gap of TiO_2 may be shifted towards the lower energy / longer wavelength side of the electromagnetism spectrum by applying some suitable modifications. Visible light presents the advantage of being less toxic than ultraviolet[44] and penetrates more deeply in human tissues than ultraviolet. However, near-infrared light is superior in this regard, having the best penetration in tissue[45] when compared with both visible[46] and ultraviolet[36]. It is for this reason that NIR-triggered nanomaterials (usually coupled with a thermoresponsive component) have become an important area of research.

For example, doping titanium oxides with metal ions such as Ru[47], V[48] and Fe[49] or non-metals such as C[50], N[51], S[52] and B[53] may shift the wavelength into the visible range[54] and even leading into the NIR[55] range. Alternatively, a sensitising dye may be coupled with TiO_2 nanoparticles to extend the wavelength into the visible range (typically < 750 nm). This strategy is widely used for improving the absorption of natural light in dye-sensitised solar cells[56] and water-splitting[57]. The most prominent dyes for this purpose Rhodamine B[58], Coumarin[59] and Ruthenium complexes[60] are all well-known for their toxicity, a disadvantage that cannot easily be overcome. Finally, TiO_2 nanoparticles may be coupled with plasmonic Au[61] and Ag[62] nanoparticles. Plasmonic Au in particular is a popular choice for drug delivery due to the tuneable excitation wavelength and the chemically and biologically inert nature of gold[63].

Despite these limitations, TiO_2 remains a popular study subject in drug release. However, perhaps it should be noted that TiO_2 is better suited for application in external applications such as wound dressings, and that while its optical properties can be improved, it is worthwhile considering that other materials may be better candidates for internal applications.

Table 1 Selected results on TiO_2 for light-activated release of drugs

TiO_2 structure	Drug Delivered	Linking Molecule	Excitation wavelength	Release time	Loading Content	Source
Nanotube	Horseradish peroxidase	APTES	325	0 – 600s	~4.4 × 10−11 nmol per tube	[31]
TiO_2 core-shell composites	Doxorubicin	None	980 nm	0 – 50 hours	N/A	[64]
Nanoporous film	Dexamethasone	None	None	0 – 48 hour	362 ng/ mm^2	[65]
Nanotube	Paclitaxel, BSA	None		0 – 50 days	Paclitaxel: 5μg/cm^2. BSA: 110μg/cm^2	[66]
Nanotube	Anti-microbial Peptides	None	None	4h – 7 days	N/A	[67]
Nanoporous particle	Ibuprofen	None	None	0 – 3000 mins	N/A\	[33]
Nanotubes	Fluorescent Dye	Siloxane	UV	"A few seconds"	N/A	[21]
Nanotubes	Lysozyme, BSA	None	None	0 – 110 min	N/A	[68]
Nanoparticles	Daunorubicin	None	None	0 – 48 hours	N/A	[38]
Nanoparticle	Doxorubicin	N-(Trimethoxysilylpropyl) ethylene diamine triacetic acid	None	48 hour	9.2 wt% DOX to particle	[34]
Nanotubes	indomethacin	PLGA coating	None	Up to 30 days	N/A	[39]

1.2.2 SiO_2 the inert carrier

Although nanoporous TiO_2 structures have been used for drug loading and release, it is SiO_2 that is more popular in this role. The almost ubiquitous popularity of SiO_2 arises from its relative chemical inertia, a property that makes it an ideal passive carrier with long-term stability and low impact on its biological environment.

In addition to the spherical particles, a mesoporous form of amorphous SiO_2 has been known since the 1970s[69]. Mesoporous SiO_2 nanoparticles have extremely high surface area (> 900 m^2/g) is particularly useful for drug release[70] and gene transfection.[71] In the simplest designs, the porous SiO_2 acts as a sponge whose many nanoscale pores may be loaded with the medical cargo, typically at levels exceeding those of other common drug delivery carriers such as liposomes, non-porous nanoparticles, or polymers.[17] The surface chemistry of SiO_2 allows for electrostatic[72], hydrogen-bonding[73] and van der Waals interaction with the cargo, ultimately allowing for loading capacities that surpass the solubility limit of a solution or osmotic gradient loading. This is particularly effective for drugs that have low solubility in aqueous media but may form stable complexes with the nanoparticles, for example ibuprofen[74], itraconozole[74], and highly hydrophobic anti-cancer drug Tamoxifen[72].

In this simplest scenario, drug elution is ongoing out of the pores with a rate that is typically diffusion limited[75]. Modifications such as a polymer coating and gating molecules at the silica surface allow greater control over the delivery. For example, such components may be sensitive to endogenous triggers for the release of the payload. This includes local pH[76] and salt concentration.[77] With appropriate design, porous silica based nanocarriers may also be selectively activated by exogenous triggers. One

example is the use of labile, heat-sensitive gates[78]. Many strategies have been developed to functionalise SiO_2 surfaces with organic molecules suitable as tethering ligands or gate-keeping molecules, just as for TiO_2. These will be discussed in in *Section 1.5*.

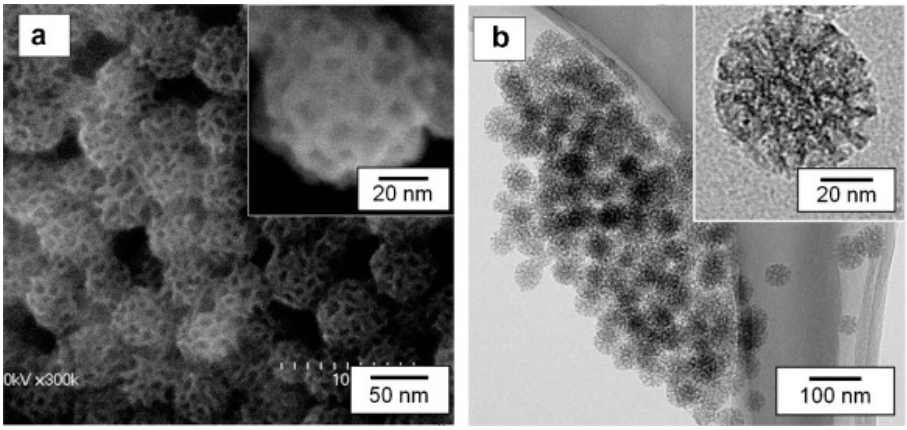

Figure 3. Example of Mesoporous SiO_2 electron micrographs. [79]

In addition to mesoporous particles, SiO_2 is currently important as a coating or matrix material for other functional nanoparticles. For example, it is commonly used for coating superparamagnetic iron oxides (SPIONs)[80], quantum dots[81], and plasmonic Ag[82] and Au[83]. The chemical stability of SiO_2 makes it an excellent barrier that can improve the cytotoxicity[84] and long-term stability of the functional nanoparticle cores while being simultaneously optically[85] and magnetically transparent so that it does not effect the functionality of the nanoparticle core. Finally, it is has a well-established Stöber synthesis route[86] that results in particles of well-controlled monodisperse morphology[87] at a large scale and low-cost, which has contributed in no small way to its currently ubiquitous popularity.

1.3 Magnetic nanomaterials for drug release

Of the inorganic nanomaterials, none have attracted more interest for biomedical applications than magnetic materials. This is due to the importance of magnetism in biomedical applications that allow for 'at-a-distance' manipulation by the application of external magnetic fields[88]. Magnetic forces, unlike other stimuli such as light and x-rays, have the advantage of deep penetration with relatively low attenuation or harm to living tissues[89]. This can be used to direct their location within biological systems[90], allowing for targeted therapies[91]. Secondly, magnetic nanoparticles may be used as MRI contrast enhancement agents[92], which allows easy monitoring of their location and action using existing technology[93], unlike other materials that effectively become invisible once they enter the biological system. A dynamic magnetic field may be also to induce magnetothermal responses[94] in the nanoparticles that can then be used for direct hyperthermia therapy[95] or for thermal-responsive drug delivery[94].

Unsurprisingly, this class of materials has been extensively studied over the past decade. This is particularly true for iron oxides such as magnetite (Fe_3O_4) and hematite (α-Fe_2O_3), due to their biocompatibility over other magnetic materials[96]. As a result of research efforts to date, the ability to control their chemical and physical properties is already advanced. Various synthesis methods have been documented, and the ability to control their size, composition, shape and surface chemistries are well understood.

Here, I have presented a survey of the key findings of the past two decades concerning the most biomedically important magnetic nanoparticles, their synthesis and resulting structures, methods for their functionalisation towards drug delivery, and finally some recent results in magnetic-field assisted synthesis.

1.3.1 Ferromagnetic versus superparamagnetic

It is useful to categorise magnetic nanomaterials into ferromagnetic and superparamagnetic as these classes have distinct behaviours. While the development of nanoscale ferromagnetic structures is known[97, 98], there has been far more work devoted to superparamagnetic nanoparticles. This is due to the challenge of guaranteeing good dispersion of the ferromagnetic nanoparticles compared with superparamagnetic materials. Due to the high surface area of nanomaterials, they usually exhibit strong attraction due to the van der Waals[99] and electrostatic[100] interactions that cause the formation of large, flocculated assemblies. In the case of ferromagnetic materials, an additional flocculation pathway by attraction of permanent magnetic poles exists and may not be easily reversed.[101] The formation of such aggregates is a disadvantage as it undermines the desirable small size and correspondingly large surface area nanomaterials. The overall smalls size is critical as it allows for injection into the blood stream[102], penetration through the blood-brain-barrier (BBB)[103], and uptake by cells[104]. The high surface area is crucial as it provides the platform for interaction with the system, such as through drug loading and release[105]. The formation of agglomerates in vivo may cause adverse effects such as thrombosis, although the critical size scale for this condition remains in debate[106].

On the other hand, superparamagnetic materials only develop a magnetic moment when in the presence of an external, inducing magnetic field. Materials that are ordinarily ferromagnetic in the bulk may take on superparamagnetic properties as the particle size decreases below that of the domain size, meaning that they become single rather than multiple domain[107, 108]. This is one of the key examples where material

properties do not directly scale down to the nano regime. Materials with documented size-dependant superparamagnetism include cobalt ferrite[109] and magnetite (Fe_3O_4).[108]

1.3.2 Magnetite

A brief review of the literature shows that of the magnetic nanomaterials, superparamagnetic forms of magnetite, Fe_3O_4, are overwhelmingly preferred for biomedical applications. This may be in part due to its convenient and well-established superparamagnetic character, so important for applications of drug release. At particle diameters of 10 – 20 nm, Fe_3O_4 becomes superparamagnetic in nature[110], existing in single magnetic domains. This size scale of magnetite has been well-studied, and numerous efficient, facile, scalable routes of synthesis exist for producing such particles with highly specific size and shape control. Above this size Fe_3O_4 NPs will consist of multiple domains and show an open hysteresis value typical of ferromagnetic materials. Despite this, research towards biomedical applications of Fe_3O_4 has been conducted on a range of iron oxide sizes from 10 – 100 nm. Some key results of the past decade on superparamagnetic iron oxide nanoparticles (SPIONs) for biomedical purposes, their mode of synthesis, and their relevant material characteristics have been presented in the following table (Table. 2).

1.3.3 Passive Versus Activated Release

It is noteworthy that most drug release studies to date make use of a passive and sustained release mechanism wherein the payload is allowed to diffuse out gradually from the magnetically guided nanocarrier. However, in recent years, rapid rate drug release promoted by an active agent has gained much attention. An activated system allows for a local and temporary enhancement in release rate. This ‘on-off’ action

allows for pulsatile release profiles that is allows, additional control over therapy compared to a sustained, passive system.

Release rate may be accelerated depending on the pH of the transfer medium and the relative solubility of the drug at these conditions.[111] The magnetothermal properties of SPIONs[112] have been well-studied and its use in hyperthermia therapy using the heat generated by magnetically vibrating SPIONs to directly destroy cancer cells[113] and bacteria has been proposed. However, this has not translated to a significant body of work on using a high frequency magnetic field (HFMF) to remotely trigger the release of drugs. An exception is the work of Hu et al.[114] who present a drug-loaded SiO_2 core surrounded by a Fe_3O_4 coating layer that is designed to rupture upon applying HFMF.[115] Meanwhile, Satakar et al.'s study makes use of the magnetothermal response combined with a thermally-responsive hydrogel coating.[116] Work on thermally-responsive hydrogel coatings for drug delivery are relatively well-established[117], but as yet combining this with the magnetothermal effect has not been reported.

It is possible to envision a system that combines magnetically activated delivery with MRI visibility to create a synergistic system. It is particularly popular in current research to functionalize the surface of magnetite and magnetite-composite materials with a targeting moiety for cancer-specificity towards the development of so-called 'theranostic' systems that simultaneously allow visualisation of the affected areas and therapy through either drug or direct hyperthermia treatment.

Table 2. Magnetite-containing nanomaterials for biomedical purposes

Size (nm)	Shape	Application	Functional coatings	Activation	Targeting	Source
21	Sphere	Drug Delivery (DOX)	Polymer	Passive		[118]
10	Sphere	Drug Delivery (DOX)	PVA	Passive		[119]
11-15	Sphere	Drug Delivery (DOX)	Starch	Passive		[92]
10	Sphere	Drug Delivery (DOX)	PEG	pH		[111]
9.3	Sphere	Drug Delivery (DOX)	Oleic Acid	Passive		[120]
15	Sphere	Drug Delivery (DOX)	Dopamine HSA	Passive		[121]
8	Sphere	Drug Delivery (DOX)	None	Passive		[122]
5-10	Sphere	Drug Delivery (PTX)	NH_2-terminated PEG	Passive		[123]
5	Sphere	Drug Delivery (PTX)	PEG	Passive		[124]
15-20	Sphere	Drug Delivery (PTX)	PLGA	Passive		[125]
150	Sphere	Drug Delivery (Gene)	PEI, PEG, Chitosan	Passive		[126]
15	Coating (Inverse core-shell)	Drug Delivery (Fluorescent Dye)	Fe_3O_4 coating, PVP-modified SiO_2 core	HFMF		[114]
30	Sphere	Drug Delivery (DOX)	Hybrid Poymersome	HFMF		[127]
50	Sphere	Drug Delivery (Gene)	Dextran	HFMF		[128]
25	Sphere	Drug Delivery (Vita B12)	Hydrogel	HFMF		[116]

8	Sphere	Drug Delivery (TMX)	Folic Acid, β-cyclodextran	HFMF		[129]
10	Sphere	Drug Delivery	Eicosane	HFMF		[130]
2000	Cluster	Drug Delivery (Budesonide)	Lipid	HFMF		[131]
7 - 9	Sphere	Hyperthermia Therapy (Cancer)	PEG, Folic Acid	HFMF		[113]
10000	Cluster	Hyperthermia Therapy (Antibacterial)	None	HFMF		[132]
23600	Cluster	Hyperthermia Therapy (Cancer)	Silica	HFMF		[133]
6-20	Sphere	Hyperthermia Therapy (Cancer)	Silica, hydrogel	HFMF		[134]
60 – 80	Cluster	Hyperthermia Therapy (Cancer)	PEG, Folic Acid	HFMF		[135]
13 – 40	Cube	Hyperthermia Therapy	None	HFMF		[136]
5	Sphere	Hyperthermia Therapy	Hyaluronic acid, PEG	HFMF		[137]
45	Magnetosomes	Hyperthermia Therapy	Citrate, PEG	HFMF		[138]
12	Sphere	MRI	Autofluorescent Albumin	-	ATF	[139]
80 – 160	Cluster	MRI	Citrate	-	-	[140]
7.5	Sphere	MRI	Mercaptopropionic acid, dextran	-	-	[141]
6	Sphere	MRI	Folic Acid, PEG, PDLLA,	-	Folate	[142]
10 – 15	Sphere	MRI	Fluorescent Dextran		Protamine	[143]
10	Sphere	MRI	Targeting ligand		2-aminoethyl-trimethyl ammonium	[144]
		MRI			Glial fibrillary acidic protein	[145]
16	Sphere	MRI	Carboxylic manna		Mannose receptor	[146]

1.3.4 Fe_3O_4-containing nanocomposites

Composites nanostructures containing Fe_3O_4 are useful as they may add additional functionality and useful properties. Most notably, coating the iron oxide in a material such as silica or a suitable polymer may further improve the water-stability of the nanoparticle as well as its chemical inertness in biological conditions. For this reason, most composites of iron oxide focus on core-shell like structures, although other structures do exist. The synthesis of composite structures may be performed in two steps, whereby the Fe_3O_4 NPs are then combined with the second material or through a single-step co-synthesis where the two materials are formed simultaneously. The main structures currently known in literature have been illustrated below (Figure 4).

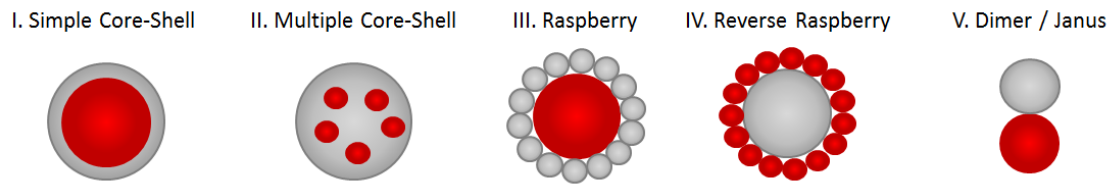

Figure 4. Heterogeneous composite nanostructures of magnetite

1.3.5 Composites with polypyrrole

In this thesis, Fe_3O_4 is combined with polypyrrole to create structures that have magnetic functionality combined with the electrical, optical and thermal properties of polypyrrole. The known structures to date are simple core-shell, multiple core-shell, aggregated and raspberry-like structures (Figure 5).

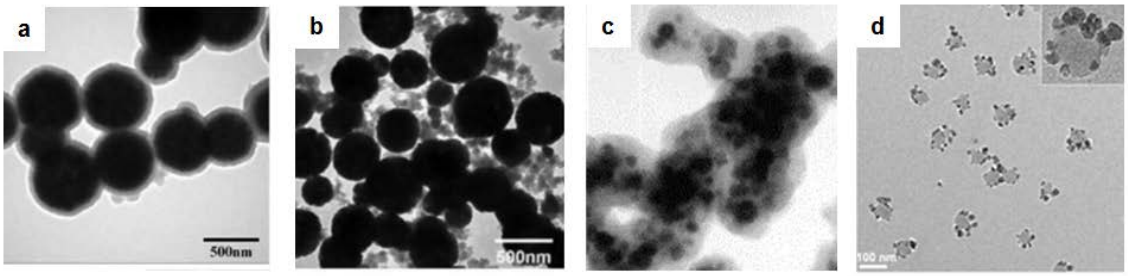

Figure 5. Known structures of PPy-Fe_3O_4 nanocomposites. (a) core-shell[147], (b) aggregated[147], (c) multiple core-shell[148], (d) raspberry (PPy core, Fe_3O_4 decorations)[149]

Composites of PPy and Fe_3O_4 may be synthesised by including suspended Fe_3O_4 NPs in the chemical polymerisation mixture for PPy, in a process of seeded polymerisation. However, the resulting structures differ significantly depending on the particulars of the process. There are several important concepts to consider during such a two-step synthesis. Firstly, the degree of aggregation of the nanoparticles is important. For uniform core-shell structures, a highly desirable structure, the nanoparticles must be well-dispersed during synthesis. Secondly, both the location and type of nucleation of the PPy particles is important. For example, a homogeneous nucleation that is not concentrated at the Fe_3O_4 nanoparticle surfaces will result in randomly aggregated structures.

Indeed, it has been reported that when synthesised without surfactants to prevent the aggregation of Fe_3O_4 NPs, an aggregated structure comprising polypyrrole NPs that nucleates away from the Fe_3O_4 surface results (Fig. 4 b) whereas the inclusion of a surfactant such as sodium dodecyl sulfonate will promote a core-shell structure comprising a homogenous polypyrrole layer over the nanoparticle cores.[147] The use of a copolymer such as PVA may have a similar effect in promoting the growth of the core-shells[148]. Wuang et al. combined typical oxidation route with PVA-based microemulsions to create PPy particles with multiple encased Fe_3O_4 cores.[150] Tian et

al.[149] was able to create the reverse, raspberry-like structure of PPy serves surrounded by Fe_3O_4 decorations on the structure surface by applying using an $FeCl_3.6H_2O$ oxidant in excess and applying a second step to convert excess Fe^{3+} into Fe_3O_4 nanoparticles.

The oxidant used will also have an effect on the structure. While both APS and $FeCl_3.6H_2O$ are commonly used in oxidation of polypyrrole, in the synthesis of PPy-Fe_3O_4 composites the use of $FeCl_3.6H_2O$ may be advantageous due to the common ion effect. It is hypothesised that $Fe^{3+}_{(aq)}$ adsorbs on the Fe_3O_4 nanoparticle surfaces, thus promoting the polymerisation of PPy at the nanoparticle surface.[148]

1.3.6 Magnetically-driven synthesis and self-assembly

One concept that is unique to magnetic nanomaterials is the use of a magnetic field during their synthesis to promote the growth and/or assembly of 1-dimensional, anisotropic nanostructures along the direction of the field lines. This process involves the transport and arrangement of matter under an applied magnetic field. This may be follow by or occur simultaneously with stabilization of the assembled structure by chemical means. Before discussing the recent progresses in this area, it is important to understand the fundamental underlying theories governing this process.

Firstly, the movement of transition metal ions in a solution is governed by the magnetic force, F(z) defined as

$$F\ (z) = \ \chi n H(z) \frac{\partial H(z)}{\partial z} \qquad \text{(Equation 3)}$$

Where χ is the molar magnetic susceptibility of metal ions with mole number n at the position z within a magnetic field $H(z)$. Hence, it has been observed that larger movement under the same field gradient occurs for ions of larger susceptibility[151]. At the same time, a larger overall ion concentration induced larger movement, which

indicates that the ions move as a group and not as independent single particles. The drift velocity of these ions, *v(z)*, has the following simple relationship to the magnetic force.

$$v(z) \propto F(z) \qquad \text{(Equation 4)}$$

The movement of ions is in line with the magnetic field, with overall migration towards the centre of the field. This results in the formation of 1D structures along the field lines. These two equations govern the transport component. The energy component is governed by the following equation for the magnetic energy *E* of an object of volume *V* under a magnetic field *B* through a space of permittivity μ_0:

$$E = \frac{1}{2\mu_0}\chi V B^2 \qquad \text{(Equation 5)}$$

If the magnetic energy is greater than that of the thermal energy for a system, the objects will orient to the applied field. Since magnetic properties are anisotropic within a crystalline grain, they will do so by orienting in the crystal direction that will minimise the energy of the system. This direction is called the 'easy direction'. In Fe_3O_4, the easy magnetic axes are along [111] and [110] directions.

These fundamental forces are utilized in nature within magnetotectic bacteria. This class of bacteria form chains of magnetic nanomaterials within their bodies. It is currently understood that these anisotropic magnetic nanostructures, called magnetosomes, aid the bacteria in finding their orientation within the earth's magnetic field (Figure 6). Some attempts have been made to harvest these magnetosomes and apply them subsequently to biomedical applications[152] such as delivery of DOX[153] and magnetothermal therapy.[138] However, due to the need for culturing, harvesting and purification of these magnetosomes, there has emerged a recent interest in artificially synthesising analogous materials.

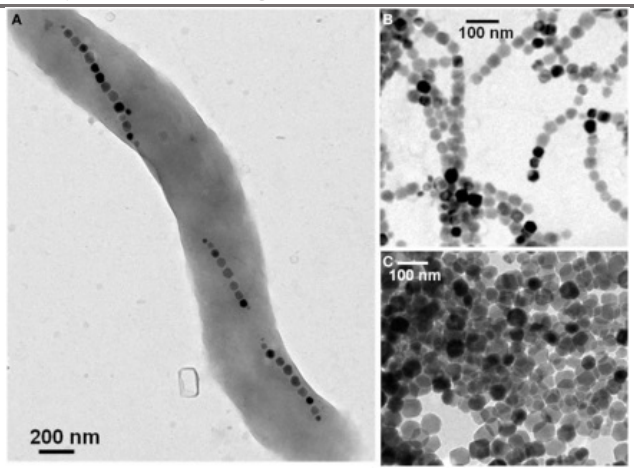

Figure 6. Transmission electron microscopy images of a single magnetotactic bacterium (A) of chains of magnetosomes extracted from whole magnetotactic bacteria (B) of individual magnetosomes detached from the chains by heat and SDS treatment (C).[152]

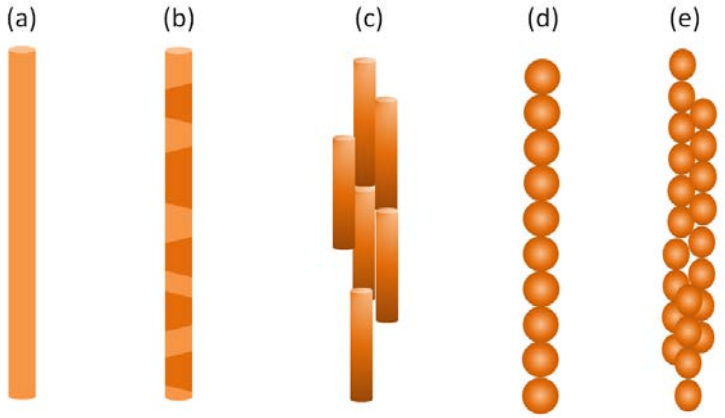

Figure 7. Schematic illustrating various known 1D structures resulting from synthesis under an applied magnetic field. (a) single crystal nanowire, (b) multi-crystal nanowire, (c) bundled nanowire, (d) nanochain of isotropic nanoparticles, (e) aggregated chain.

The current work on the synthesis of anisotropic magnetic materials under an applied magnetic field may be divided into several categories depending on the resulting morphology. The two main structures are rod-like (Figure 7 a,b) and chain-like (Figure 7 c). Of course, as for all nanomaterials, the tendency to form aggregates (Figure 7 c,e) is ever present.

Rod-like or wire-like structures are typically synthesised in one step, coupling an applied magnetic field with a typically liquid phase synthesis of iron oxides. For

example, Wang et al. have reported the fabrication of single crystal Fe_3O_4 nanowires by hydrothermal process by applying a field of up to 0.35T. [154] The nanowire that resulted was found to grow primarily along the [110] direction and is in good agreement with the theory discussed above of ion migration along magnetic field lines during synthesis. Similar results were observed for sonochemical[155] and thermal decomposition[156] synthesis. It is similarly possible to create multi-crystalline nanowires and rods by such one-step methods under certain, kinetic driven conditions.[157]

In addition to rod or wirelike materials, application of a magnetic field can also be used to assemble individual isotropic (usually spheroid) nanoparticles into 1D, chainlike forms. These structures may be understood to form in a two-step process. First, the nanoparticles are formed without the influence of a magnetic field, and then arranged under the aligning magnetic field. This is typically accomplished in the liquid phase with suitable surface treatment of the magnetic nanoparticles for either colloidal stability or as an adhesive coating to stabilize the assembled anisotropic structures. For example, Chong et al. were able to create end-on-end, well-dispersed nanochains with tuneable size by encapsulating Fe_3O_4 NPs with SiO_2 in a microfluidic reactor.[158]

The key publications of the past decade in magnetic field directed synthesis have been summarized in the following table (Table 3).

Table 3. Magnetically directed synthesis of anisotropic materials

	Method	Material	Field Strength (T)	Source
Liquid Phase	Hydrothermal	Single crystal Fe_3O_4 nanowire	0.25	[154]
	Hydrothermal	Fe_3S_4 and FeS_2 multi-crystal microrods	0.045	[159]
	Hydrothermal	Co_3O_4 nanowire	0.24	[160]
	Sol-gel	TiO_2 nanowires	9.4	[161]
	Solvothermal	Bi single crystal nanowires	8	[162]
	Solvothermal	Ni-Co alloy nanowires	0.08	[115]
	Sonochemical	Fe_3O_4 nanorods	0.5	[155]
	Microwave	Fe_3O_4/C/CdS coaxial nanochains	0.2	[163]
	Wet chemistry	Ni nanochains	0.5	[164]
	Wet chemistry	PEDOT:PSS encapsulated iron oxide NPs nanochains	0.065	[165]
	Wet chemistry microfluidic	SiO_2 encapusulated Fe_3O_4 NPs nanochains	Unreported	[158]
	Wet chemistry nanocapillary coating	Fatty acid encapsulated Fe_3O_4 NPs nanochains	0.0012	[166]
Vapor Phase	Chemical Vapor Deposition	GaN nanowire	0.25 – 0.8	[167]
	Arc Plasma	SWCNT	0.02- 0.2	[168]
	Flame synthesis	Co multi-crystal nanowire	1	[157]

This present work is particularly interested in the synthesis of chainlike and aggregated chainlike structures. Unlike the rod-like counterparts, these chains can be flexible when a suitably soft material is chosen as the encapsulating agent. For example, Ho et al. was able to create conductive, flexible filaments of iron oxides by using conductive polymer PEDOT:PSS as the coating material. [165] Of course, when a rigid material such as SiO_2 is used as the coating instead, the resulting nanoparticle chains are as rigid as expected.[158] Additionally, the assembly of magnetic nanochains may be engineered to be reversible. Bharti et al. coated iron oxide chains with fatty acids to create a thermally-responsive material that would be reconfigurable when the fatty acid was in liquid state and exploited this for magnetically directed self-healing of the filaments.[166]

In addition to end-on-end chains of single particles, it is possible to create large, needle-like structures that result from the aggregation of large numbers of nanoparticles in the direction of the magnetic field.[169] These structures are termed ‘needle-like’ due to the profile of the structure’s width dimension, comprising a middle section of several nanoparticles’ width that tapers to a fine, needle-like point (Figure 8). At present, it is unclear what experimental conditions cause these two vastly different reported morphologies, and how conditions may be selectively and controllably exploited to favour one over the other.

Finally, it is important to consider the dynamic behaviour of the chainlike materials, in particular the soft, flexible materials. Bharti et al.[169] have reported a flexible, curling motion (Figure 10) that is unique to soft-coated nanochains and is not, for example, observable in the SiO_2-encapsulated chains presented by Chong et al.[158] Although the irreversible formation of circular bundles reported by Bharti may be a

disadvantage as it destroys the anisotropy of the structure, it is nonetheless an interesting and unique material property. At the very least, this work indicates the importance of tracking the dynamic behaviour of such structures which can be demonstrably irreversible.

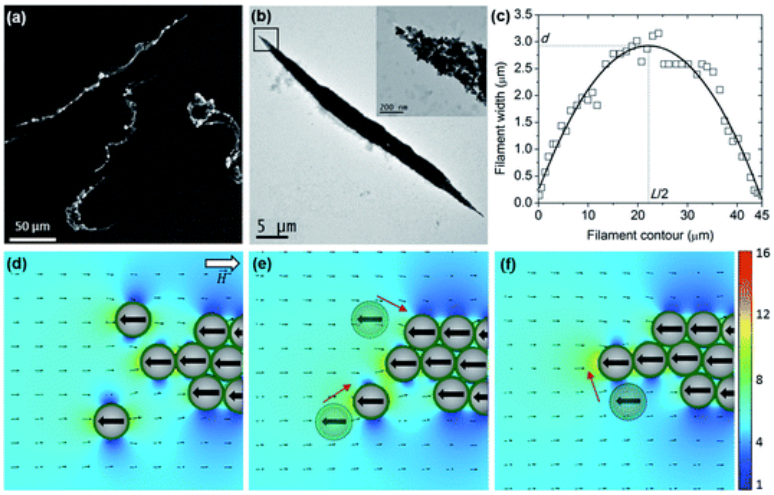

Figure 8. Formation of aggregated nanochains under an applied magnetic field.[169]

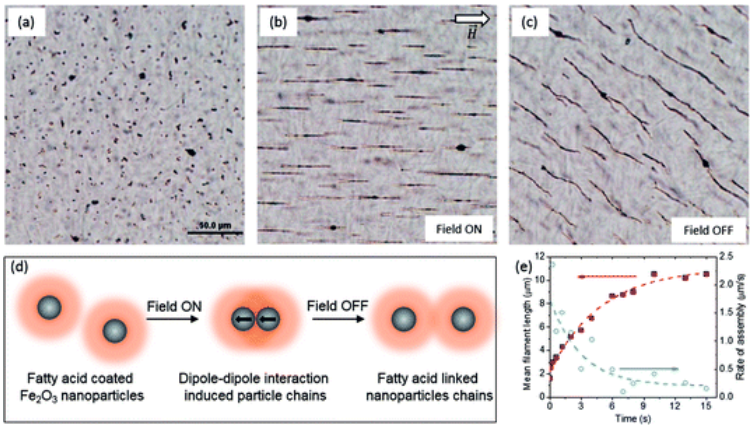

Figure 9. Flexible motion of soft-encapsulated nanochains[169]

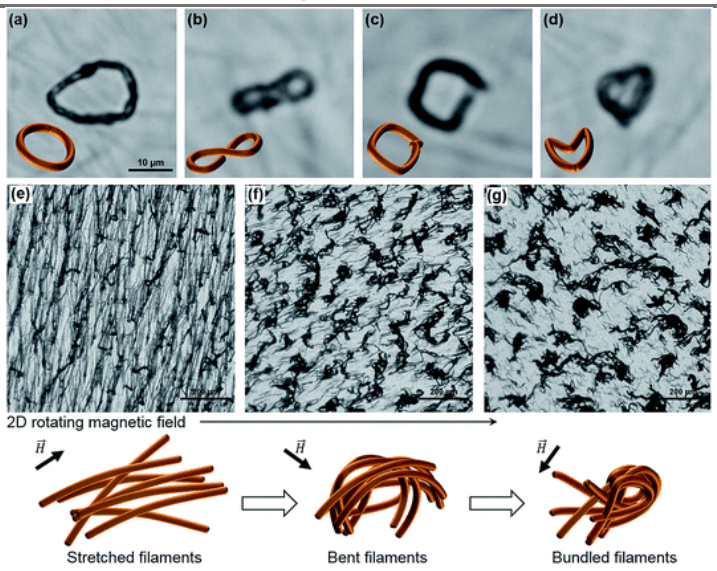

Figure 10. Irreversible formation of spheroid bundles upon applying a rotating magnetic field.[169]

To date, the synthesis and assembly of 1D nanomaterials under a magnetic field remains relatively novel, despite the potential of such materials in numerous areas. For the purpose of this work, it is the potential of such materials towards drug delivery that is important. Anisotropic materials that may be magnetically actuated have numerous potentially useful properties. Firstly, they may be arranged or patterned by external magnetic field alignment. The ability to create aligned structures for drug delivery has been of interest recently, in particular in scaffolds for neuron growth. The ability to promote neurite extension in one direction by using a suitably patterned nano- or micro-vehicle loaded with a neural growth factor is an area of high novelty and high impact research. 1D magnetic nanomaterials have a strong advantage over scaffold and coating system as they have the potential for dynamic response. While scaffolds are fixed, nanowires and chains can be manipulated at will by applying a simple change to the magnetic field strength or direction. To date, there have been no attempts to study what

the effect of controlled movement of the cell substrate would be on the resulting cell growth pattern.

The second useful property arises from the movement of the 1D structures when subjected to a rotating magnetic field. They are reported to follow the movement of the field direction and have been proposed by Chong et al. to be useful as nanoscale impellers inducing formation of local vortices.[158] While Chong et al. suggest the application of these vortices for microscale mixing to be used in lab-on-chip and other miniaturised systems, this function may also be of interest in drug delivery and other therapies. Firstly, the rotation of the 1D nanostructures induces local turbulence that may overcome the typical diffusion limitation of drug delivery systems. Secondly, the high speed rotating action itself may be used for therapy for targeted cell destruction. It has been recently discovered that physically breaking apart the cell walls of bacteria using a nanomachine may be highly effective at defeating pathogens.[170] Although no parallel studies have been conducted so far on using a similar mechanism for cancer therapies, this is potentially an area of high impact research.

1.4 Synthesis of Metal Oxide Nanomaterials

There are currently many methods to synthesise the metal oxide nanoparticles discussed in previous sections. The most important methods have been categorised in the following figure (Figure 11).

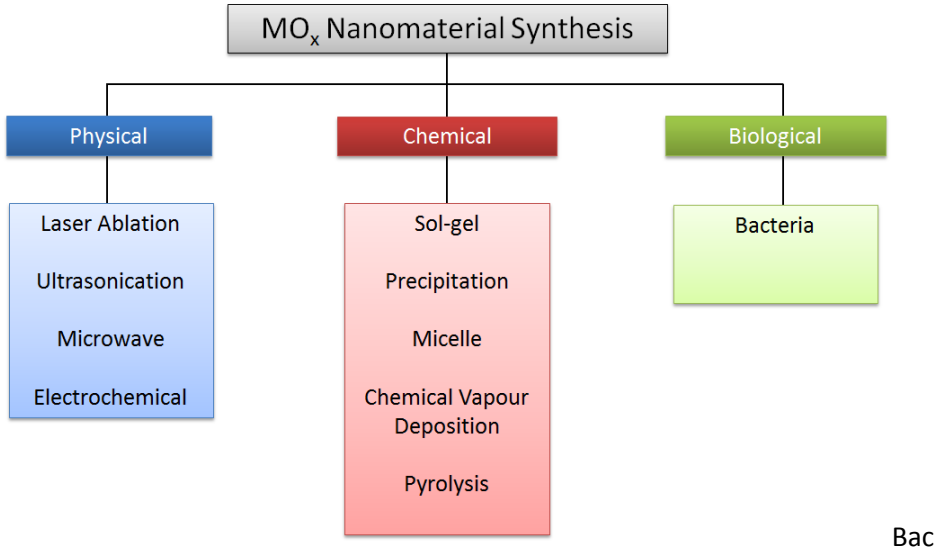

Figure 11. Synthesis methods for metal oxide nanomaterials

Currently, the chemical methods dominate the field. Each technique brings its own advantages and disadvantages, possibilities and limitations. Useful parameters to consider include speed and throughput, scalability, toxicity of materials involved, energy consumption, and resulting particle size, shape and uniformity. A brief comparison of the key chemical synthesis routes for TiO_2, SiO_2 and Fe_3O_4 follow (Table 4).

1.4.1 Flame Spray Pyrolysis

The dominant nanoparticle production method of this thesis is flame spray pyrolysis. It is a high throughput, low cost method that is able to create high purity nanoparticles of a suitable size scale (typically 5- 50 nm) in one step[171]. This method involves a combustible precursor containing the metal ions diluted in a highly flammable fuel (commonly ethanol[172], acetonitrile[173] or xylene[174]) that is injected through a nozzle with oxygen jets. An aerosol of fine precursor droplets is formed. This is then combusted by a continuous gas-fed flamelets that surround the aerosol, resulting in the production of metal oxides. These metal oxides nucleate to form nanoparticles that then

continue to collide and grow to their final size. They are driven to the cooled collection region by thermophoresis, forming a film with porosity typically in the range of 98%[175],and their collection may be aided by vacuum filtration. A schematic representation of a typical FSP reactor along with the growth mechanism of nanoparticles is provided below (Figure 12).

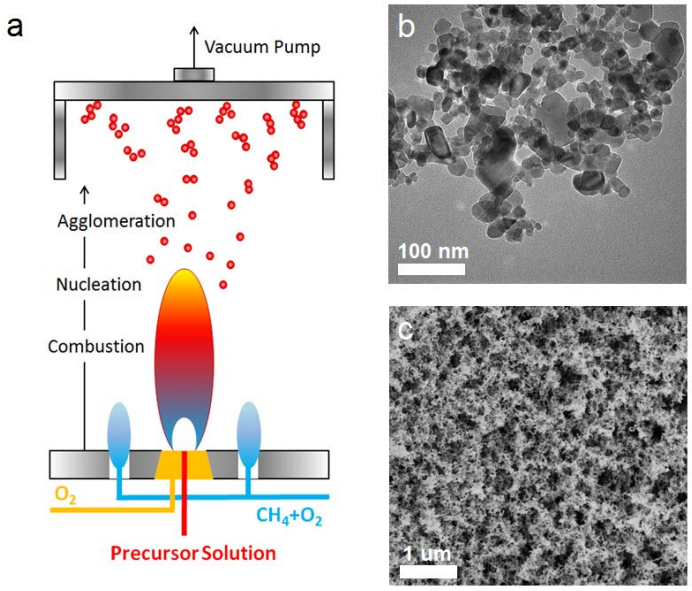

Figure 12. (a) Schematic representation of a typical FSP reactor. (b) TEM showing typical TiO_2 product and (c) SEM showing top view of porous film of the same.

Table 4. A brief comparison of different chemical routes towards MOx nanomaterial synthesis

Technique	Description	Advantage	Limitation
Chemical Vapor Deposition	Volatile precursors decompose and/ or react on a substrate surface to form desired products.	Highly uniform, 1D structures can be grown this way if using seeds.	High cost and low throughput. When unseeded, only films can be made this way.
Flame Spray Pyroloysis	Liquid precursors are combusted in a high temperature flame, creating nanomaterials, usually oxides.	High throughput Low cost High purity and crystallinity	Products are polydisperse. Some irreversible agglomeration to be expected.
Sol-gel	Precursor solution is mixed with a suitable catalyst slowly evolves into a gel-like state containing discrete nanoparticles in a polymer matrix.	Low cost and low tech.	A second, high temperature stage must be applied to purify the product. This can be a slow method.
Precipitation	Solution containing the nanomaterial precursors is mixed with a suitable initializer (e.g. oxidising/ reducing agent) to form precipitates.	Fast and easy. Scalable.	Controlled growth can be difficult. Particle size can be large and polydisperse.
Micelle	Two phase system of microdroplets of oil suspended in water is created. Nanoparticles are synthesised at the surface between the two phases.	Excellent control over shape and size is possible. Products can be monodisperse.	Currently only small-scale batch synthesis can be achieved.
Electrochemical	Eletrolyte containing precursor ions is either oxidised or reduced at the appropriate electrode to form solid material.	1D structure can be achieved by templating.	Cannot be used to create nanostructures without appropriate templating, only films.

The synthesis of both TiO_2 and SiO_2 by FSP are relatively well-established, therefore this thesis will not be concerned with optimising this known procedure. From the previous work, the following relevant and useful observations arise:

i. The resulting particle size scales with the concentration of the metal ion over the dispersing oxygen $[M]/O_2$.[172] In other words, at a given precursor concentration and system pressure drop, the greater the dispersion oxygen, the smaller the particle size.

ii. Typical particle size is between 5 – 50nm for SiO_2[172], 5 – 20m for TiO_2[176] and 5- 50nm for iron oxides.[177] In all cases, there is a significant particle size distribution within the sample that may be attributable to natural temperature profile within the flame.

iii. Some degree of hard agglomeration is expected due to the collision and subsequent sintering together of particles within the high temperature zone in the flame. Typical agglomerate size is between 100 – 200nm. This agglomeration is distinct from the van der Waals driven flocculation of nanoparticles as it is typically irreversible/ unbreakable even at high pressure.[178]

iv. TiO_2 is produced as mixtures of Anatase and Rutile. Particle shape is expected to be facetted spheroid.[179]

v. SiO_2 is usually produced as spherical amorphous particles.[180] However, nanowires have also been observed.[181]

vi. Iron oxides are produced in Maghemite, Wustite and Magnetite forms.[177] The synthesis of iron oxides is less advanced than wither TiO_2 or SiO_2 and is worth studying.

1.5 Functionalising metal oxide nanomaterials

Previously, the concept of using an appropriate tethering or gating molecule to improve the performance of the nanocarrier has been introduced. The functionalisation of nanoparticle surfaces with such suitable organic molecules is in itself an interesting and active research field due to the applicability of functionalised nanomaterials for biosensing[182], implant integration[183], bio-labelling[184], and, of course, drug delivery[185]. This section will outline the key concepts of this field in detail, with a particular focus on the interaction of amino acids with MO_x surfaces.

There are several general design considerations to be applied when choosing a suitable functional molecule, which may be simplistically understood to possess a head group (for the attachment of the target molecule to be delivered) and an anchor group (for attaching to the nanoparticle vehicle) connected by the spacer chain.

i. *Anchor group.* The role of this group is to form the bond between the surface of the nanostructure and the molecule. Different interactions are possible, including covalent[186], hydrogen[187] and electrostatic bonding[188]. There has been extensive study conducted on the adsorption mechanism of ceramic surfaces with various functional groups, most significantly carboxylates[189], amines[190], phosphonates[191] and silanes[192].

ii. *Head group.* This group should be tailored to suit the final application. The head group, being the group that is ultimately exposed to the surroundings, has a large role in the overall chemistry of the resulting functionalised material. For example, a nanoparticle may change from negative to positive surface charge[193] and from hydrophilic to hydrophobic[194] due to the action of this head group. In

this dissertation, carboxylate sand amines are considered due to the affinity of these groups towards proteins[195] and DNA[196] which renders them highly versatile within the fields of drug delivery and gene transfection.

iii. *Spacer*. The shape and length of the chain may have a small steric-limiting effect on the density of functional molecules attached to the nanostructure surface. For example, small linear molecules may show higher packing density than large, laterally bulky counterparts.[197]

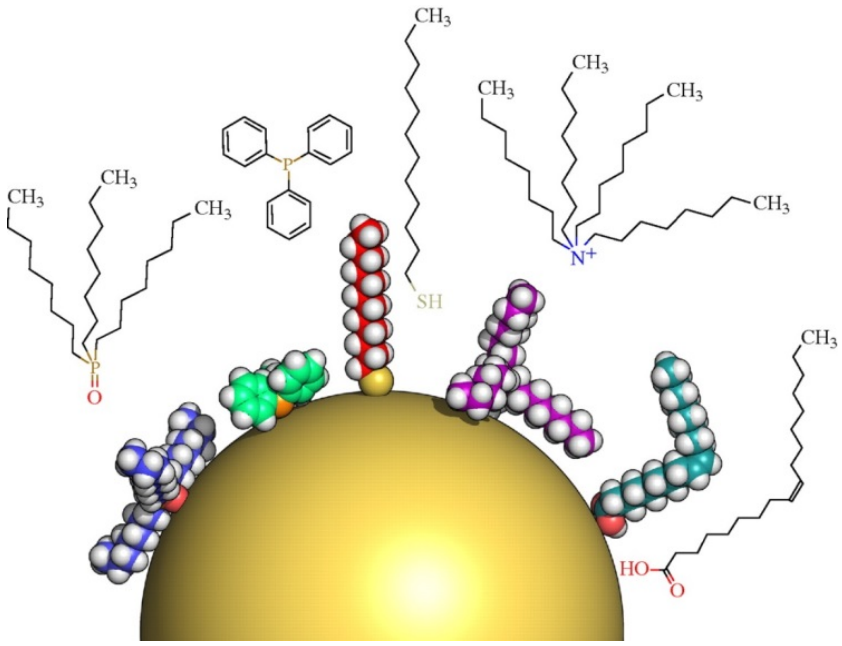

Figure 13. A nanoparticle of 5 nm with different ligand molecules. Left to right: trioctylphosphine oxide (TOPO), triphenylphosphine (TPP), dodecanethiol (DDT), tetraoctylammonium bromide (TOAB) and oleic acid (OA). [198]

1.5.1 Phosphonates

Metal oxide nanoparticle surfaces may be modified with phosphonates ($-PO_3$) resulting in mono-, bi- or tridentate anchorage of a phosphonate ligand on the metal oxide surface, creating a M-O-P bond. This can generally be accomplished using P-OH, P-OR or $P-O^-$ containing precursors. One example is the reaction of TiO_2 with phosphonic

acid[199], resulting in a Ti-O-P bond that is very stable toward hydrolysis. Conversely, the Si-O-P bond is highly sensitive to hydrolysis and is not stable[200].

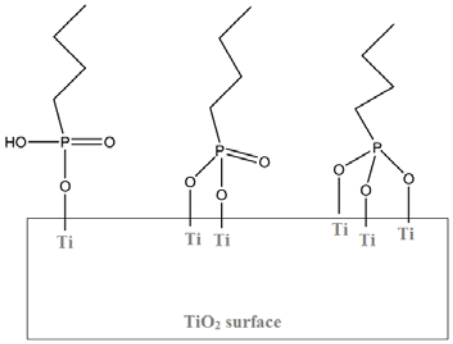

Figure 14. Phosphonate interaction with TiO_2 surface. From left to right: mono-, bi- and tridentate anchorage. Adapted from Neouze and Shubert.[201]

1.5.2 Silanes

Silanes are amongst the most common used functional molecules for MO_x surfaces due to the large variety of commercially available silanes (e.g. alkoxysilane, hydrogenosilane or chlorosilane) bearing different head groups (e.g. amino, cyano, carboxylic, epoxy) and their relatively easy grafting pathway. In particular, di- and trichlorsilanes are so reactive towards MO_x surfaces that multidentate attachments are favoured.[202, 203] This functionalisation is currently known for many metal oxides, including TiO_2[204], SiO_2[205] and Fe_3O_4[206].

1.5.3 Carboxylates

Carboxylic acids (-COOH) are commonly used for modifying MOx nanoparticles, particularly long-chain acids such as oleic acid which can be used to cap Fe_3O_4[207]. Several interactions are possible, including physical adsorption and several chemisorption forms (Figure 14). It has been reported that normal post-modification of metal oxide nanoparticles such as titanium dioxide by immersion in aqueous solutions containing the modifying functional molecule will result in simple physisorption by electrostatic or H-bonding rather than chemisorption.[208]

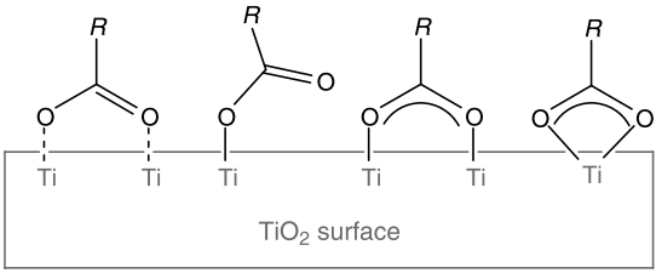

Figure 15. Carboxylate interaction with TiO_2 surface. From left to right: physical adsorption, monodentate coordination, bridging chemisorption, chelating chemisorption.[201]

1.5.4 Amines

The interaction between amines (-NH_2) and metal oxides is usually via electrostatic attraction[209] or hydrogen bonding, and is therefore weaker than the chemisorption configurations of the other anchor groups so far presented. For this reason, it is not common to make use of amine adsorption for functionalization of MOx nanoparticles.

1.5.5 Amino Acids

Due to the bio-interfacing potential of amino acids[210], the adsorption of these biologically important molecules onto the surfaces of metal oxide nanostructures has become an area of emerging importance in surface science. Amino acids are amphoteric, possessing both basic primary amine (-NH_2) and carboxylic acid (-COOH) groups and may thus undergo the bonding configurations typical of both of these anchor groups. This leads to several different possible binding mechanisms that are of fundamental interest.[211]

In the past two decades, there have been advances both empirically and theoretically on the adsorption of particularly important amino acids on likewise significant metal oxide surfaces (e.g. TiO_2, Fe_3O_4), although there remains a deficit in the empirical verification of adsorption models within the same study. At the same time, there is some disagreement in the data thus far collected. For example, it still remains unclear whether simple electrostatic attraction between metal oxide surfaces and

charged amino acids is the primary driver[212], or whether the adsorption pathway by replacing surface hydroxyls by the carboxylate group of the amino acid is in fact favoured[213].

The field is still waiting for a definitive study that unifies theories and data to date with a view towards explaining the precise mechanism of this pH-dependence as it relates to various bonding hypotheses. Furthermore, there have been few attempts to apply the key results to the optimisation of such structures towards biomedical applications where binding configuration and its resulting effects on such properties as surface charge, particle agglomeration/coagulation, and amino acid bond strength, although these factors have proven importance for cellular uptake[214] and toxicology[215].

A summary of the important works to date that have been included in this review are presented in Table 5.

Table 5. Key studies on interaction of metal oxide surfaces with amino acids

Metal Oxide	Amino Acid	Theoretical/ Empirical	Key Findings	Source
TiO_2	Glutamic Acid Aspartic Acid	Empirical (IR)	Aspartic acid adsorbs via electrostatic interaction Glutamic acid adsorbs strongly even when there is electrostatic repulsion.	[212]
TiO_2	Methionine Alanine	Empirical (XPS)	Amino acids generally tend to adsorb onto TiO_2 surfaces by their carboxyl groups replacing a basic hydroxyl on a Ti site, a process favoured by acidic milieu.	[213]
TiO_2	Lysine	Empirical (IR)	Lysine is maximally adsorbed near its isoelectric point of 9.8.	[188]
TiO_2	Aspartic Acid Homocysteine Lysine Serine	Empirical (X-ray photoelectron spectroscopy)	Most amino acids prefer to bind by the –COOH in acidic medium. At pH>6, Lysine interaction by $–NH_2$ dominates.	[216]
TiO_2	Glycine Aliphatic carboxylic acids	Empirical (IR) Theoretical (quantum-chemical calculations)	Carboxyl groups prefer bridge and monodendate binding.	[217]
TiO_2	Alanine Phenlyalanine Serine Aspartic Acid Histidine	Empirical (Zeta Potential	-OH (Ser), -NH (Trp, His), or $-NH_2$ (Asn) in their side chain appeared to be adsorbed more favorably	[218]

TiO_2	Lysine Polylysine	Empirical (IR)	Electrostatic interactions of the lysine peptides with the adsorbent are of main importance to adsorption.	
Fe_3O_4	Aspartic Acid Glutamic Acid	Empirical (IR)	Chemisorption of chelate type involving Fe(III) surface species and a carboxylate group.	[219]
Fe_3O_4	Glycine Glutamic Acid Lysine Arginine	Empirical (electrophoretic mobility)	Electrostatic interactions only considered.	[209]
Fe_3O_4	Cysteine	Empirical (IR, Mossbauer)	Both carboxyl and amine groups are involved.	[220]
Fe_3O_4	Aspartic Acid Leucine Glycine Glutamic Acid	Theoretical (Force-field calculations)	Electrostatic interactions dominate. Carboxyl-group (Asp and Glu) or to the carboxylate-group (Gly, Leu and Glu) are involved.	[221]
Fe_3O_4	Lysine Glutamic Acid	Empirical (Zeta Potential)	Carboxyl is preferred.	[222]
Fe_3O_4	Aspartic Acid Lysine	Empirical (Zeta Potential)	Carboxyl is preferred.	[223]

1.5.6 Reaction pH and amino acid functionalisation

One of the most important parameters to consider in the binding of amino acids to MO_x surfaces is that of the amino acid charge state as this determines the electrostatic attraction between the molecule functional groups and the metal oxide, a crucial step in the binding process. The protonation/deprotonation of the $–NH_2$/COOH groups is strongly pH-dependant and thus the overall charge of the molecule may be controlled by selectively adjusting the pH relative to the pK_a values for each of the functional groups of the amino acid. Figure 16 shows the pK_a values of several biologically important amino acids.

This pH-dependence is significant on three accounts. Firstly, it can be manipulated during synthesis to encourage certain interactions. Secondly, the net surface charge of any nanomaterials coated in amino acids can by tuned by changing the pH. And finally, it is important to be aware that under physiological pH 7.4, which is the ultimate environmental pH for most biomedical applications, most amino acids will exist in their zwitterionic form. This is important as amino acids in their zwitterionic form will be able to associate together by electrostatic interactions, causing adsorption of multiple layers of the molecules on the particle surface (Figure 17).[223] This is important to consider when designing nanostructures using amino acids as the functional coating as, depending on the final surface chemistry of the structure, there may be significant agglomeration of nanoparticles via this association mechanism. The association of nanoparticles into larger, microscale structures is often presented as a disadvantage due to the loss of the nanoscale functions, but in fact there may also be useful outcomes of this property, when this association can be controlled.

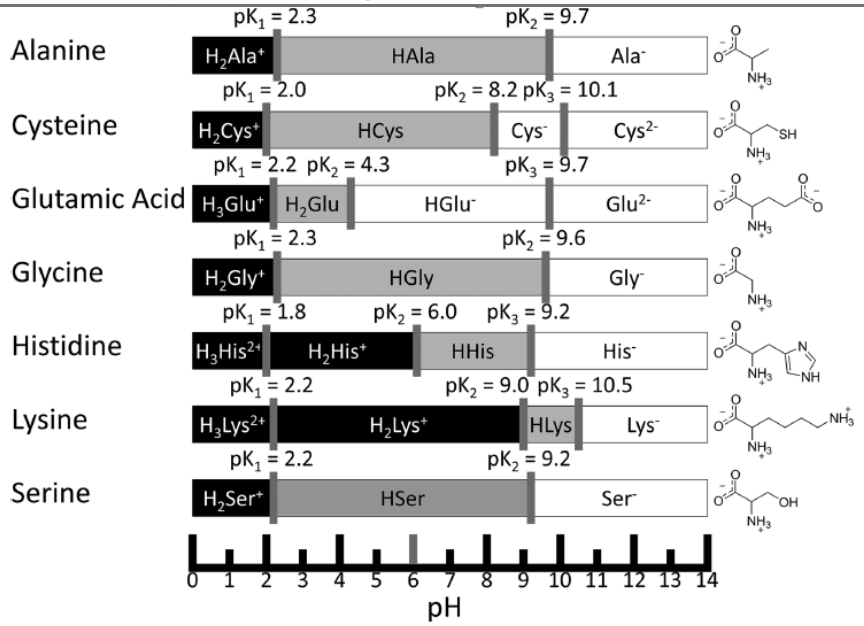

Figure 16. pK_a and charge state for various amino acids (adapted from[224])

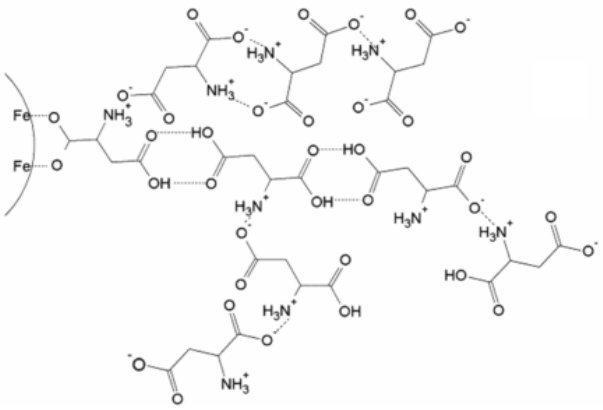

Figure 17. Association of amino acids in zwitterionic form (Adapted from [223]).

The second component of the adsorption interaction is the metal oxide surface, which is likewise pH-responsive. As for the amino acid, the metal oxide surface is also amphoteric[225] in nature and its overall net charge of the metal oxide in aqueous environment is pH-tuneable[226]. The isoelectric point (IEP) of the metal oxides studied in this thesis, magnetite and anatase form of titania, have been summarised below (Table 6). Magnetite and anatase (and metal oxides in general) present a negative charge

at pH above the IEP and a positive charge at pH below this crucial point. Understanding of the surface charge of the nanoparticle is also an important method to characterise their degree of functionalisation. Upon adsorption of functional molecules, a shift in isoelectric point is useful in first assessing the successful binding of the modifying ligand, and is further significant in charge-dependant processes such as protein adsorption.[193]

Table 6. Isoelectric point of iron and titanium oxides

Material	Isoelectric Point	Source
Fe_3O_4	6.8	[227]
Fe_3O_4	6.78	[228]
Fe_3O_4	6	[229]
Fe_3O_4	6.78	[230]
TiO_2 (Anatase)	5.8	[231]
TiO_2 (Anatase)	5.5	[232]
TiO_2(Anatase)	5.3	[233]
TiO_2(Anatase)	5.5	[234]
TiO_2 (Rutile)	3.2	[232]

In addition to the physi- and chemisorption configurations that can be expected from interaction with either the –COOH or $–NH_2$ group, the amino acid can also be involved in electrostatic interactions governed by the reaction pH and the overall charges of the molecule and the MOx surface. For example, it has been noted that the adsorption of L-aspartine[235] and L-glutamic acid[236] onto TiO_2 is promoted at a pH where the two bodies carry attractive opposite charges and is conversely inhibited when they carry repulsive like charges. It is important to realise that the local charge at the

functional group(s) of the amino acid may be more important than overall charge of the molecule. For example, although the zwitterion is neutral, the local charged -NH_3^+/-COO^- groups may still interact with the charged metal oxide surface.

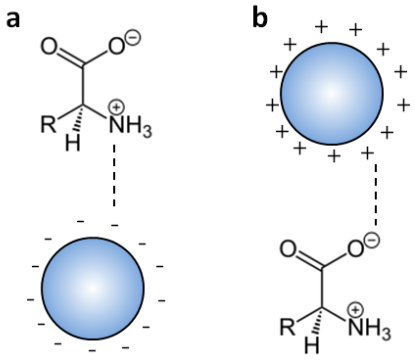

Figure 18. Electrostatic binding of amino acids to (a) negatively charged and (b) positively charge metal oxide nanoparticle surfaces.

In amino acids containing more than one –COOH group (such as glutamic acid), both carboxyls may be involved simultaneously in coordinating to the metal oxide surface. In fact, in glutamic acid, it is currently understood that this double binding action is dominant. This has an important implication on the overall surface chemistry of the resulting functionalised structure. Firstly, this will affect the zeta potential. A glutamate molecule that is bound by a single –COO- will present an overall net neutral charge (due to remaining free –COO-/NH_3^+), whereas one undergoing bidentate binding will present a net positive surface charge. Additionally, the bidentate binding configuration is more robust than the single-site binding. Both of these considerations are important for biomedical applications where the surface charge is crucial in determining both the interaction with biological moieties (e.g. DNA, protein binding) and the strength of the tethering functional molecule determines the robustness of the overall structure.

1.6 Intrinsically Conductive Polymers

The third type of nanomaterial of great biomedical importance is the class of intrinsically conductive polymers. They provide alternative routes towards controlled drug release via their unique photo thermal and electrochemical properties. As their name suggests, this class of materials is usually conductive with a switchable conductivity that is based on their oxidation state[237]. This ability to switch is the basis behind their electrochemically triggered drug release[238]. They have low energy bandgap transitions available, typically absorbing light in the visible and near infrared[239], compared with UV for TiO_2, and transforms this absorbed light into a local temperature increase[240] that can in turn trigger any nearby temperature-sensitive components[241].

The most important conductive polymers are:

(i) Polypyrrole (PPy)

This is arguably the most well-studied polymer for biomedical applications, due in part to its good *in vitro* and *in vivo* biocompability[242], good chemical stability in water[243] and relative ease of synthesis.

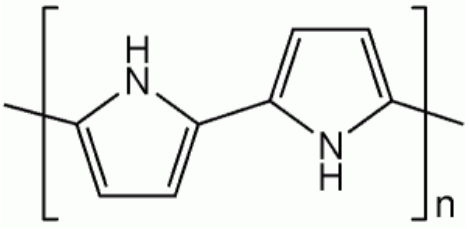

Figure 19.Chemical structure of polypyrrole (PPy).

(ii) Polyaniline (PANI)

The second most investigated after polypyrrole is polyaniline, which exists in in the following forms: pernigraniline base, half-oxidised emeraldine base, and fully reduced leucoemeraldine base[244]. These forms differ significantly in their conductivity, and electrochemical means may be used to switch readily between the forms.

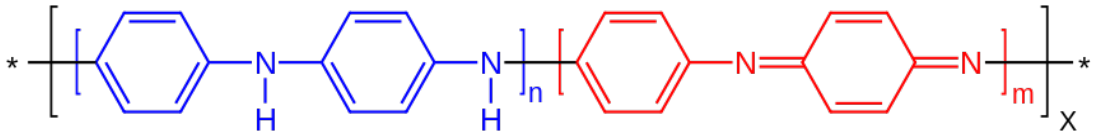

Figure 20. Chemical structure of polyaniline (PANI)

(iii) Poly(3,4-ethyl-enedioxthiophene) (PEDOT)

A third alternative is PEDOT, a polythiophene derivative that has better conductivity[245], but is less thermally stable.[246]

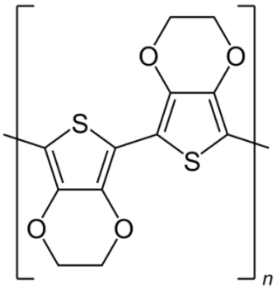

Figure 21. Chemical structure of PEDOT

1.6.1 Polypyrrole Synthesis

This dissertation focusses primarily on PPy due to its proven biocompatibility and easy route of synthesis that can readily be adapted to produce nanocomposites with the other materials of interest[247]. There are two routes towards the synthesis of polypyrrole: chemical and electrochemical polymerisation. In both cases, the monomer pyrrole is oxidised to produce a positively charged polymer backbone that is stabilised by the

inclusion of anions[248]. In the case of chemical polymerisation, a strong oxidant, typically ammonium persulfate (APS)[249] or iron (III) chloride hexahydrate ($FeCl_3.6H_2O$)[250] is used to initiate the reaction and counter ions included in the resulting product are the anions from this salt, sulphates (SO_4^{2-}) and chloride (Cl^-) respectively. Synthesis via the chemical route produces nanoscale polypyrrole particles in one step and is therefore a facile route that is preferred for drug delivery applications. Electrochemical synthesis uses applied potential (> 0.8V) as the driving force for oxidative polymerisation[251]. This method produces a coating of polypyrrole on the working electrode and is often used for coating of implants[252]. A schematic for the general reaction pathway resulting in oxidised polypyrrole has been included below (Figure 22).

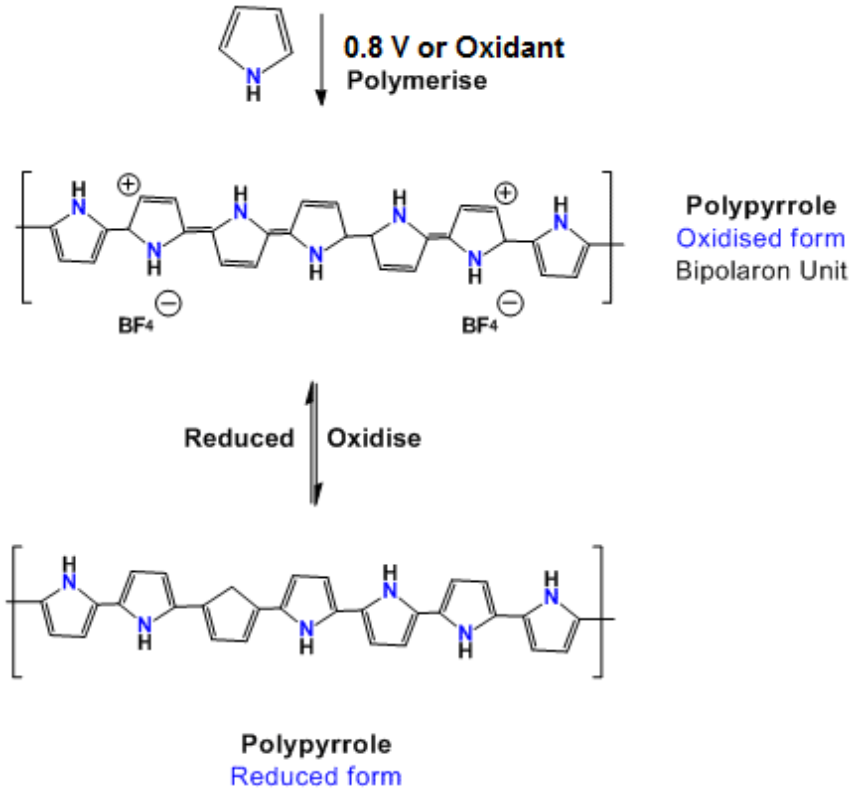

Figure 22. Polymerisation of polypyrrole by either electrochemical or chemical pathway.

Chemical routes are used in this work due to the ease at which these methods can be adapted to create functional nanocomposite structures applicable for drug delivery applications as compared with the bulk scale deposited film that typically result from electrochemical synthesis.

1.6.2 Electrochromic properties

The oxidised form of polypyrrole is also referred to as 'doped' polypyrrole due to the inclusion of the anionic dopants. In the doped form, the polymer is conductive due to the formation of polarons (single positive charges) or bipolarons (double positive charges) spread over four pyrrole units, whose distortion in the polymer chain relaxes the high stresses within the five member ring and thus create lower energy states below the conduction band.[253] Bredas et al's landmark investigation on the evolution of the band structure upon successive doping show that the main gap at 3.2 eV of undoped PPy is joined by additional transitions at 0.7 eV, 1.4 eV and 2.1 eV.[254] Thus, a doped polypyrrole absorbs strongly in visible and near infrared ranges. Furthermore, PPy is electrochromic, that is, its optical and electrical properties are strongly linked. For this reason, the optical absorbance of a PPy sample is a useful tool to determine the sample's oxidation state and doping content. [255-258]

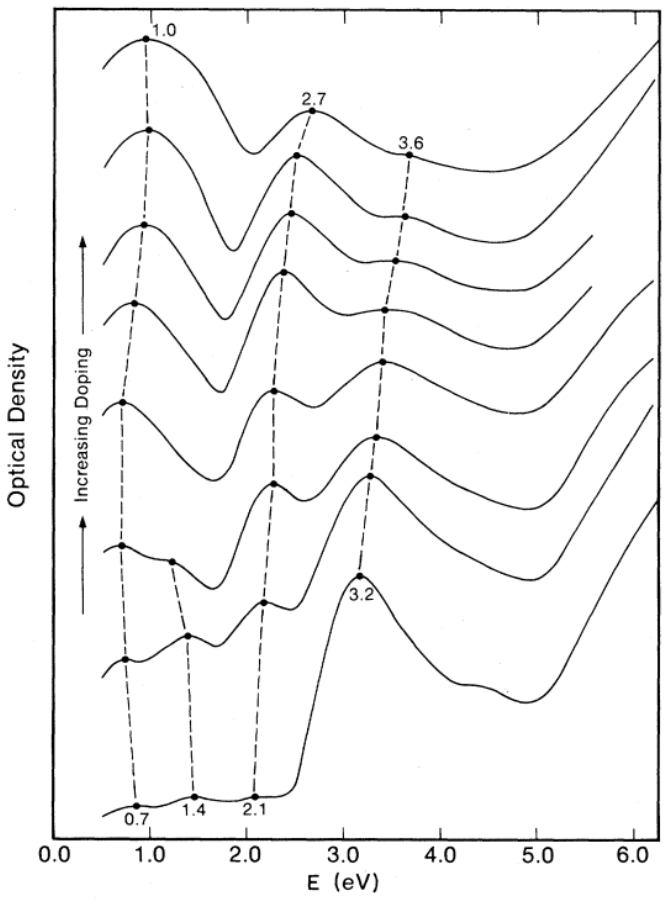

Figure 23. Evolution of optical absorbance of polypyrrole upon successive doping content.[254]

1.6.3 Doping and dedoping

There has bene a recent push towards doping PPy with useful anionic molecules instead of the anions from the oxidant salt or electrolytes to create electrochemically triggered load and release systems. This can be accomplished by including a suitable, negatively charged molecule in the typical polypyrrole synthesis, whether it be by the chemical or electrochemical route. Examples include biotin[259], dexamethasone[260] and neurotrophic proteins[261], all of which can be successfully incorporated in the PPy by including the dopant in the reaction mixture at the point of polymerisation. This versatility has led to the proposal of PPy as a material for drug delivery[262] in both its nanoparticle and film forms. The ability to include proteins, particularly growth factors,[263] makes PPy a

preferred material for implant coating as these bound growth factors can significantly increase the growth of cells over the PPy surface and thus implant integration is improved[264].

These materials may be subsequently dedoped in one of two methods. The most common is to forcibly reduce the PPy by applying negative potential. This neutralises the charge on the polymer backbone and forcibly ejects the bound anion.[265] Electrochemical dedoping has proven to have a high efficiency and is a preferred method for drug delivery from polypyrrole films[238]. Although this is most applicable to electrodes coated in the PPy, there has been a recent landmark study using electric field penetration in vivo to accomplish the same on PPy nanoparticles.[266] Dedoping can also be triggered by changes in pH. It has been observed that treatment with alkaline media will also result in removal of the dopants[267]. This gradual loss of bound anions has also been observed at physiological pH (in PBS) and has been utilized for the gradual, passive release of bound anti-inflammatory drugs.[268]

1.6.4. Photothermal responses

In addition to electrochemical triggers, PPy also has a strong photo-responsive to light matching the wavelengths of its main bands (0.7eV, 1.4eV, 2.1eV and 3.2eV). Its photothermal response (a conversion of this absorbed light into local increases in temperature) has been well-documented This has been used directly for photothermal therapies such as the ablation of cancer cells.[240] Additionally, this local increase in temperature can be used in conjunction with temperature-sensitive components such as labile linkers[241] and hydrogels[269] for controlled release.

1.6.5. Polypyrrole and amino acids

As for TiO_2 and Fe_3O_4, the use of amino acids with polypyrrole has garnered some interest in recent years due to their biological importance coupled with their amphoteric and sometimes ambiguous chemistry. Overall, work in this area is rather limited compared with metal oxide functionalisation. Meteleva-Fischer et al. first observed that glutamic ions could be incorporated in electrochemically synthesised PPy[270], and Valencia et al. subsequently reported that their inclusion served as a tethering point for the controlled release of amoxicillin.[271] However, these works stand alone in the literature and do not present any detailed, systematic study of how this doping may be optimised.

1.6.6 Literature survey of polypyrrole as a nanocarrier

A literature survey is presented below (Table 7) for the current biomedically important results pertaining to PPy.

Table 7. Polypyrrole for biomedical applications

Structure	Synthesis Route	Dopant	Application	Mechanism	Source
Hollow Sphere	Chemical	Di(2-ethylhexyl) sulfoscuccinate	Photothermal ablation	NIR laser (808nm)	[272]
Sphere, 45nm	Chemical	Cl^-	Photothermal ablation	NIR laser (808nm)	[273]
Sphere, 100nm	Chemical	Cl^-	Photothermal ablation	NIR laser (808nm)	[274]
Sphere 50nm	Chemical	Cl^-	Photothermal ablation	NIR laser (808nm)	[275]
PPy on Mesoporous Silica	Chemical	Cl^-	Photothermal ablation	NIR laser (808nm)	[276]
Sphere, 85nm	Chemical	SO_4^{2-}	Photothermal release (FITC-albumin)	NIR laser (808nm)	[277]
Sphere, 27nm	Chemical	Cl^-	Photothermal release (Vancomycin)	NIR laser (808nm)	[278]
Hollow Sphere	Chemical	SO_4^{2-}	Photothermal release	NIR laser (808nm)	[279]
Film	Electrochemical	Toluene sulfonic acid	Electrochemical Release (Dexamethasone)	±0.6 V vs Ag/AgCl at 0.5 Hz in PBS NIR laser (808nm)	[280]
Film	Electrochemical	sodium dodecylbenzenesulfonate	Electrochemical Release (Biotin)	±3.0V vs Pt wire mesh at 0.003 Hz	[259]

Film	Electrochemical	toluene-4-sulfonic acid	Electrochemical Release (Heparin)	0 to 3.5 mA were applied and the heparin release was monitored for 120 min	[281]
Film	Electrochemical	para-Toluene sulphonic acid	Electrochemical Release (neurotrophin-3)	± 0.5 mA and ± 20 mA) at 5 Hz	[282]
Sphere	Chemical	Cl^-	Electrochemical Release (fluorescein, daunorubicin)	-4.5 V/cm electric field	[266]
Granule Aggregate	Chemical	L-serine L-glutamic acid	Electrochemical Release (amoxicillin)	±5 V were applied for 2 min between the two electrodes in intervals of 30 min.	[283]
Sphere	Chemical	None	pH Release (fluorescein sodium, rhodamine 6G)	pH change between physiological (7.4) and tumour site (6.5)	[284]
Sphere <10 nm	Chemical	Cl^-	Passive Release (Ketoprofen)		[268]

1.7 Biocompatibility

It is important to consider the biocompatibility of all nanomaterials for any application that involves interfacing with biological systems. Many factors may influence the acceptability of the nanomaterial in question to a living system, including the toxicity, dispersity, retention and cell adhesion. The inherent toxicity of nanomaterials remains a hotly debated topic, with several studies indicating the size-dependant toxicity of sub 100nm materials, while others refute these claims. The materials of main interest in this thesis (TiO_2, Fe_3O_4, and PPy) differ significantly in their biocompatibility. The following factors are generally understood to be important in determining the overall biocompatibility of the structure:

(i) Solubility

(ii) Radical Oxygen Species Generation

(iii) Particle size and shape

(iv) Surface charge

(v) Retention

(vi) Cell adhesion

1.7.1 Solubility

The stability of the material within the media of interest (usually the bloodstream[285] or other extracellular fluids[286]) is a generally an important factor in determining the cytotoxicity of various nanomaterials[287]. For example, a study conducted on flame-made oxide nanoparticles of similar size and shape (spherical, ca. 10-50nm) concluded that a relatively low concentration (ca. 3.75ppm) of slightly soluble iron oxide caused significant cell death, while comparable concentration of insoluble titanium oxide and silica did not cause any loss of cell viability.[287] This highlights the importance of

increasing the chemical stability of the nanostructure surface for slightly soluble materials. For example, iron oxide nanoparticles intended for biomedical applications are usually coated in either chemically inert SiO_2[288] or a polymer such as polystyrene.[289]

On the other hand, PPy is insoluble at in physiological conditions, remaining stable up to 14 days[290], although beyond that it may undergo some subtle reduction in conductivity[291], likely due to interaction with salts in the system.

1.7.2 Radical Species Generation

Although TiO_2 is insoluble and does not cause cell death via dissolution, it becomes toxic due to the photocatalytic production of reactive oxygen species (ROS) at the nanoparticle surface. ROS is considered an exemplary nanotoxicity pathway that is known to stimulate inflammation[292] as well as to initiate pro-apoptotic[293] cell signalling.

Upon illumination by light of the correct wavelength, electrons (e^-) and holes (h^+) are generated at the TiO_2 surface, which then go on to initiate the formation of radical OH· and peroxide (H_2O_2) [37] (see Chapter 2 *Section 1.1*). Both species are highly oxidising and may be thus toxic to cells. Studies to date have concluded that while TiO_2 nanoparticles without light illumination are relatively benign (up to 100ug/mL)[294], cytotoxicity is significant upon exposure to UVA and may be attributed directly to the radical OH generation.[295]

Similarly, the presence of PPy may stimulate generation of ROS through innate immune responses. Studies have observed that the ROS value may reach 58% at a PPy concentration of 500 μgmL^{-1} and is correlated with peak cell death rates, far exceeding that by phagocytosis.[296]

Although ROS generation is highly damaging to tissue, it is not entirely a disadvantage. For example, it has been observed that when TiO_2 is used at tumour sites, there is a marked synergistic effect when UV irradiation is used in conjunction with targeted delivery of anticancer drugs.[297] However, it is important to note that in such circumstances it is vital to have good control over location of nanoparticles only at the cancerous sites, to which end the use of an Fe_3O_4 core and/ or targeting molecules is helpful.

1.7.3 Particle Size and shape

It has been proposed in recent years that materials that may be chemically inert (insoluble) in physiological conditions (such as TiO_2, SiO_2, even noble metals[298]) may become toxic when their size is small enough for biological interaction[299]. However, there is currently a lack of consensus in the literature to date on the origins of this effect, if it is indeed true, and what the crucial cut-off sizes are for various materials. For example, while size matters for most metal oxides, with nanoparticles being more toxic than microscale counterparts, it was conversely observed that microscale TiO_2 may be more toxic due to the higher photocatytic efficiency of larger, more crystalline particles and subsequent increased ROS generation.[300] The same study found that there was no difference between micro- and nanoscale Fe_2O_3 and Fe_3O_4 particles.[300] This sentiment seems to be supported by Warheit at al. who observed no difference between rutile and anatase at 10nm compared to 300nm, and furthermore recorded no difference between spherical particles and rods.[301]

1.7.4 Surface Charge

Additionally, there is emerging evidence that nanoparticle surface charge may be important in determining its toxicity via cellular uptake. Cationic, or positive-charged, nanoparticles cause more pronounced disruption of the plasma-membrane integrity,

stronger mitochondrial and lysosomal damage and a higher number of autophagosomes than equivalent anionic particles.[302] This is a significant consideration for functionalised nanoparticles. Although both bare TiO_2[303] and Fe_3O_4[304] are negatively charged at physiological pH (7.4), many functionalization strategies result in the amination of this surface and thus positively charged carriers.[305] It is noteworthy that polypyrrole is usually negatively charged despite its cationic polymer backbone due to the presence of anionic dopants.

Another factor to consider is the influence of the overall particle surface charge on the degree of flocculation. It is generally required that nanoparticles are well-dispersed to avoid forming large structures within the body that may cause clogging of vital functions. Flocculation of nanoparticles in solution is strongly dependant on the zeta potential. In general, the overall charge magnitude correlates to the degree of electrostatic repulsion between the particles. Thus, the higher the zeta potential, the greater is the dispersity of the nanoparticles. On the other hand, the closer the zeta potential is to zero, the greater is the flocculation. This effect is studied in some detail in Chapter 3 and 4.

1.7.5 Retention

It is also important to consider the ultimate fate of the nanocarrier, whether it is passed through the body or retained at injection sites. In general, it is desirable to design 'stealth' nanocarriers that are not recognised and have minimal interactions with biological components outside of the chosen performance. Due to the novelty of the field, long term studies on the effect of retained nanoparticles are missing. Given this knowledge gap, most studies suggest that a cautionary stance should be taken with a view towards promoting clearance of nanoparticles out of the system. The interaction

with voracious cells of the mononuclear phagocyte system (MPS) is of key importance. Although this forms the basis of drug delivery where cellular uptake of the particles themselves are required[306], in other designs this must be avoided if nanoparticles are to be cleared from the system after they have performed their function.[307] Here, shape and size may play a role that is distinct from their poorly understood effect on toxicity. Studies have shown that larger and more anisotropic particles show greater tendency towards retention within the organs.[308] This is an important consideration in view of the recent surge in interest in rods[309] and fibres[310] over spherical carriers due to the additional, unique capabilities of anisotropic structures. In an ideal scenario, the shape-factor of the nanocarrier should be tuneable, and results towards this are discussed in *Chapter 4.*

1.8 Research Questions

Given the current state-of-the-art and knowledge gaps identified so far in this chapter, this dissertation will focus on the synthesis and optimisation of exogenously stimulated structures based on light and magnetoresponsive materials primarily for controlled drug release applications. Based on the literature review conducted, of particular interest are titania (TiO_2), a strong photocatalyst, magnetite (Fe_3O_4), a superparamagnetic form of iron oxide, and polypyrrole (PPy), a photothermal and electrically conductive polymer. The photocatalytic response of TiO_2 may be used for light-activated molecule release[23] as well as redox-assisted treatment of cancer cells.[311] Magnetic nanoparticles are useful as they allow for magnetic field targeting[91], MRI imaging[312] and magnetothermal therapy[94]. Polypyrrole has been successfully used for electrochemical drug delivery[282] and photothermal therapy[313].

In the case of TiO_2, there remain some fundamental questions on mechanism of the apparent photocatalytic release reported by some authors to date. There remains some disagreement on the fate of the adsorbed functional molecules upon irradiation with UV light and subsequent electron/hole generation. It is currently unclear whether the functional molecule degrades due to photcatalysis at the TiO_2 surface, or if photocatalysis simply results in the photocleavage of TiO_2-functional molecules instead. Both have been reported in literature to date. Distinction between the two is of vital importance in drug delivery applications for two reasons. Firstly, it is important to preserve the whole, undamaged structure of the pharmaceuticals that have been released in order to maintain efficacy. Secondly, it is important to minimise the evolution of side products that may have unknown impact on the biological environment.

The functionalisation of TiO_2, Fe_3O_4 and PPy is an active field with many strategies currently in use. Amino acids are the focus due to their high biocompatibility and proven ability to delivery useful moieties such as DNA[210], proteins[314] and prodrugs[315]. Additionally, the amphoteric nature of amino acids leads to ambiguous interaction with the nanomaterials in question. For example, they can bind by either –COOH or $–NH_2$ groups of the amino acid, with a current lack of unified study over the effect of various reaction parameters on this binding mode. In the case of PPy, it is known that the material can only be doped with anionic functional molecules. Yet, there is a lack of systematic study on inclusion of amino acids under variable reaction pH. These questions do not currently have solutions and would benefit from a thorough investigation.

To summarise, the following key qeustions form the basis of this thesis:

1. What is the mode of apparently reported TiO_2 photocatalytic drug release?
2. What is the impact of reaction parameters, particularly pH, on amino acid binding to various metal oxide nanoparticles?
3. How can the configuration of the above be optimised for delivery of desired moieties?
4. What is the effect of amino acid functionalisation on the flocculation of the nanoparticles?
5. What is the subsequent effect of this flocculation on the usefulness of the structure?

These fundamental questions have not yet been adequately addressed in the literature. Therefore, their investigation constitutes a novel and valuable contribution to the field.

CHAPTER TWO

Amino Acid Functionalisation of Metal Oxide Nanoparticles

Published with modifications:

Zhang, T., M. A. Go, et al. (2015). "Low-cost photo-responsive nanocarriers by one-step functionalization of flame-made titania agglomerates with L-Lysine." Journal of Materials Chemistry B **3**(8): 1677-1687.

Chapter Overview

This chapter covers the synthesis of flame-made metal oxides (SiO_2, TiO_2 and iron oxides) and their subsequent functionalisation with the amino acids L-lysine and L-glutamic acid. In particular, it focusses on the effect that the reaction pH has on the resulting zeta potential, particle flocculation / self-assembly and reactive amine content as indicated by an amine-reactive fluorescent label. Furthermore, for TiO_2, an important photocatalyst, the time-dependant release of the surface-bound functional molecules under exposure to UVA light is shown. The release of the bound amino acid is shown to be crucially time-dependant, with the onset of a photocatalytic decomposition via a cyclisation pathway occurring after ca. 10s. A model drug, the anti-inflammatory ketoprofen, is then loaded to the active -NH_2 of the material. It is shown that in such circumstances the photocatalysis breaks the bond between the amino acid tether and the loaded pharmaceutical, releasing the drug as an unmodified molecule, demonstrating the usefulness of this nanocarrier for the light-triggered delivery of biologically important and highly specific compounds. A schematic of the overall functionalisation – release process is provided in figure 24.

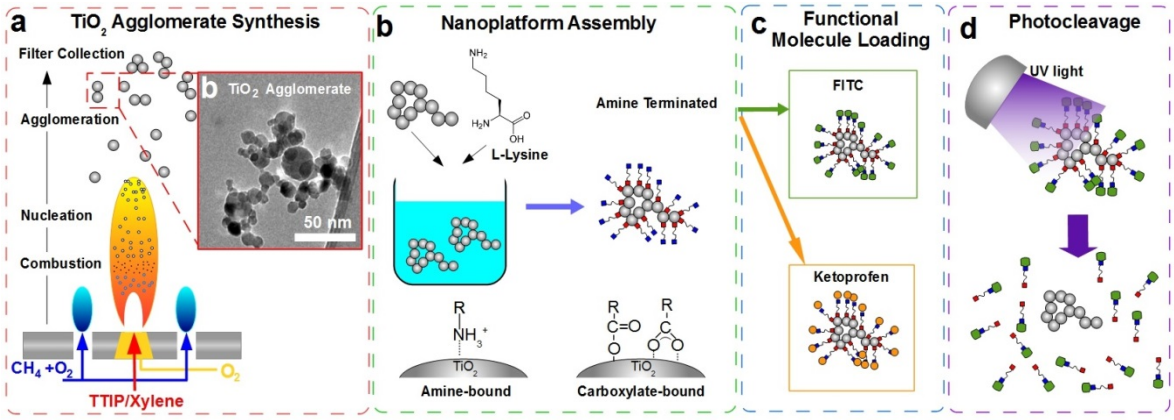

Figure 24. Chapter three overview. (a) FSP-synthesis of metal oxide nanoparticles. (b) Functionalisation using amino acids at different pH resulting in different coating morphology. (c) Exploiting –NH_2 termination for attachment of FITC dye or ketoprofen. (d) Exposure of photocatalytic TiO_2 to UV light for release of the functional molecules.

2.1 Introduction

Metal oxide based nanomaterials have recently gained much interest in the field of drug release for both passive and active/ selective release systems, as previously discussed in Chapter One. TiO_2 is popular in this field due to its photocatalytic properties that allow for light-triggered, controlled release[16], while Fe_3O_4 contributes useful superparamagnetic properties[90] and SiO_2 is ubiquitous in applications that required chemically inert biomedical coating[81] or passive porous carriers[79]. These three materials demonstrate currently ambiguous amino acid adsorption, despite their prolific use in the field, and poses one of the fundamental research questions of this thesis. Therefore, this chapter aims to investigate the role of pH on the adsorption of amino acids on TiO_2, SiO_2 and Fe_3O_4 surfaces and optimise with respect to loading of $–NH_2$ reactive deliverable molecules.

2.1 Synthesis of MO_x nanoparticles and their material properties

Nanoparticles were synthesised using flame-spray pyrolysis due to the high yield of crystalline, pure nanoparticles in the size range 5-50nm produced by this method.

Both SiO_2 and TiO_2 were produced at previously established standard reaction conditions for the flame reactor (5 bar nozzle pressure, 5mL/min precursor feed rate, 5L/min dispersion oxygen). Micrographs showing the typical products obtained are shown in Figure 25. The SiO_2 was amorphous with d_{TEM} ca. 10nm , consistent with previous reports[316]. TiO_2 produced was ca. 20nm with a facetted shape that is also consistent expectations.

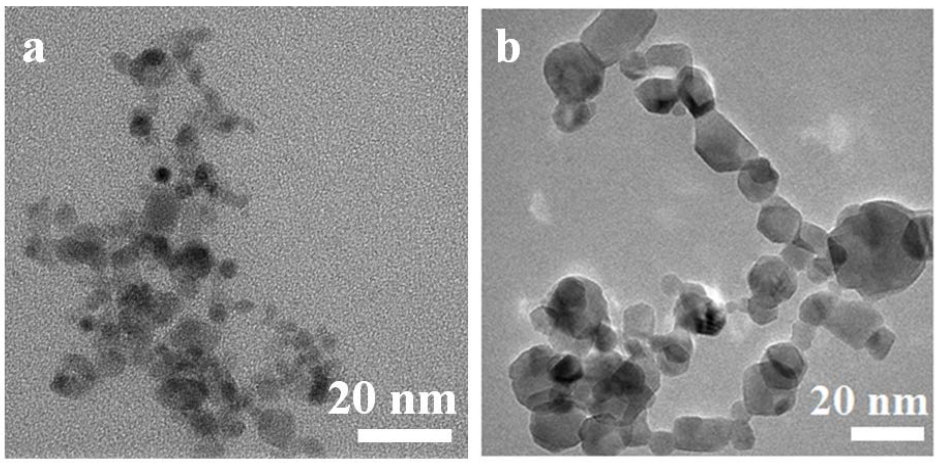

Figure 25. TEM showing (a) SiO_2 and (b) TiO_2 NPs synthesised at 5/5/5 flame conditions.

XRD was performed to determine the crystal structure of TiO_2 (Figure 26 a) and revealed a predominantly anatase phase (A, between 87.1% and 80.0%) with a small content of rutile (R, between 12.9% and 20.0%). Due to the higher photocatalytic activity of anatase relative to that of rutile[317], it is advantageous to have of a higher content of anatase. It has also been suggested that a mixture of anatase and rutile that typically results from flame-spray pyrolysis routes may in fact have an enhanced photocatalytic efficiency compared to pure anatase alone. This is due to a synergistic interaction with the rutile phase, with a reported optimal content of ca. 39mol% anatase identified for water splitting efficiency.[318] However, here, phase composition was not optimised further as this is outside the primary aims of this dissertation.

The nanoparticle band gap was obtained from the UV-vis absorbance spectrum (Figure 26 b) as approximately 390 – 400 nm (3.2 eV) using the Tauc plot method and comparable to previously reported values for flame-made TiO_2 of similar size.[319]

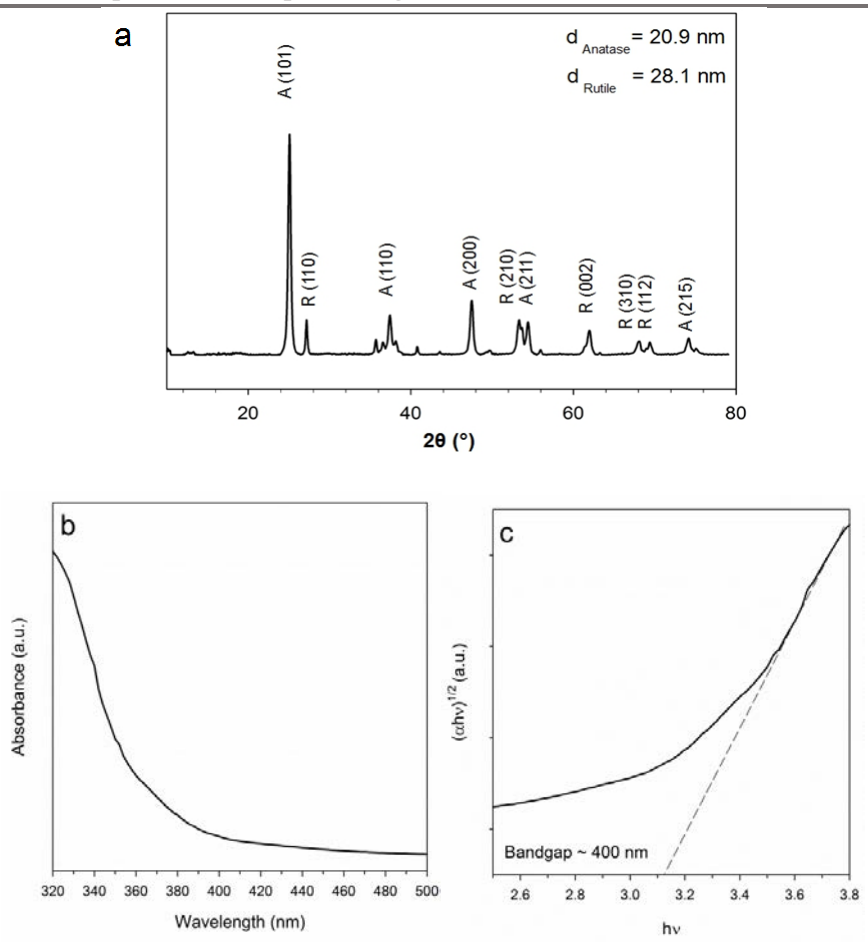

Figure 26. (a) XRD Spectrum of flame-made TiO_2 nanoparticles showing Anatase (A) and Rutile (R) phases. (b) Optical absorbance of TiO_2 and (c) Tauc plot showing bandgap at ca. 390nm.

Due to the range of iron oxides compositions that are possible via flame-spray pyrolysis, the synthesis parameters were altered systematically in an attempt to optimise the resulting product's composition and magnetic properties. It was found that the flame reactor was highly sensitive towards the synthesis conditions, in particular the nozzle pressure drop, and would produce clean combustion only at 5bar ±1 bar. Outside of this pressure, poor atomization was observed during combustion and, and in some cases a black residue was formed that is characteristic of incomplete combustion. Therefore, the pressure was fixed at 5 bar while the governing parameter $[Fe]/O_2$ [mol/L][172] was changed by altering the dispersion oxygen and feed rates.

It was discovered that the overall nanoparticle size (d_{BET}) was directly proportional to the [Fe]/O_2 mol/L concentration in the system at a constant 5 bar pressure (Figure 27).

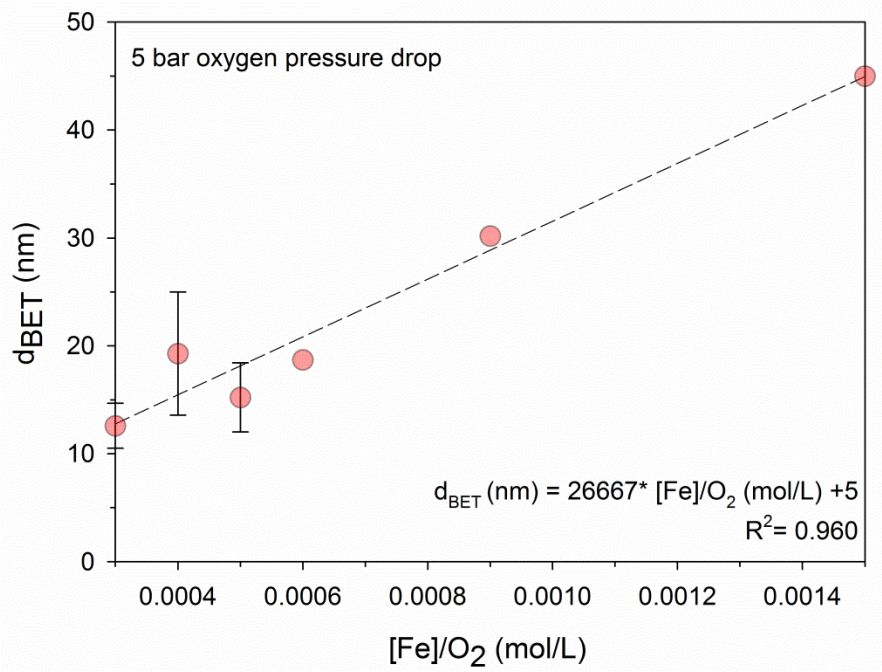

Figure 27. Particle size of FSP-made iron oxide nanoparticles as a function of [Fe]/O_2 (mol/L) at constant 5bar pressure.

It is usually desirable to reduce the size of the nanoparticle as it is their small size that is advantageous in many applications. Based on these results, a smaller [Fe]/O_2 ratio is favourable in this respect. However, in the case of iron oxides, optimisation of the product must also take into account the phase composition(s) produced across the reaction parameters as the phase of the iron oxide together with the size determines its magnetic properties. It was found that the nanoparticles produced were mixtures of hematite and magnetite (Figure 28, Figure 29) and is consistent with previous reports. To date, mixtures of hematite, maghemite[177], magnetite[177] and wustite[177] have been reported for iron oxides produced by the FSP method. Due to the desirable superparamagnetic properties of magnetite (Fe_3O_4) over the other phases of iron oxides,

the synthesis was optimised with a view to maximising the content of Fe_3O_4. It was discovered that the optimal conditions to produce Fe_3O_4 were 6 mol/L [Fe^{2+}] precursor concentration, 5L/min dispersion oxygen, 5 bar oxygen pressure, producing a nanoparticle of ca. 20nm size (d_{BET} = 20nm, d_{TEM} = 17nm) that is ca. 98% Fe_3O_4 / 2% Fe_2O_3 (Figure 28, Green line).

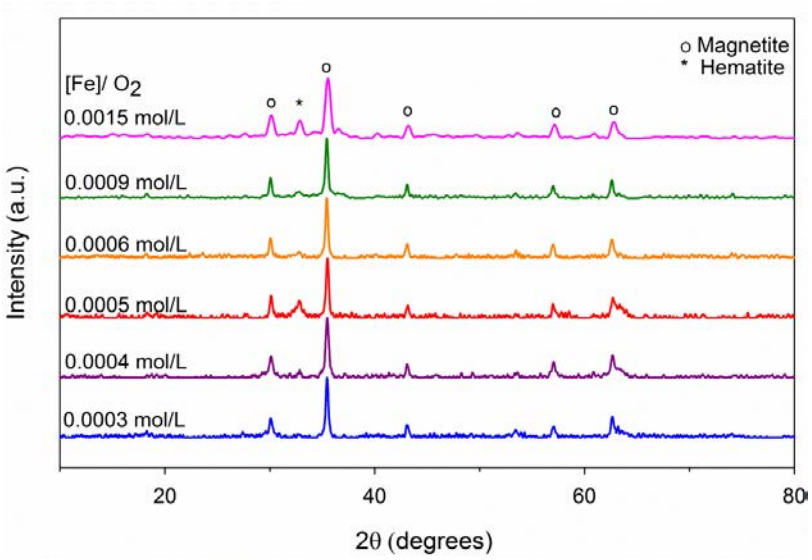

Figure 28. XRD spectra of FSP-made iron oxide NPs as a function of [Fe]/O_2 at constant 5 bar pressure.

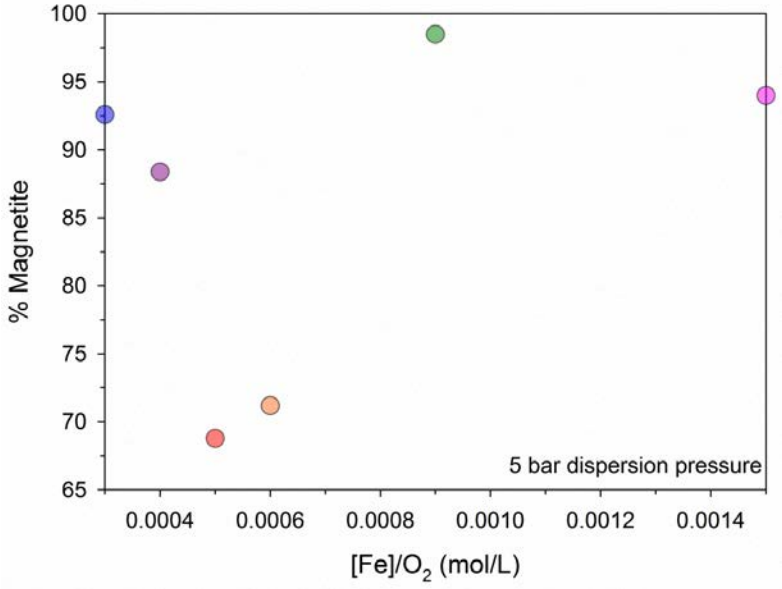

Figure 29. Magnetite weight content of FSP made iron oxide NPs as a function of [Fe]/O_2 at constant 5 bar pressure.

Finally, the magnetic properties of the flame-made iron oxides were assessed by magnetic hysteresis and compared against a commercially available Fe_3O_4. These results were in good agreement with the phase composition data obtained by XRD, showing a maximum saturation magnetisation for the sample that contained the highest magnetite content (Figure 30, green line). However, this value was still approximately 50% lower than that of the commercial Fe_3O_4 (Figure 30, black line). This can be attributed to the difference in the nanoparticle size. The commercial magnetite has a reported size of ca. 50nm, while the flame-made is ca. 30nm. This is consistent with the expect increase in magnetisation as the particle size increases.[320] Additionally, the crystallinity is expected to differ between the products. The flame-made nanoparticles had a quasi-spherical shape with slight faceting compared with the highly geometrical cubic shape of the commercial product. The TEM and size distributions of typical commercial and flame-made iron oxides are included in Figure 31. A high magnetisation is generally an advantage as it implies the ability to induce a stronger magnetic field with the material (and from there, stronger secondary responses for magnetic motion, or magnetotherapy) requiring a weaker externally applied field.

However, this desirable quality should always be balanced by other properties. One is the particle size, always important in drug release, and another is the remanence and coercivity of the material. Truly superparamagnetic materials have a remanence and coercivity close to 0, meaning that they lose all magnetisation upon removal of the external source. This is important as it is typically not desirable to have nanoparticles that behave as weak ferromagnets after the external field is switched off. For example, they may experience attractions leading to flocculation and formation of large structures that may obstruct blood vessels or otherwise be disruptive. The remanence values were

tabulated alongside the magnetisation at 1T (Table 8) for each product synthesised alongside commercial magnetite.

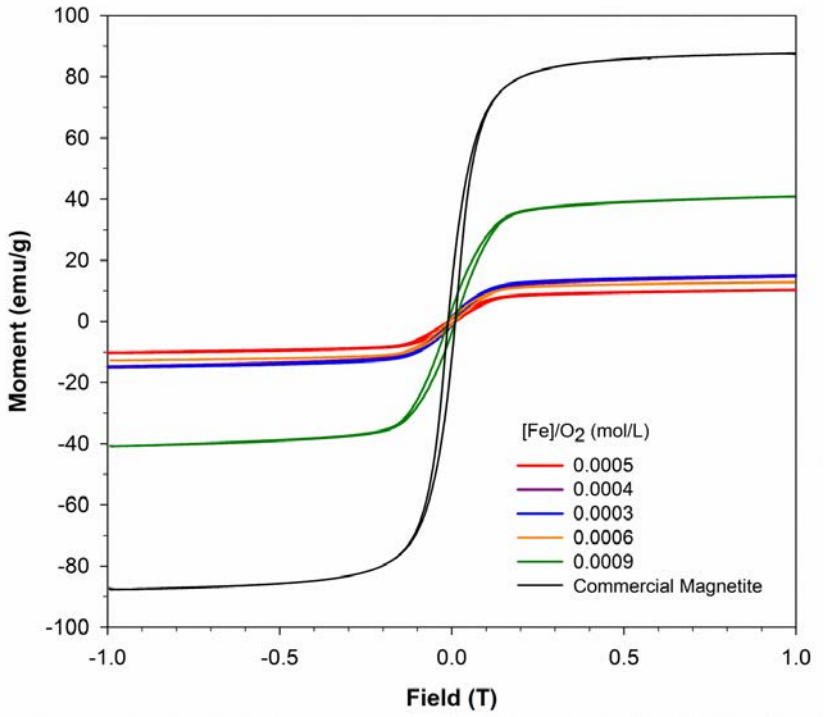

Figure 30. Magnetic hysteresis of flame-made iron oxides at various [Fe]/O_2 concentration and fixed 5bar pressure drop (coloured lines), compared against commercial Fe_3O_4 NPs (black line).

Table 8 Remanence and magnetisation at 1T for flame-made and commercial magnetite.

[Fe]/O_2 (mol/L)	% Fe_3O_4	Size (nm)	Magnetisation at 1T (emu/g)	Remanence (emu/g)
0.0003	92.5	13	14.20	0.784
0.0004	88	19	15.19	0.957
0.0005	68	15	13.71	0.739
0.0006	71	18	12.88	1.09
0.0009	98	28	40.98	3.77
Commercial Magnetite	100	50-80nm	89.27	9.41

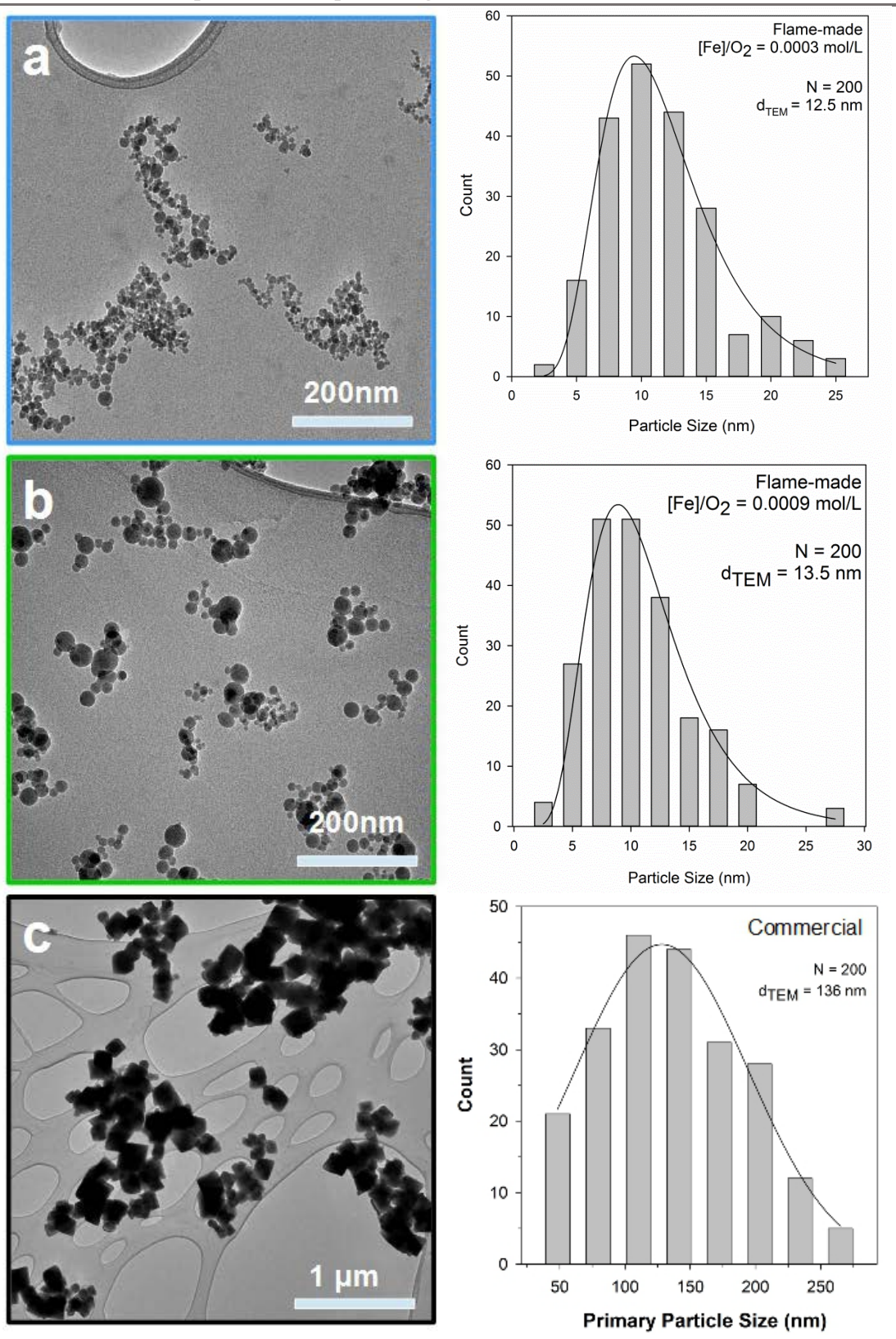

Figure 31. TEM and size distributions for (a) flame-made at $[Fe]/O_2$ = 0.0003 mol/L, (b) flame-made at $[Fe]/O_2$ = 0.0009 mol/L, and (c) commercial iron oxides.

2.2 Adsorption of amino acids

SiO_2, TiO_2 and Fe_3O_4 (flame-made at $[Fe]/O_2$ = 0.0009 mol/L) nanoparticles were then used for the adsorption of amino acids from aqueous media under variable pH. The amino acids used for these experiments were L-glutamic acid and L-lysine, chosen for their importance for further biomedical applications as well as their contrasting acid-base character (L-lysine being a basic type and L-glutamic acid being an acidic type). Three pHs were investigated: pH 7 (water), pH 10 (adjusted by the addition of NaOH) and pH 2 (adjusted by the addition of HCl).

The zeta potential was recorded between the bare nanoparticles suspended in water and those with adsorbed amino acid(s). Table 9 shows the zeta potentials in water measured for the flame-made nanoparticles used in this thesis. TiO_2, the most important material in this study, was further titrated, and its isoelectric point was identified as 3.5 (See *Appendices*) Upon adsorption of amino acids, the measured zeta potential changed significantly due to the contribution of the charged $-NH_3^+/-COO^-$ groups towards the surface charge of the functionalized nanoparticle. Depending on which group(s) are involved in the binding of the molecule at the nanoparticle surface and which groups are left exposed, the charge state of the overall structure is expected to differ. For example, in the case of L-lysine, expressed in $–(\alpha)\text{-}NH_3^+/(\gamma)\text{-}NH_3^+/\text{-}COO^-$ at pH 7, if $–COO^-$ is involved in the amino acid adsorption, the remaining $(\alpha)\text{-}NH_3^+/(\gamma)\text{-}NH_3^+$are expected to contribute a positive charge to the structure, and vice versa.

The adsorption of amino acids onto the nanoparticle surface is also expected to have a significant effect on the flocculation dynamics of the system. This is due to the strong effects of electrostatic attraction and repulsion. For example, two neighbouring highly charged nanoparticles will repel one another. On the other hands, there is the potential of strong attraction between the neighbouring $–NH_3^+/-COO^-$ groups of amino

acids giving rise to the potential of agglomeration via electrostatically stacked nanoparticles. Thus, the changes in the hydrodynamic diameter were recorded alongside zeta potential for all samples. Initially, adsorption from water (pH 7) was studied for all three nanoparticles (Table 9).

Table 9. Evolution in zeta potential and hydrodynamic diameter of metal oxide nanoparticles after adsorption of L-lysine from aqueous (pH 7) solution.

	As Prepared MO_x NPs		**Lysine-MO_x pH 7 (water)**	
	Zeta Potential (mV)	Hydrodynamic Diameter (nm)	Zeta Potential (mV)	Hydrodynamic Diameter (nm)
SiO_2	-22.6 mV	160 nm	-3.8 mV	3181 nm
Fe_3O_4	-27.5 mV	226.5 nm	+14.7 mV	1324 nm
TiO_2	-25 mV	180 nm	+9.0mV	2000 nm

Several observations come from these results. Firstly, it is worth noting that the hydrodynamic diameter increases drastically generally from ca. 150-200nm by a factor of approximately 10 to ca. 1500-3000 nm. This suggests that the adsorption of L-lysine does indeed increase the flocculation dynamics of the system, consistent with existing theories.[321] This also suggests that adsorbed amino acids may indeed be used to assemble the nanoparticles into larger, more complex structures via the electrostatic interactions between activated $-NH_3^+$ and $-COO^-$ of neighbouring amino acids that act as bridges between the attached nanoparticles.

This phenomenon is later exploited (see *Chapter Three*) to direct the assembly of iron oxide anisotropic structures. However, this tendency to associate into larger structures needs to be monitored/controlled as the small size of nanoparticles is one of their most desirable features of nanoscale loading and release systems. The small size scale allows for their movement away from their injection / implant point, for example, and their subsequent diffusion through biological system. The small size of nanoscale

materials also gives rise to the large surface that define their difference from their bulk counterparts. In this application, the high surface area offered by small particle sizes serves as the high capacity platform for the loading and release of functional molecules. The formation of large, densely assembled structures is a detriment in both aspects.

It should be noted that over the same reaction conditions (24 hours, pH 7), the degree of functionalisation as assessed by the positive shift in the zeta potential is not equal between the three metal oxide nanoparticles studied. It is apparent that Fe_3O_4 nanoparticles arrive at the highest positive potential followed by TiO_2 and finally SiO_2. This shift is related not only to the overall concentration of positive-contributing L-lysine molecules adsorbed, but is also suggestive of the preferred adsorption orientation of the amino acid. It can be expected that the positively charged products (Lys-Fe_3O_4, Lys-TiO_2) should contain a higher surface coverage of free, reactive amine groups compared with the negatively charge product (Lys-SiO_2). This is largely consistent with literature. Although the interaction between amino acids and TiO_2 and SiO_2 surfaces is ongoing,[322] the adsorption of -COOH groups onto iron oxides is currently well-established.[323]

With respect to subsequent binding of proteins, viral vectors and formation of useful prodrugs, it is generally advantageous to promote higher available, reactive amine content[324]. Thus, experiments were performed to determine the effect of pH and amino acid concentration on the charge state of AA-functionalized TiO_2 to optimise this material for subsequent reaction steps. For L-lysine, it was clear that the reaction pH has a significant effect on the overall zeta potential and hydrodynamic diameter (Figure 32). In particular, we note that acidic conditions favour the adsorption of L-lysine to form positively charged, relatively colloidally stable structures. This is line with studies that show that adsorption of carboxylates is preferred under acidic conditions[325].

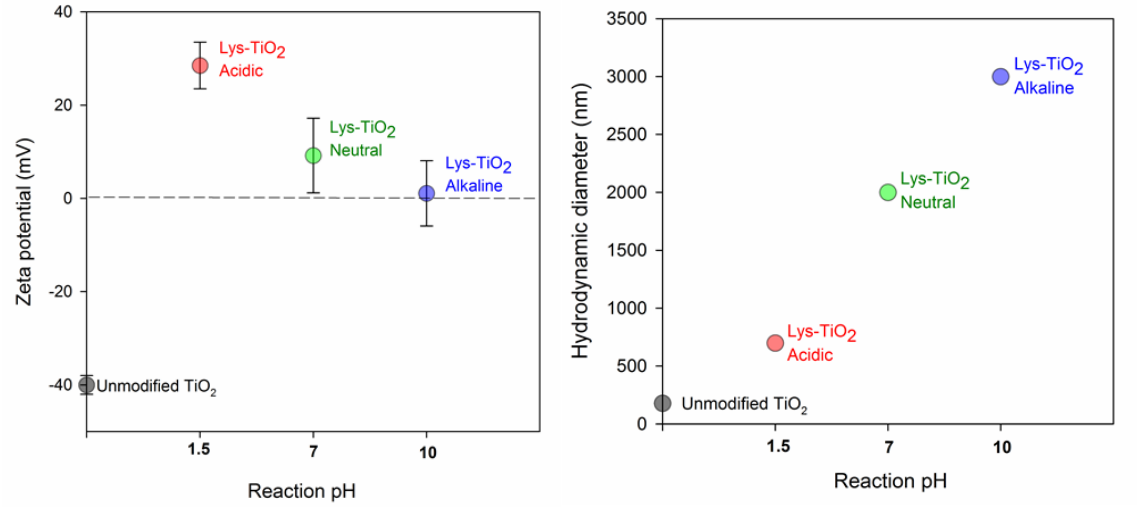

Figure 32. Evolution of (a) zeta potential and (b) hydrodynamic diameter of unmodified TiO_2 (black circles) and lysine-functionalised TiO_2 synthesised at acidic (red circles), neutral (green circles) and alkaline (blue circles).

As before, the hydrodynamic diameter trends inversely with the overall magnitude of the zeta potential, illustrating the key role of electrostatic repulsion in the stability of colloidal nanoparticle suspensions. Additionally, the pH of the lysine adsorption has a significant effect on the morphology of the flocculated agglomerates. Transmission Electron Microscopy was performed (Figure 33) and the resulting images show a significant difference on the fractal dimension of the amino-acid functionalized products. When lysine is adsorbed from acidic (pH 1.5) solution, the agglomerates, while possessing a higher hydrodynamic diameter, retain the same open fractal structure as the as-prepared nanoparticles. This open structure is consistent with the reversibly agglomerated structure that results from random collision of the nanoparticles within a solution.

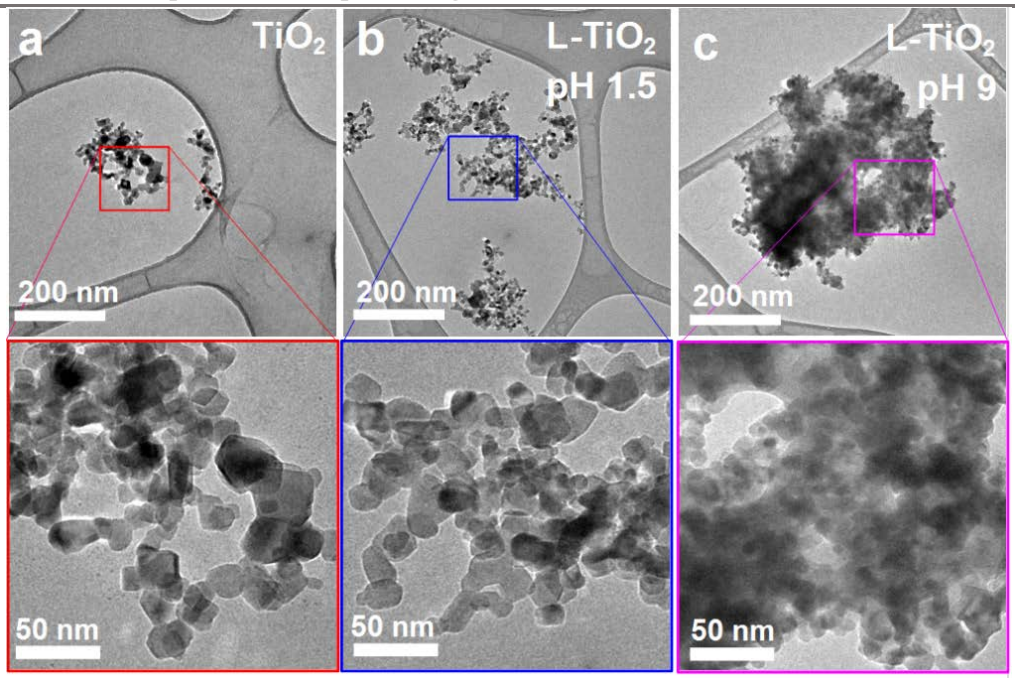

Figure 33. TEM micrographs showing the agglomerate size and morphology of (a) as-prepared and lysine-functionalized TiO_2 nanoparticles at (b) pH 1.5 and (c) 9.

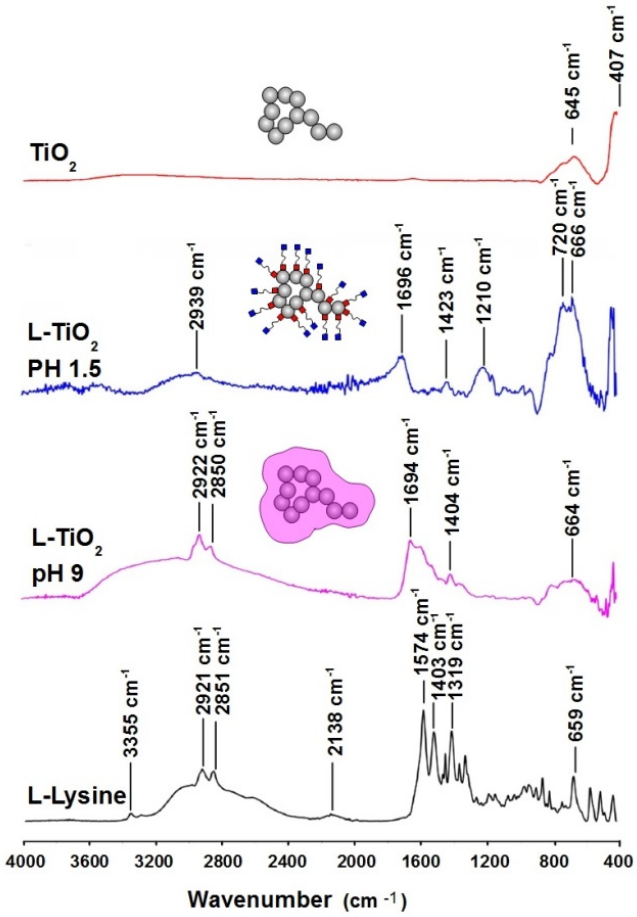

Figure 34. FTIR of bare TiO_2 (red), lysine-functionalized TiO_2 nanoparticles at pH 1.5 (blue), pH 9 (pink) and pure L-lysine powder (black).

However, when the lysine is adsorbed from an alkaline solution, the results are markedly different. Now, the agglomerates are not only larger but also show a denser structure. At higher magnification, it is possible to see an amorphous layer. This is consistent with the condensation of multiple layers of lysine molecules upon the nanoparticle surface that can be expected at pH 9 due to the zwitterionic form of the amino acid allowing for electrostatic attraction of neighbouring molecules. The increased agglomerate size and dense structure is indicative of the assembly of the nanoparticles into larger, microscale structures that is promoted by the adsorption of zwitterionic amino acids. In fact, lysine electrostatic attractions have been used by other researchers to form of relatively stable composites of 700 to 1200 nm[326]

This pH-dependant functionalisation/ coating is further supported by the FTIR results. The as-prepared TiO_2 (Figure 34, red line) spectrum was characterized by strong absorption bands below 850 cm^{-1}. These are attributed to the lattice vibrations of TiO_2[327], and confirm the high crystallinity of the flame-made samples. The spectrum of the acidic conjugated samples (Figure 34, blue line) was similar to that of the as-prepared TiO_2 showing few peaks matching the lysine spectrum (Figure 34, black line). This further supports the successful formation of an adsorbed lysine layer as indicated by the changes in zeta potential.

Conjugation in alkaline conditions (Figure 34, pink line) resulted in significantly higher match to the lysine spectrum (Figure 34, black line) with a similar broad hump between 3600-2000 cm^{-1} appearing. This is characteristic of solid lysine samples dried upon reactions in highly alkaline conditions (pH ~12)[328] and it is commonly attributed to the overlapping bands of NH^+ groups[329]. Here, this NH^+ surge is attributed to the formation of disordered, dendritic lysine mass terminating in protonated amino groups.

The sharp peaks at 2922 cm^{-1} and 2850 cm^{-1} are assigned to CH_2 bonds[328]. Their intensity increases rapidly with the mass of lysine molecules surrounding the nanoparticles.

The effect of pH is even more remarkable for the adsorption of L-glutamic acid onto TiO_2 (Table 10). Here, we see that at under alkaline conditions the zeta potential is unmodified (ca. -40mV), suggesting insignificant adsorption of the amino acid, while under acidic conditions the zeta potential shifts significantly towards +38.4mV. This is in keeping with the –COOH dominant adsorption hypothesis under acidic conditions. Due to glutamic acid possessing two –COOH groups, it is within reason that its adsorption can be drastically promoted by acidifying the reaction media. Furthermore, we note that theoretical modelling indicates that dicarboxylic acids may adsorb strongly via the bidentate bridging and chelating formations available to these molecules. [330] In such situations, the bidentate-adsorbed molecule may be expected to contribute even more strongly towards the positive shift in the zeta potential due to the single residual – NH_3^+ group being exposed.

Table 10. Evolution of zeta potential and hydrodynamic diameter between pure TiO_2 and lysine-functionalized TiO_2

	Bare TiO_2	**Glut-TiO_2 pH 1.5**	**Glut-TiO_2 pH 9**
Zeta Potential (mV)	-40.0	+38.4	-40.2

2.3 Activity of –NH_2 termination

Since subsequent attachment of proteins and DNA vectors are amine-reactive, it was necessary to directly gauge the reactivity of the amines on the functionalised nanoparticles. This was done by reaction with fluorescein isothiocyanate (FITC), a

fluorescent, primary amine-reactive dye, to create fluorescent-labelled nanoparticles with a characteristic FITC absorbance at ca. 470nm.

This experiment was performed on the lysine-TiO_2 previously synthesised from alkaline and acidic conditions. An as-prepared TiO_2 was subjected to the same FITC treatment as a control against the possibility of direct adsorption of FITC onto TiO_2. A higher concentration of FITC was detected for the acidic lysine functionalisation than the alkaline counterpart (Figure 35), suggesting greater availability of $–NH_3$ terminations and is consist with previous zeta potential measurements.

Following from this, further experiments were conducted to try and optimise the dye loading further as loading capacity is a crucial metric for performance as a nanocarrier. Since previous experiments used excess quantities of L-lysine that resulted in the formation of a large, encapsulating mass of organic matter around the nanoparticles, an attempt was made to decrease the concentration. Using theoretical models of the available binding site concentrations on TiO_2 surfaces, a concentration corresponding to a single monolayer of adsorbed L-lysine molecules was formulated and the experiments repeated for both acidic (pH 1.5) and alkaline (pH 9) lysine adsorption, followed by FITC labelling of free $–NH_2$. This was found to have a significant effect on the loading capacity of the carrier towards the dye (Figure 35, b), increasing by a factor of 10. Once again, the reaction pH had a significant effect, with a lower pH preferred. The final $–NH_2$ availability for the lower concentration was further studied across reaction time.

The measured FITC concentration was computed as a ratio over the theoretical number of surface Ti-binding sites to help visualise the functional molecule density (Figure 36). The theoretical Ti-sites were estimated from the surface density of Ti atoms using the average particle size, assuming a spherical geometry and (101) and (110)

surfaces planes for anatase and rutile respectively (see Materials and Methods for more information). This ratio was found to peak at 3 hours, after which a gradual decline was recorded. It is hypothesised that this peak represents the maximum adsorption of reactive L-lysine onto the TiO_2 surface before the organics begins to degrade due to the imperfect blockage of ambient light during the total reaction time.

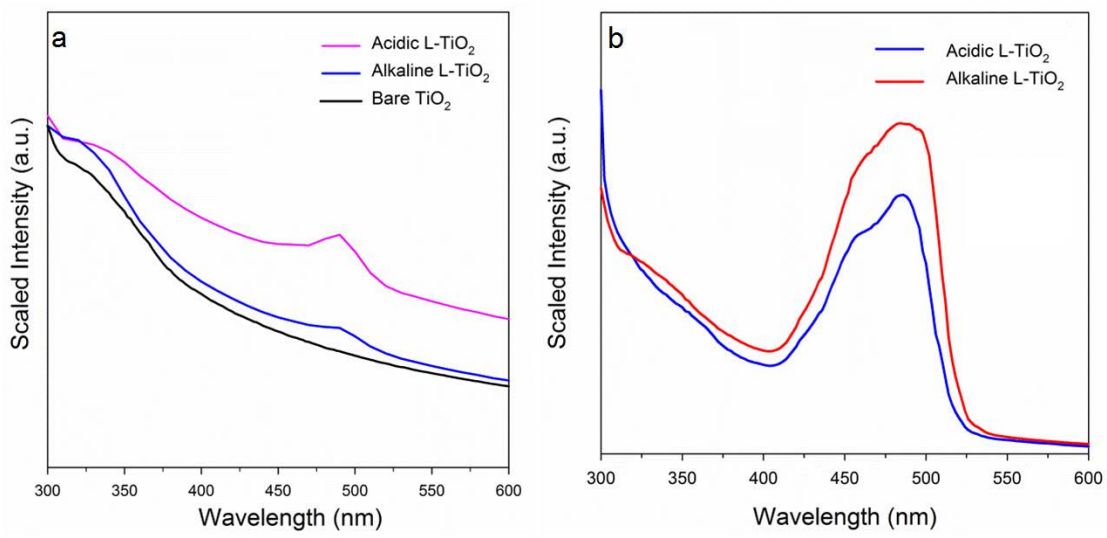

Figure 35. (a) Absorbance spectra of FITC conjugated onto bare TiO_2 (black), and lysine-TiO_2 prepared with excess L-lysine at pH 1.5 (pink) and pH 9 (blue). (b) Absorbance spectra of FITC conjugated onto lysine-TiO_2 prepared with low concentration of L-lysine at pH 1.5 (red) and pH 9 (blue)

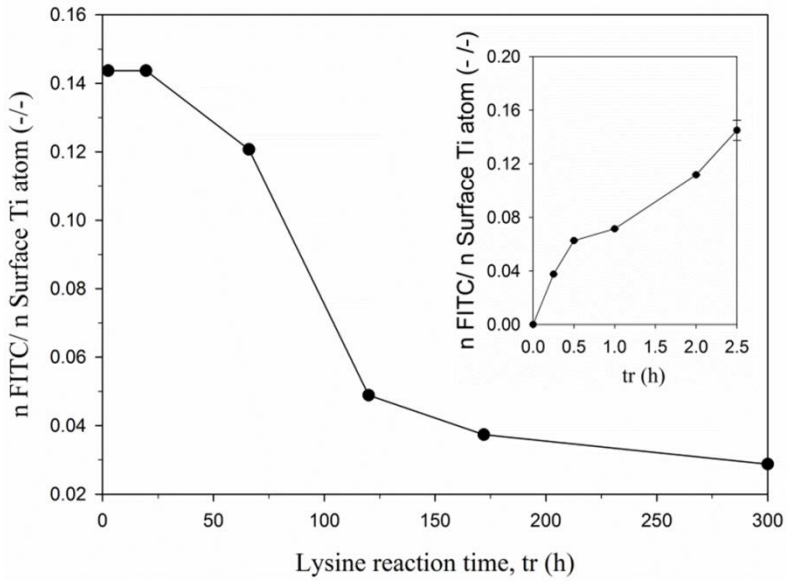

Figure 36. nFITC/ Surface Ti-binding site ratio computed for lysine-TiO_2 at low concentration pH 1.5 across a long term study.

2.4 Response of AA-functionalised TiO_2 nanoparticles towards UV light

Having established an optimal condition for the amino-functionalization of the TiO_2 nanoparticles, the photocatalytic response of the material was then determined. The lysine-coated samples were exposed for variable time intervals to UV light. In general, a decrease in the recorded hydrodynamic diameter (Figure 37 b) was recorded alongside a negative shift in the zeta potential (Figure 37 a) towards the original value for the bare TiO_2. Upon 20 s exposure, the DLS agglomerate size distribution (Figure 38) of the low concentration lysine-TiO_2 shifted from a large agglomerated distribution back to a unimodal that is similar to that of the as-prepared powders. In line with these results, their ζ-potential (Figure 37 a) decreased from ca. -12 mV of the acidic conjugated samples back to -35 ± 1 mV, close to that (-40 mV) of the as-prepared TiO_2. Analysis of the photo-response dynamics (Figure 37 b) indicated an asymptotic decrease in hydrodynamic diameter (d_H) within the first 30 s of UV exposure with d_H decreasing from 1100 nm of the 0.5 ML (t_r = 120h) acidic conjugated samples to ca. 400 nm. Both behaviours are consistent with the successive removal of lysine molecules from the nanoparticle surface.

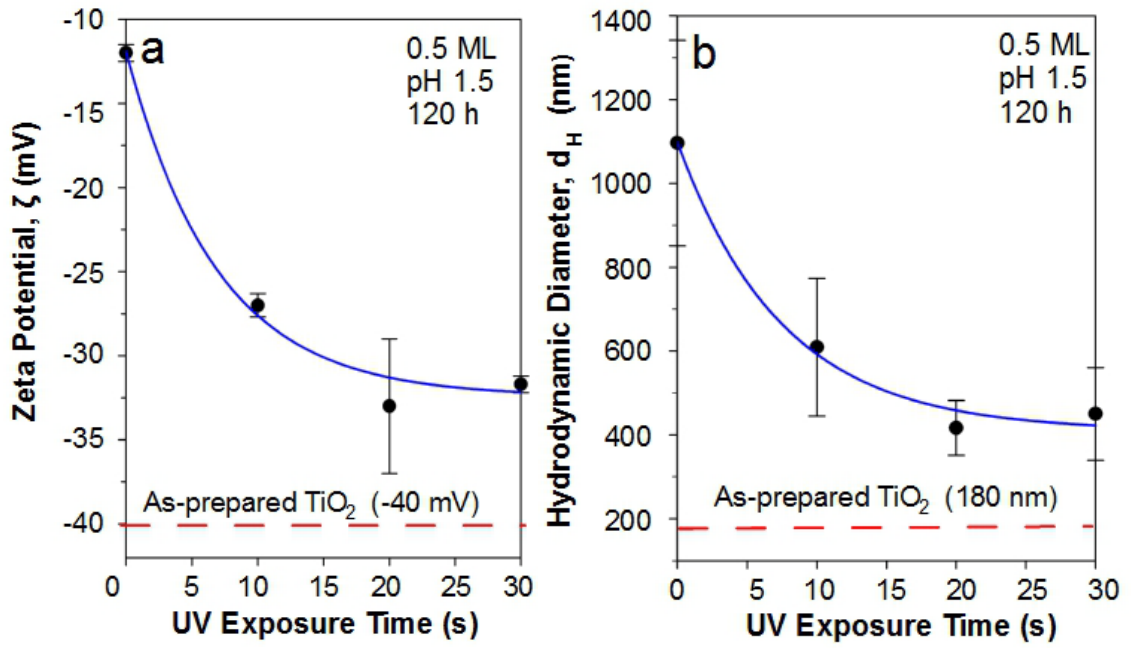

Figure 37. (a) Zeta potential and (b) hydrodynamic diameter of lys-TiO_2 after increasing exposure to UV-A light.

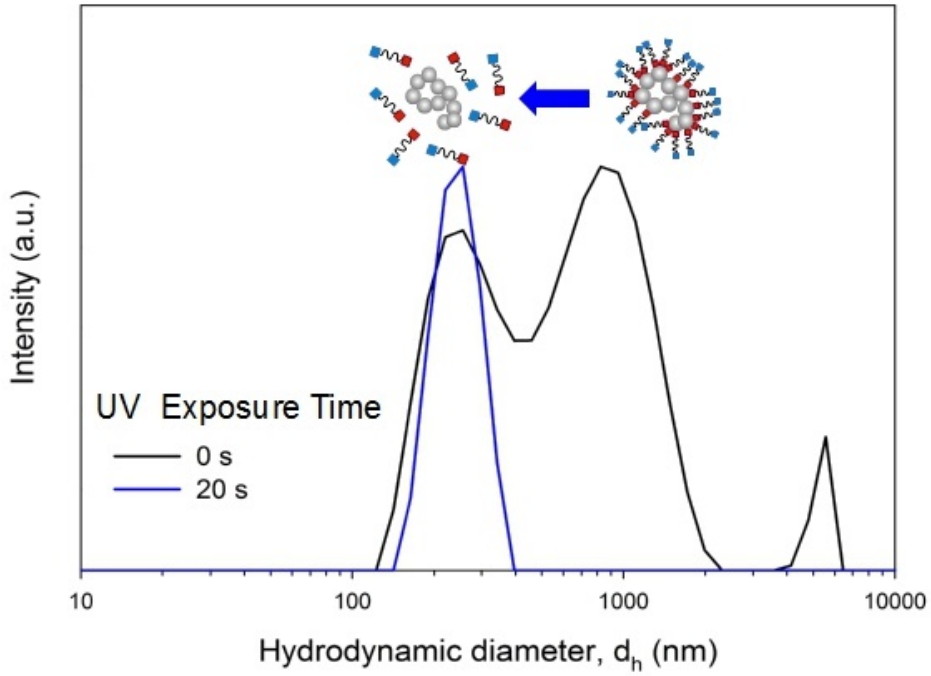

Figure 38. hydrodynamic diameter distribution of lys-TiO_2 before (black line) and after 30s (blue line) exposure to UV-A light.

Although promising, these results alone cannot confirm that the nanocarrier is responding to the applied UV light by releasing the surface-adsorbed molecules. Instead, it is possible that the molecules are simply being destroyed by photocatalytic redox events on the surface, thus returning the nanoparticle to its initial, unmodified properties. The decomposition of various amino acids solution by photocatalysis of TiO_2 is well-known.[218] Therefore, the lysine content liberated into solution after UV exposure was confirmed by using a Fluorescamine reaction on the solution after removal of the particles post-UV treatment in order to assess the release rate in greater detail. Fluorescamine reacts with primary amines to create a fluorescent adduct (Figure 39) that can be correlated to lysine concentration with appropriate calibration (see *Appendices*). In this way, an estimate on the free lysine concentration as a function of the UV exposure time was obtained.

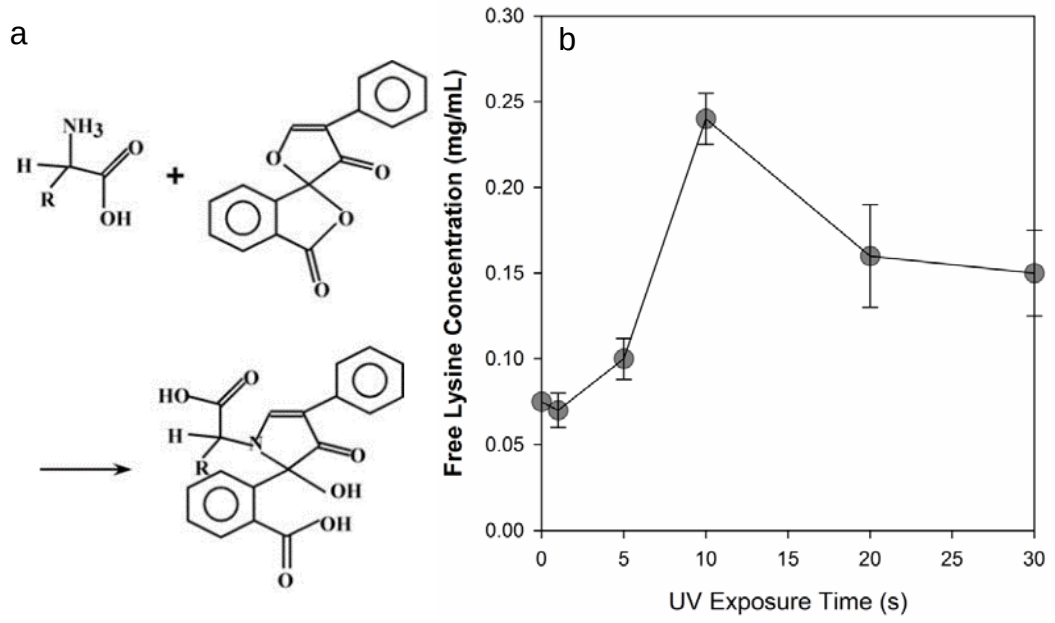

Figure 39. (a) Reaction between primary amine and fluorescamine producing a fluorescent adduct. (b) Fluorescamine assay of free lysine concentration in solution after exposure to UV light.

The result obtained is interesting as a peak was recorded at 10s rather than a sustained increase reaching a final asymptotic value as might be expected from a continuous activation. The two pathways that may be imagined are readsorption (unlikely, considering the consistent return of zeta potential and hydrodynamic diameter towards original values), or the loss of reactive -NH_2 via redox events. This may be attributed to the subsequent photocatalytic degradation of amino acids via redox events in accordance with known pathways[331] that may begin after this time. For example, it is been observed that photocatalysis of lysine on TiO_2 may cause selective cyclisation into pipecolinic acid[332] via the following reaction pathway (Figure 40).

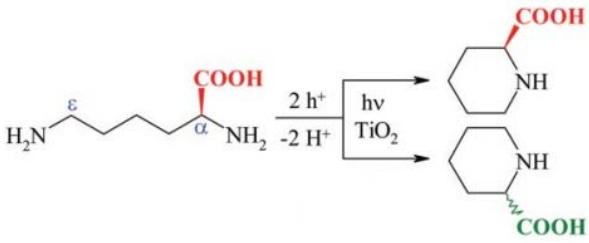

Figure 40. Photocatalytic cyclization of lysine into pipecolinic acid isomers. Adapted from [333]

To test this hypothesis, GC-MS was performed on the particle-free solutions. A strong match for L-lysine (Figure 41 a) was obtained, but evolution of pipecolinic acid was detected simultaneously (Figure 41 b), suggesting that photocatalysed conversion of lysine to its cyclisation compound[334] does occur in solution, in line with literature[335]. This result highlights the importance of controlling the UV exposure time in such a system as although the molecule release from the carrier surface scales with exposure time, there exists a critical point at which photocatalytic degradation appears to take over. In this particular case, photo-degradation of the functional molecule becomes dominant by ca. 10s.

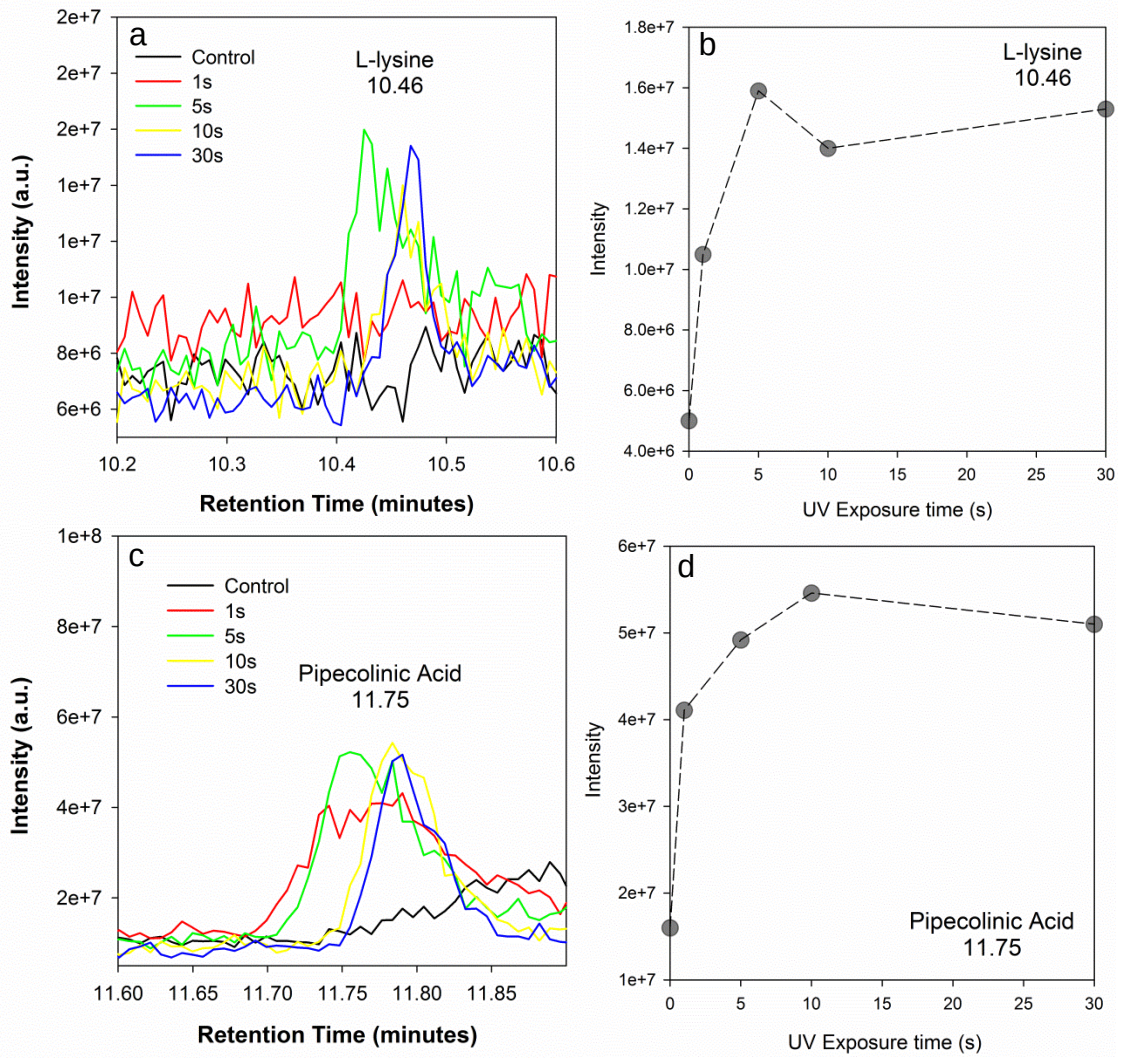

Figure 41. Mass spectrometry of particle-free solution after successive UV illumination showing (a,b) L-lysine and (c,d) pipecolinic acid, its radical cyclisation product.

For comparison, glutamic acid an analogous study was conducted on L-glutamic acid. Following the insights from L-lysine functionalization strategies, this was performed using calculated monolayer coverage of L-glutamic acid in acidic conditions at a nominal reaction time of 24 hours (the full optimisation over the reaction time parameter not being carried out for this molecule). This functionalised material was then exposed to successive UV and the particle-free solution assayed with fluorescamine as per previous experiments (Figure 42). A similar trend was observed for glutamate, consisting of a maximum concentration released at ca. 5s followed by a gradual

decrease. Mass spectrometry confirmed that glutamate's cyclisation product, pyroglutamic acid, was simultaneously formed (Figure 43), suggesting an analogous mechanism. However, it should be noted that in this case the quantitation of the mass spectra data does not fully agree with that obtained by the fluorescamine assay. While ca. 5s appears to be the peak time for glutamate release according to the fluorescamine assay, the mass spectra seem to indicate that 10s is preferable, as for the L-lysine release. It should be noted that the time point at 5s for the fluorescamine assay is highly variable and this may account for the oscillatory shape of the glutamic acid peak intensity recorded by mass spec at 5s (Fig. 43 c).

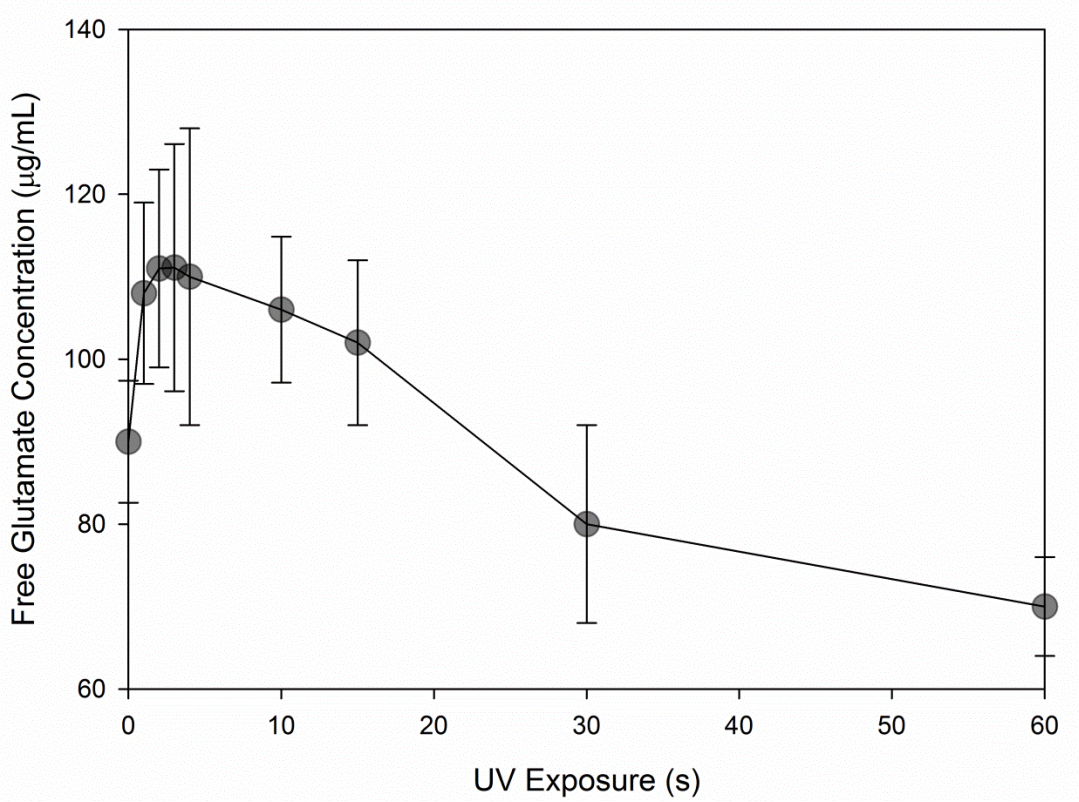

Figure 42. Fluorescamine assay of particle-free solution for glutamate-TiO_2 after exposure to UV.

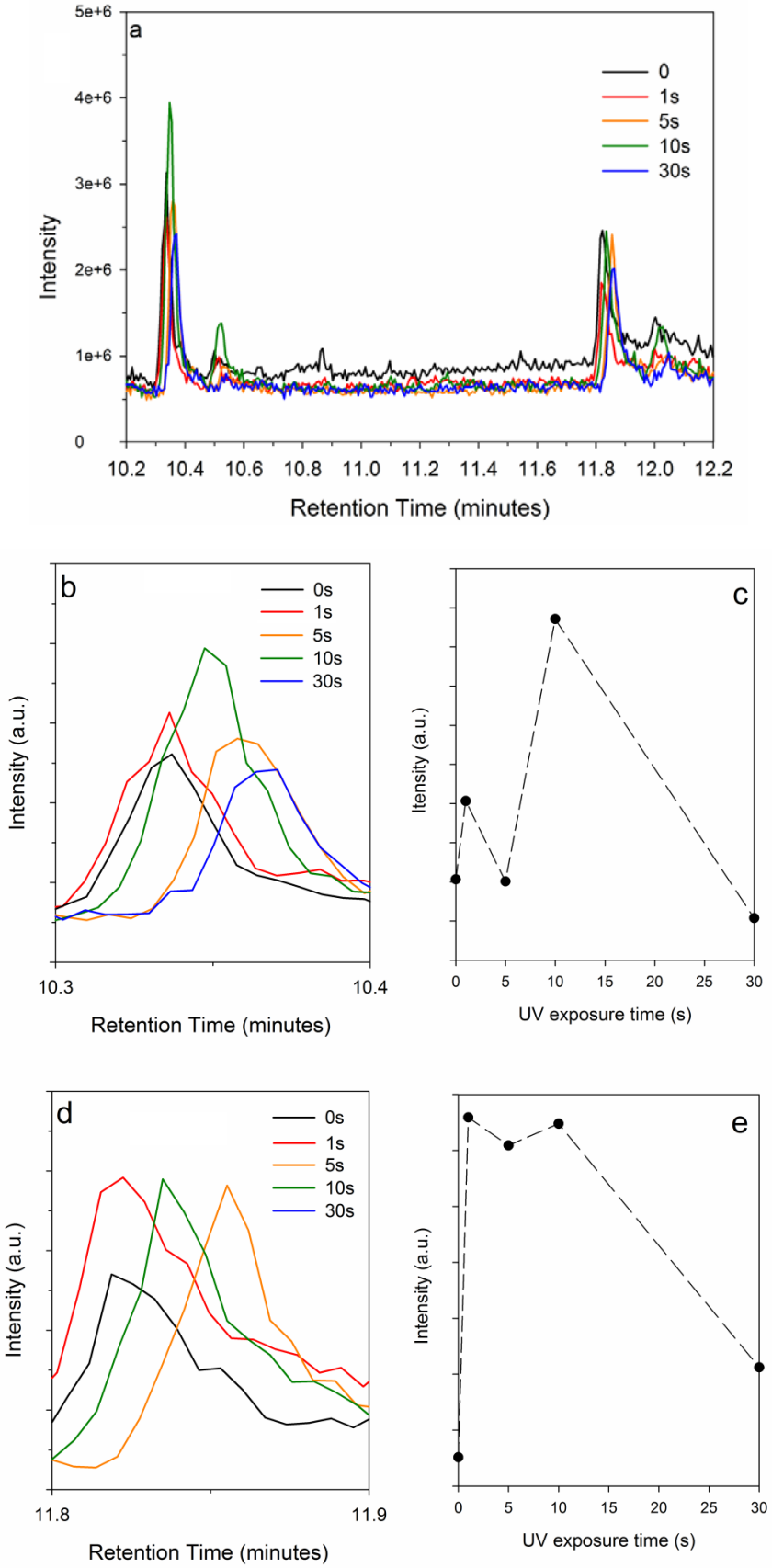

Figure 43. (a) Mass spectrometry results for particle-free solution after exposing glutamate-TiO_2 to UV light showing evolution of (b,c) free glutamate alongside (d,e) pyroglutamic acid.

2.5 Loading and release of model drugs

Next, the amine groups of the lysine-TiO_2 were conjugated with a model drug, the anti-inflammatory ketoprofen (Figure 44 a). This is a useful model as the attachment of ketoprofen to L-lysine can improve the uptake of the drug through the blood-brain-barrier (BBB). Ketoprofen being ordinarily hydrophilic cannot easily cross the BBB unless attached to a nanocarrier[336] or modified by amino acids to allow for transport across the large amino acid transporters[337]. Thereafter biodegradation of the lysine-ketoprofen link yields pharmacologically active ketoprofen.[337] Thus, the release of the full prodrug (Ketoprofen-Lysine) from a nanocarrier is of importance, and is currently not well-studied. It is not yet fully understood, for example, where the bond(s) will break in a system comprising ketoprofen-lysine-TiO_2 and thus whether the prodrug, the drug, or some partially photocatalytically degraded intermediate will be released, although this question is a crucial one.

Mass spectrometry was performed on the free solution to identify products present after progressive UV light exposure. and identified a strong match for ketoprofen (Figure 44 b). Although 10s was previously established as ideal for lysine release, it was found that the ketoprofen-lysine pro-drug concentration at 5s UV illumination after which point the signal decreased again (Figure 44 c),

It is of interest to note that the m/z values were a close match to ketoprofen (Figure 44 b) and no evidence of the ketoprofen-lysine pro-drug structure[35] was recorded. At the same time, no signatures corresponding with L-lysine (Figure 44 e) or the cyclization product pipecolinic acid (Figure 44 f) were recorded. Based on these data, it is proposed that UV-triggered release is causing a rupture of the ketoprofen-lysine bond (Figure 44 g). This result is significant as it implies that photocatalytic drug

release systems based on amino acid-functionalised TiO_2 cannot be used to successfully deliver amino acid-modified prodrugs as the electron-hole generation events cascade to cause detachment of the amino acid from the end-loaded drug molecule.

On the other hand, this result may also mean that highly specific molecules that cannot be afforded irreversible covalent modification may be successfully delivered as it appears that the bond between the payload molecule and the amino acid tether is detached during the light-activated release process. This is an important observation that has not been previously reported as far as the author is aware.

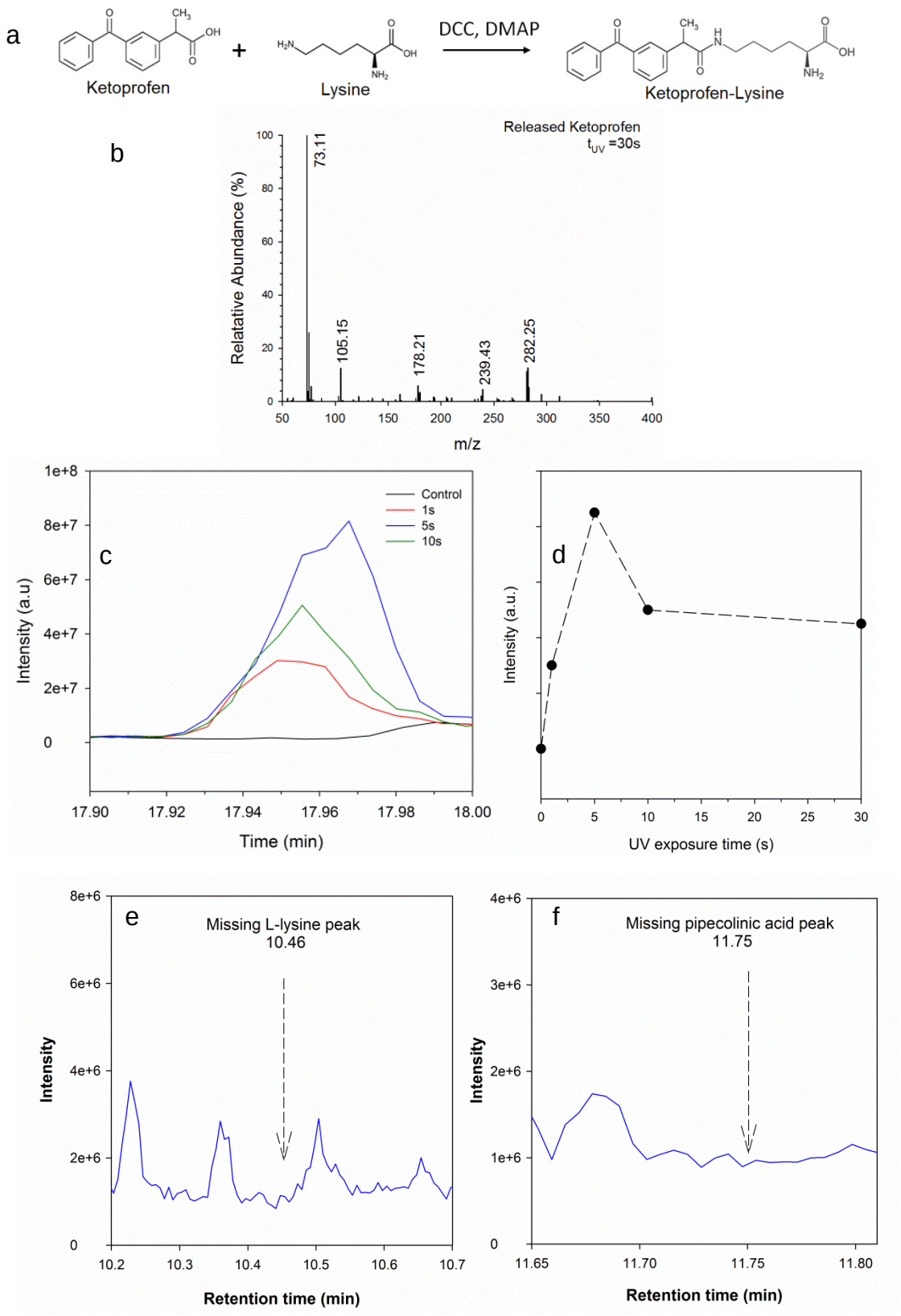

Figure 44. (a) Reaction pathway to synthesise ketoprofen-lysine prodrug.[337] (b, c,d) mass spectrometry results showing release of ketoprofen and absence of (e)L-lysine and (f) pipecolinic acid peaks.

Chapter Summary

In this chapter, biomedically important metal oxide nanoparticles SiO_2, TiO_2 and Fe_3O_4 were synthesised by flame-spray pyrolysis and their material properties characterised. An optimisation of Fe_3O_4 synthesis for magnetic properties and particle size was presented. A general strategy was devised for the functionalisation of these materials with amino acids L-lysine and L-glutamic acid. An optimisation strategy based on altering the reaction pH, amino acid concentration and reaction time was developed. The initial hypothesis that the reaction pH will have significant effects on the overall reactivity and flocculation dynamics of the nanocomposites was proven to be correct. In particular, it was discovered that: (i) acidic conditions result in greater extent of binding by –COOH groups, leaving greater content of $–NH_2$ terminations free for further reactions, (ii) amino acids can induce electrostatic flocculation and assembly of large, micro-scale aggregate when functionalisation is carried out in alkaline conditions, (iii) to limit flocculation and maximise available $–NH_2$, amino acid concentration and reaction time should be controlled.

The photocatalytic response of functionalised TiO_2 towards UV light was investigated, and a mechanism comprising simultaneous cleavage of the lysine-TiO_2 bonds and radical degradation of the functional molecule into its cyclisation compound Pipecolinic acid was proposed based on mass spectrometry and Fluorescamine assay results. An optimal time for the release of the amino acid before photocatalytic decomposition was identified at ca. 10s. Finally, a model drug Ketoprofen was successfully loaded and released by short term exposure of the composite to UV light. Despite the covalent attachment of the ketoprofen to the lysine molecule, forming a

lysine-ketoprofen prodrug, upon illumination by UV light, free ketoprofen alone was detected in the solution, suggesting that the photocatalytic action caused a cleavage of the bond between the amino acid and the loaded drug in this instance.

Overall, it was discovered that UV light could successfully and controllably trigger the release of a bound drug in a time range that is that significantly shorter than that reported in literature. To date, the majority of TiO_2 drug delivery systems do not make use of the photocatalytic effect and as a result still report a cumulative release that requires hours or even days to reach a maximum value.[67] The system developed here has an action time that is competitive with that reported by the few other photocatalytic TiO_2 drug release systems that currently exist. For example, by Shrestha et al. were able to release a model dye in "a few seconds" from an array of nanotubes, although they were unable to quantify the release and extend this to a useful drug. [16] Song et al. were able to release a bound enzyme, although over a significantly longer 600s.[31] As far as the author is aware, this is the first time that the decay in the detected level of the released compound has been reported alongside the evolution of redox decomposition products.

2.6 Materials and Methods

Flame synthesis of TiO_2 agglomerates

A flame spray pyrolysis (FSP) reactor was used for the synthesis of TiO_2 nanoparticles. The liquid precursor was prepared by diluting 0.5 mol/L of titanium(IV) isopropoxide (TTIP, Aldrich, purity > 97%) in xylene (Fluka, purity > 98.5%). The solution was supplied at a rate of 5 ml/min through the FSP nozzle and dispersed to a fine spray with 5 l min1 oxygen (pressure drop 6 bar) through the surrounding annulus. This spray was ignited by a supporting annular ring of premixed methane/oxygen flamelets (CH4 ¼ 1.2 L/min and O2 ¼ 2 L/min). Powder samples were collected with a vacuum pump (ICME Type M80B4) on water-cooled glass fibre filters (Sartorius glass microfiber FT-3-01124- 150, 160 mm diameter) placed at ca. 40 cm height above the burner. X-ray diffraction analysis was performed with a Bruker, D2 Phaser diffractometer operated at 30 kV, 10 mA at 2q (Cu Kα), range 10–80θ, step size 0.2θ and scan speed 2.3θ / min. The crystal size (d_{XRD}) was determined by Rietveld analysis with the structural parameters of rutile and anatase. The powder specific surface area (SSA) was measured by BET analysis using a Micromeritics Tristar II. BET equivalent diameter was calculated for spherical primary particles using the XRD weighted average densities of TiO_2 rutile and anatase. Transmission electron microscopy was conducted using a Hitachi H2100, operated at 125 kV.

Amino acid functionalisation

Functionalisation was carried out in aqueous solutions at pH 9, pH 7 and pH 1.5 prepared by adding HCl (Aldrich, purity > 37%) and NaOH (Aldrich, purity > 97%) to distilled water. The pH was measured using a pH probe (Oakton pH 700) at the start of

the reaction. The TiO2 powders were first calcined in a muffle furnace (CEMMS) for 4 h at 450 C to desorb physi- or chemisorbed H_2O. Then, 9 ml of 5.23 mmol/L TiO_2 nanoparticle suspensions were prepared by adding 3.76 mg of TiO_2 powder to the aqueous solutions and ultrasonicating (Eumax Ultrasonic Cleaner) for 5 min. A controlled amount of L-lysine (Aldrich, purity > 98%) was dissolved in the aqueous solutions and added to the particle suspensions. L-Lysine concentration was added with respect to the amount required (1 monolayer, ML) for the complete conjugation of the TiO_2 surface metal atoms.

The monolayer lysine concentration was estimated as follows: a maximal theoretical Ti–metal atom surface concentration of 12.43 atom nm2 was computed from the XRD composition and considering only the most thermodynamically stable surface planes of anatase (101) and rutile (110) and a spherical geometry of single diameter (d_{BET}). All surface Ti atoms were assumed to be in this active hydroxylated configuration for stoichiometry calculations. In line with previous studies,27,28 five possible binding configurations of L-lysine to these Ti–OH binding sites were considered: (a) physisorption through (the more reactive) 3-amine, and carboxylate binding via (b) hydrogen bonding, (c) ester binding, (d) chelating and (e) bridging states. Cases (a) to (d) lead to a 1 : 1 ratio between –OH groups and lysine molecules, while (e) results in a 2 : 1 ratio. Based on the 1 : 1 configuration, excess, stoichiometric and sub-stoichiometric amounts of L-lysine were added to each solution. First, 10 mg, 1.46 mg and 0.75 mg of L-lysine were dissolved into 1 ml of aqueous solution at the desired pH. This mixture was then added to the nanoparticle suspensions. The reaction proceeded at room temperature, with magnetic stirring at 600 rpm, and the effect of reaction time was investigated from 0 to 500 h. The functionalised nanoparticles were

collected from the reaction medium via centrifugation at 4000 rpm for 40 min. The particles were washed once in water and re-suspended in distilled water.

A Zetasizer Nano S (Malvern) was used to measure change in zeta (z)-potential and hydrodynamic diameter (d_H) between the as-prepared and lysine-conjugated nanoparticles. Transmission electron microscopy (TEM) (Hitachi 2100, operated at 125 kV) was used to determine the formation of a polylysine matrix. ATR-FTIR (Bruker Alpha) was used to determine the resulting bonding type.

Functional molecule loading and release

The prepared TiO_2 particle–lysine solutions were ultrasonicated in a bath sonicator (Eumax UD100SH-3LN, 100 W) for an additional 3 min to break-up potential soft agglomerates. Then, 10 ml of 1 mmol/L fluorescein isothiocyanate I (Sigma, purity > 90%) diluted in a water/ethanol solution (e.g. 1 : 9 volume ratio) was added to the TiO_2 particle–lysine solutions to create dye-labelled nanostructures. To form ketoprofen–lysine–TiO_2 structures, 10 ml aliquots of lysine–TiO_2 were first centrifuged at 4000 rpm for 50 minutes to remove supernatant and freeze dried for 2 h. Ketoprofen (5 mg) (Sigma, purity > 98%), and 4- (dimethylamino)pyridine (0.3 mg) (Sigma, purity > 99%) were dissolved in dry dichloromethane (30 ml) (Sigma, purity > 99.8%) and ethanol (20 ml) (Sigma, > 99.8%) before adding them to dried lysine–TiO2 particles, followed by 10 min of ultrasonication to form a suspension before the addition of Ncyclohexyl-N0 -(2-morpholinoethyl)carbodiimide-metho-p-toluenesulphonate (4.6 mg) (Sigma, > 99%). Loading of both FITC and ketoprofen was performed at room temperature for 48 h with stirring at 300 rpm, after which the samples were centrifuged again at 4000 rpm for 50 min to separate the product. The collected FITC and ketoprofen-terminated nanocomposites were suspended in water by ultrasonication for an additional 3 min.

These solutions were analysed by z-potential (Malvern Zetasizer Nano S) and UV-vis absorption measurements (Tecan M200Pro) to quantify the degree of loading and surface composition. To photocleave the ligand, the suspended product was exposed to UV light of 365 nm and 100 W (Spectroline Model SB700P/FA). The eluent was separated by centrifugation at 4000 rpm for 50 min. The effect of exposure time was investigated by dynamic light scattering and z-potential for each sample (Malvern Zetasizer Nano S). Primary amine fluorescamine assays were performed on the eluent by adding 100 mL of 1 mg/mL fluorescamine in DMSO to 300 mL of sample solution with fluorescence emission recorded at 470 nm (Tecan M200Pro).

GC-MS was used to identify released lysine and ketoprofen. Samples were injected (0.2–1.0 ml injection volume) via an autosampler onto a Rtx-5MS fused-silica capillary column (Restek, Bellefonte, PA, USA; 30 m 0.25 mm id) coated with a 5% phenyl–95% dimethylpolysiloxane (0.25 mm film thickness), which was eluted with He (inlet pressure 14.5 psi) directly into the ion source of a Thermo Polaris Q GC/MS (injection port 220 °C; interface 250 °C; source 250°C). The column was temperature programmed from 80 °C (hold 1 min) to 300 C at 10 °C /min. The mass spectrometer was operated in the electron impact ionisation (EI) mode with ionisation energy of 70 eV and scanned from m/z 50 to m/z 400.

CHAPTER THREE

Amino acid-assisted self-assembly of anisotropic iron oxide nanostructures

Published with modifications:

Zhang, T., P. Costigan, et al. (2016). "Disposable micro stir bars by photodegradable organic encapsulation of hematite–magnetite nanoparticles." RSC Advances **6**(40): 33843-33850.

Chapter Overview

In the previous chapter, the flocculation of nanoparticles by the electrostatic attractions of surface-adsorbed amino acids was discussed as a negative attribute towards delivery of amine-active moieties such as the anti-inflammatory ketoprofen. In this chapter, the electrostatic interaction will be explored in more detail and will be exploited to produce stable self-assembled structures of iron oxide. A method using an applied external magnetic field to create anisotropic, needle-like structures will be presented. The governing parameters of magnetic field strength, magnetisation of the nanoparticle, nanoparticle concentration and solution pH will be discussed. A highly novel rotating behaviour under a dynamic magnetic field is presented and described. Finally, the usefulness of these structures towards improving local mixing on the microscale and overcoming the challenging diffusion-limited regime at such size scales, is demonstrated. A schematic of the overall materials synthesis and performance testing process is given in Figure 45.

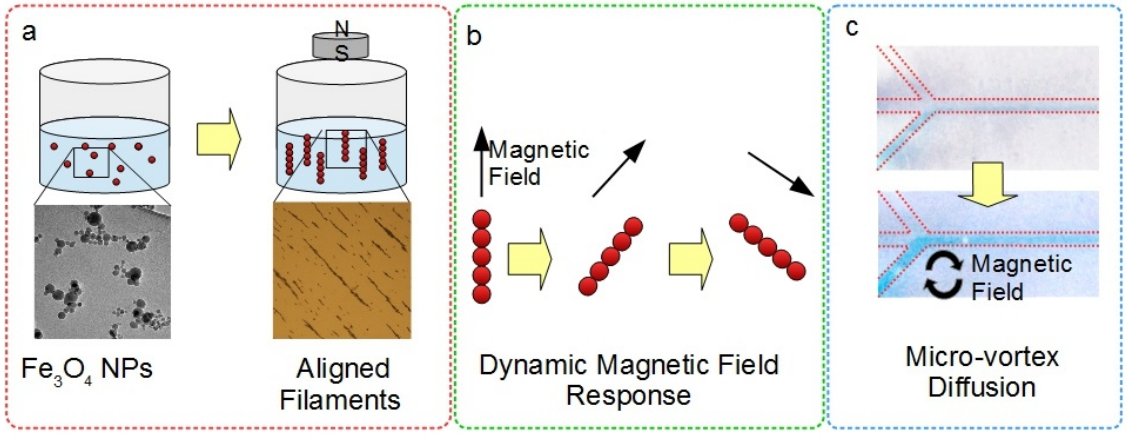

Figure 45. Chapter four overview.(a) Assembly of magnetic filaments, (b) dynamic response of filaments under rotating magnetic field, (c) micro-vortex-enhanced diffusion under a rotating magnetic field.

3.1 Lysine-assisted assembly of Isotropic structures

The flame-made iron oxide nanoparticles synthesized at a [Fe]/O_2 0.9 mmol/L were functionalised with lysine with an aim towards promoting the flocculation observed and avoided in the previous chapter. At a pH where both the iron oxide surface is negatively charged (pH> 7[338]) and the lysine is expressing amphoteric character (2.14 < pH < 12.48), neighbouring iron oxide nanoparticles should experience increased flocculation. This is in line with the results obtained for the previous chapter whereby TiO_2 agglomeration was drastically increased at pH 9 compared with pH 2.

First, a similar experiment was performed on iron oxide NPs at pH 4.6, 7.4 and 8.8 in the absence of any externally applied magnetic fields. It was found that the resulting structures had an overall larger mean agglomerate size and a different morphology compared with the bare nanoparticles. The as-prepared flame-made iron oxides had an open fractal-like morphology, while the encapsulated agglomerates had a dense, close-packed structure (Figure 46). The apparent agglomerate size increased with reaction pH. In alkaline conditions, the formation of a thick encapsulating layer of lysine residues observed and agglomerates reached > 10μm in diameter. These results resembles that reported by other authors for polylysine-coated magnetic nanoparticles.[43]The growth of these structures was largely isotropic, with the mean aspect ratio recorded at 1.8. This implies that, in the absence of a magnetic field, the growth of these agglomerated structures was undirectional and governed primarily by random collisions in random directions.

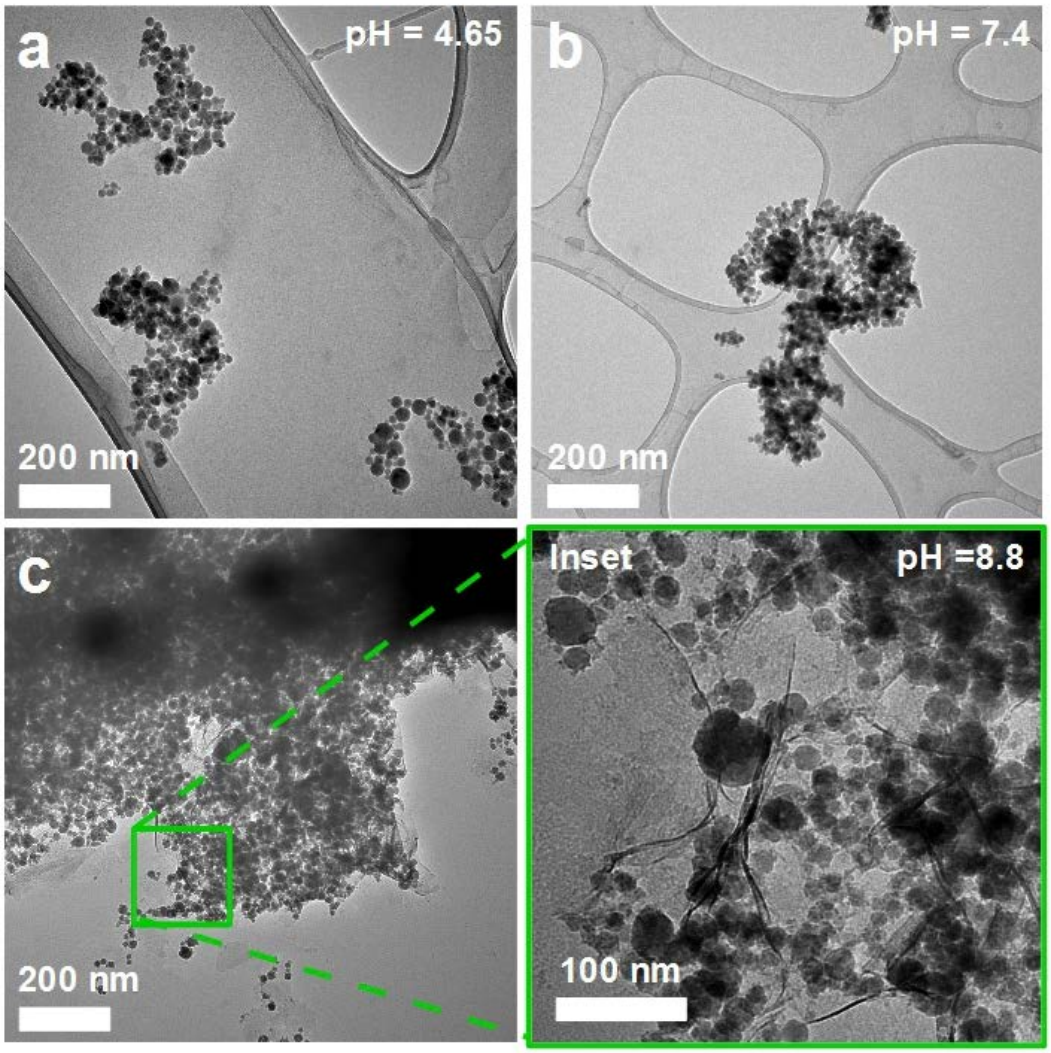

Figure 46. (a) SEM and (b) TEM images of flame-made magnetite ([Fe]/O_2 = 0.9 mmol/L) encapsulated in polylysine (PLL) at pH 8. 8 showing a nanorough surface morphology.

3.2 Magnetic-field assisted assembly of anisotropic structures

Next, an external magnetic field was applied perpendicular to the stirring plane and in opposition to gravity (see *Materials and Methods)* to promote anisotropic growth. Optical microscopy was used to determine the resulting structure. It was found that performing the amino acid functionalisation reaction under an applied magnetic field resulted in elongated structures of higher aspect ratios (Figure 47). These generally had a needle-like morphology with tapered ends that is similar to

that reported by Bharti et al. [169]. The main reaction parameters of interest were: the strength of the magnetic field, the reaction pH, and the magnetic properties of the nanoparticles. The distance of the permanent magnet source and thus the strength of the applied magnetic field was found to have a strong effect on the resulting stir bar morphology.. While the micro-bar's width was not affected by the magnet distance, the average stir bar length increased drastically from 15 to 100 μm with decreasing magnet distance from at 10 to 2.5 cm.

It is hypothesised that the primary driving force for the formation of these structures is the application of the magnetic field. The subsequent stability of this fibre-like structure is provided by two components: the amino acid residue/ encapsulation and the small remanence of magnetic field inside of the structure, both of which may have the effect of holding the chain of particles together.

It was also noted that the fibre-like material had a tendency to further grow in length when under a magnetic field applied by a rare earth magnet. Care was taken to ensure that the rare earth magnet type, size and distance was kept equal. However, the growth of these fibres in situ should not be discounted.

When compared against with the commercial magnetite nanoparticles, an important difference is observed. The commercial magnetite nanoparticles (Figure 47 g) resultedin the formation of significantly longer structures compared with the flame-made nanoparticles (Figure 47 e). However, from this result alone, it cannot be surmised whether this result is due to a difference in the particle size and shape, the magnetic character, or the difference in the amino acid adsorptions.

That author wishes to acknowledge that Figure 47 f, h are reproduced from the undergraduate thesis of Paul Costigan (supervised by the author).

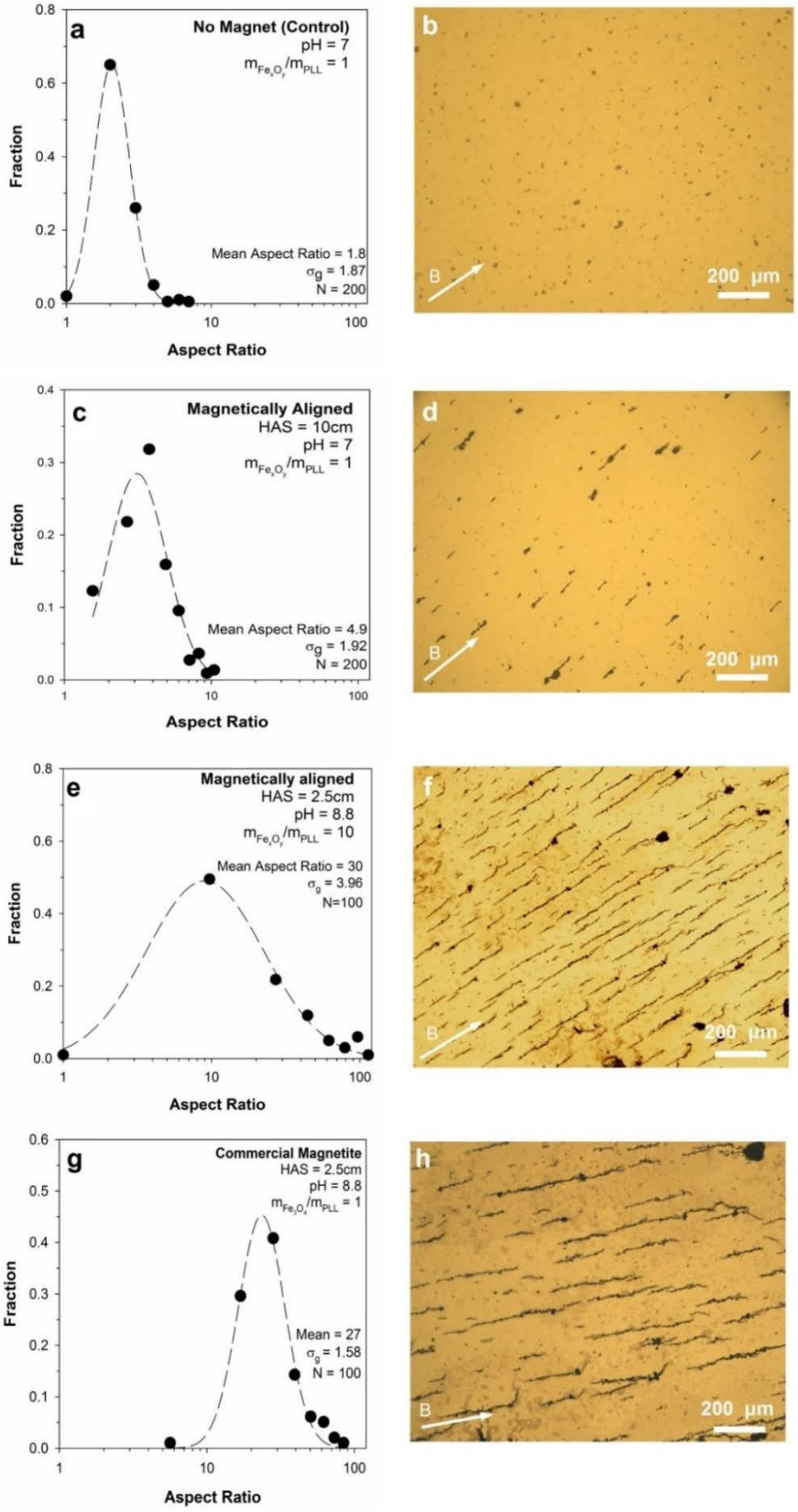

Figure 47. Aspect ratio distributions of encapsulated PLL-Fe_xO_y as computed from optical microscopy (inset) and scanning electron micrographs (beside) for flame-made iron oxide and commercial magnetite

nanoparticles: (a) control with no magnetic alignment and (c,e) magnetically aligned flame-made nanoparticles ([Fe]/O_2 = 0.3 mmol/L), and (g) commercial Fe_3O_4 nanoparticles.

3.3 Modelling magnetic interactions

To understand these observations in more detail, a model was constructed to describe the anisotropic assembly process. In addition to the field strength and magnetic properties of the material, an additional important parameter driving self-assembly is the initial agglomerate size of the iron oxide nanoparticles. Although the samples with a [Fe]/O_2 of 0.3 mmol/L had a lower magnetic saturation, they also had a significantly larger agglomerate size (305 nm) than the samples with a [Fe]/O_2 of 0.9 mmol/L (153 nm). Assuming that self-assembly proceeds predominantly by end-on-end addition in the direction of the applied magnetic field, the final aspect is proportional the number of collisions between agglomerates along the direction of the applied field that result in successful adhesion. The agglomerate size has a two-fold effect on the collision frequency. Equation 6 describes the collision frequency Z_{AB} of agglomerate A, approximated as a sphere of radius r_A, and the end of one rod-shaped structure with a half thickness/radius $r_B = r_A$. The Z_{AB} is a function of the agglomerate radius and mean velocity of the colliding sphere v:

$$Z_{AB} = N_A N_B (r_A + r_B)^2 \pi v \qquad \text{(Equation 6)}$$

Where Z_{AB} = collision frequency; v = velocity; N_A = number of colliding agglomerates with the bars; N_B = number of colliding bars with the agglomerate; $r_A = r_B$ = agglomerate radius.

The velocity v can then be estimated by modelling the colliding agglomerate as a superparamagnetic sphere within a uniform magnetic field.[44] Only motion along the applied perpendicular magnetic field lines is considered

here. This is equivalent to neglecting the influence of the magnet nanomaterials on each other and assuming anisotropic growth occurs only along the direction of the dominant external field. It should be noted that in reality there will be attractive/repulsive forces between two neighbouring magnetic nanoparticles, although the magnitude of these forces should be small compared with that supplied by the external field.

Furthermore, Agglomerate motion by diffusion is also neglected as the Péclet number is ca. 22 for this system (see *Appendices* for details of the calculation). This indicates that ballistic motion driven along the magnetic field lines is the dominant over the randomly oriented diffusion path.[45]

With these assumptions, the velocity term component of the collision frequency (Equation 6) may be expressed by considering the balance of the accelerating magnetic force and the decelerating drag force acting on an agglomerate (supplementary equations S1 - S15). Thus, the collision frequency is given by:

$$Z_{AB} = 4N_A N_B r^2 \pi \left(C e^{-\frac{18\eta}{4r^2}t} + \frac{3\chi\mu m^2}{8\pi^2 x^5 \rho} \right) \qquad \text{(Equation 7)}$$

With η = liquid dynamic viscosity, t = time elapsed, χ = magnetic susceptibility of particle, μ = permittivity of liquid, x = distance from magnet, and ρ = density of the agglomerate.

The exponential term can be neglected as the square dependency from the radius of agglomerates considered here (10^{-7} to 10^{-6} m) results in values approaching zero. As a result, the collision frequency is dependent on the second power of the agglomerate diameter and directly proportional to their magnetic susceptibility**.** Figure 48 shows the plot of the normalized collision frequency

($\frac{z_{AB}}{N_A N_B}$) as a function of both agglomerate radius and magnetic susceptibility at normalized coordinates (t = 1 s, x = 1 cm). The results of this model suggest the critical impact of the agglomerate size when the magnetic susceptibility of the material is of similar magnitude, such as is the case for flame-made iron oxide nanoparticles. This effect may account for the higher aspect ratio of the sample with the higher initial agglomerate size (Figure 47 g) compared with the sample of lower agglomerate size (Figure 47e).

The results also show the effect of magnetization of the starting nanoparticle material on the resulting microbar monodispersity. In all cases, the assembled microstructures possessed a greater geometric standard deviation compared with the initial nanomaterial, reflecting inhomogeneity inherent in the assembly procedure. However, the dispersity was lowest when the magnetisation was higher, such as for the commercial magnetite particles (σ_g = 1.58) (Figure 47 g). The length of individual microbars relates directly to the size of its eddy when in rotation. Therefore, the geometric standard deviation of bars observed here will correlate to the dispersity in the size and speed of eddies during mixing. In turbulence, a wide distribution in eddy size and speed is typically observed. The wide distribution observed particularly for the flame-made sample (σ_g =3.96) (Figure 47 e) may render the material particularly suitable for turbulent mixing applications.

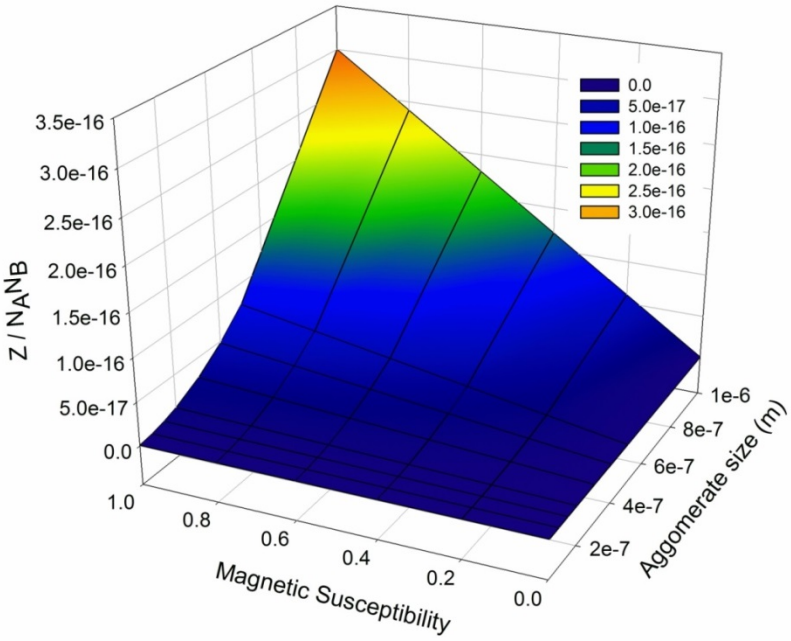

Figure 48. Modelling interaction agglomerate size and magnetic susceptibility on the collision frequency.

3.4 Motion of anisotropic structures under an applied magnetic field

The filament-like materials previously synthesised showed an interesting dynamic response towards any applied magnetic fields. Firstly, when a field is applied to a sample in wet suspension, the filaments arrange themselves to a highly uniform orientation that is parallel to the field direction (Figure 50 b). Additionally, there is net motion towards along the field gradient. When the field is rotated, these structures will attempt to follow the field, resulting in two types of motion: (a) rotation about the filament's centre of mass, and (b) orbital motion around the centre of rotation of the magnetic field. This is in line with previous reports on similar structures.[15] In the first case, micro-scale vortices were generated resulting in turbulent mixing.

Notably, no in-situ flocculation of the micro bars into larger structures was observed, highlighting their stability in suspensions. This may be attributable to the stabilising effect of the surface charge of the lysine-coated iron oxides in water. The

zeta potential was measured to be +13.4 mV for the lysine-functionalised filament structures, in line with previous observations. Flocculation of magnetic structures in aqueous solutions is usually driven by interaction of induced magnetic fields between neighbouring particles in addition to the usual van der Waals forces that are in play. This is counterbalanced by the electrostatic repulsion induced by the positively charged lysine coatings that exists in protonated form in water ($NH_3^+/COO^-/NH_3^+$). In this case, the electrostatic repulsion is strong enough to overcome the attractive forces.

This free, non-associating rotation is contrary to the 'bundling' behaviour reported by Bharti et al.[166] who observed that the flexible filaments initially aligned themselves within the stationary parallel magnetic field, but formed spherical bundles upon rotation that remained after the field was switched off and could not be reversed to their original, filament form. The improvement observed here is directly attributed to the difference choice of the functional molecule coating. Bharti et al. used lipids as the stabilising coating. Fatty acids adsorb to iron oxide surfaces via the –COOH group creating a lipid coating and leaving an exposed neutrally charged hydrocarbon chain on the outside of the nanoparticle. This lipid coating promotes strong van der Waals interactions. Here, the presence of charged functional groups exposed on the outside of the structure appears to have a crucial effect.

Video footage has been included with this dissertation that demonstrates the response of both a long filament-like structure (V1) and a random, agglomerated structure (V2) towards a rotating magnetic field. Figure 50 is a schematic of the three basic movement types observed.

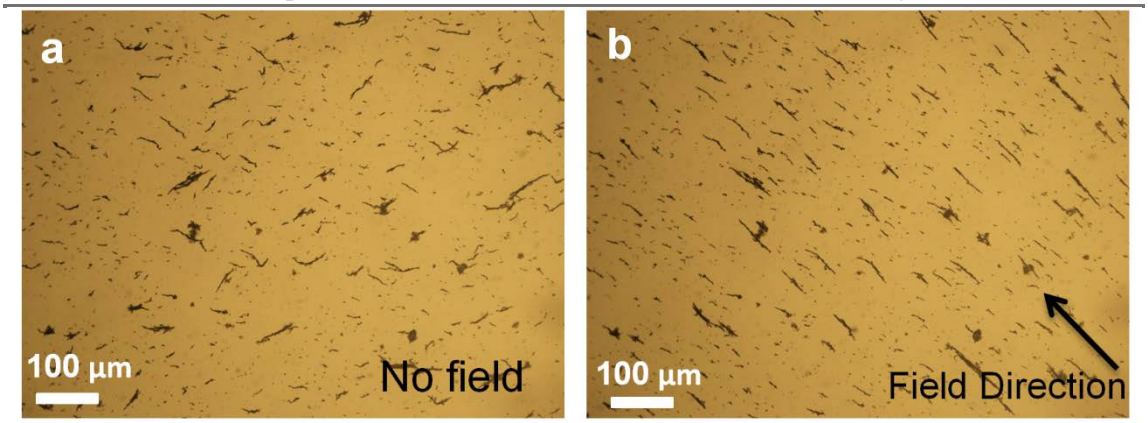

Figure 49. Magnetically assembled filaments (b) under the influence of a magnetic field and (a) after field removal.

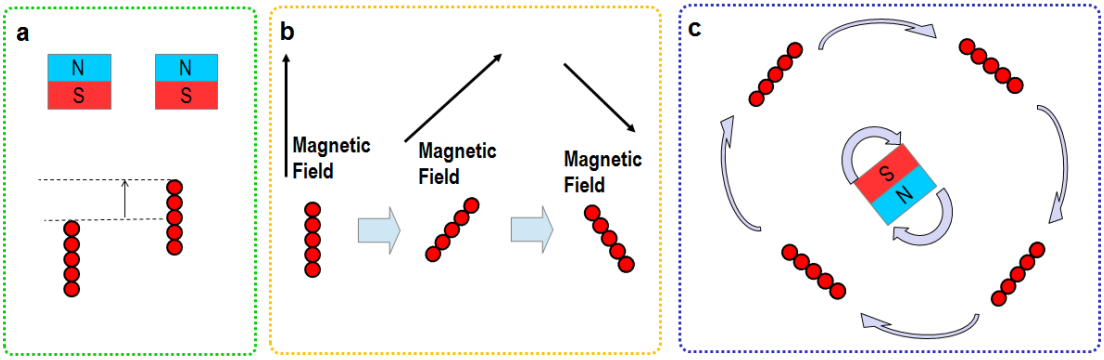

Figure 50. Schematic representation of magnetic filaments undergoing (a) translational, (b) rotational and (c) orbital motion under applied magnetic fields.

3.5 Using vortexing motion to improve microscale mixing

Due to the vortexing behaviours observed by the rotating filaments, it was hypothesised that such a movement may aid in improving mixing/ dispersion in small voumes. Inducing adequate mixing at the nano-to-microscale is a signicant challenge. Such size scales are generally in the laminar flow regime and resulting mass transport is typically diffusion-limited. Additionally, nanostructures may experience a local viscosity that is higer than the bulk counterpart.[339] This was investigated by introducing a dilute suspension of the magnetic filments into a standard PDMS chip. It was found that the use of a magnet is crucial to direct the filaments during injection into the chip to avoid blockage of the microchannel

and to position the filaments at the mixing point. The microbars rotated at 1500rpm with mininal horizontal displacement when positioned at the centre of the field of rotation. When applied within a dual stream system of water flowing beside trypan blue dye, the rotating magnetic filaments improved the mixing performance to a slight degree. An improved steady state diffusion profile across the width of the microchannel (Figure 51 b) compared with the low diffusion observed without (Figure 51 a).

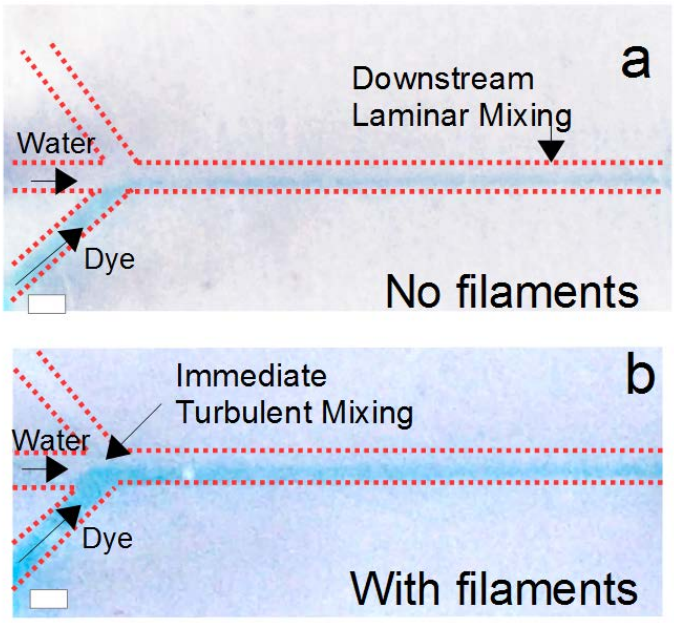

Figure 51. Flow of dye and water streams through a multichannel microfluidic chip (a) without and (b) with vortexing from magnetic filaments.

Chapter Summary

In this chapter, lysine-assisted flocculation under a directing magnetic field was used to assemble anisotropic microstructures of iron oxide nanoparticles, proving the initial hypothesis that pH-controlled electrostatic interactions between amino acid-functionalised nanoparticles can be exploited for self-assembly. The dynamics for this assembly were examined. It was found that the process may be modelled as dependant on the collision frequency. In this system, collision is influenced by the agglomerate size and the magnetic properties of the nanoparticles.

These filament-like structures exhibited several interesting responses towards an applied dynamic field, including translational, orbital and rotational motion. The rotation motion was used to create microscale vortexing that may induce improved mixing on the microscale, as hypothesised. However, it is not yet clear from the experiments presented in this chapter whether this vortex motion may in fact improve drug delivery rates.

The amino acid-coated iron oxide filaments presented in this chapter had a significant advantage over existing structures reported in literature to date. Most significantly, no irreversible ‘bundling’ (transition from filament to spheroid structure) upon rotating of the filaments was observed, neither was there any significant associative tendency between neighbouring filaments. This is an important advancement in the state of the art as this allows for the continuous rotation of the filament structures. This may be applied for the improvement of mixing rates on the microscale through microvortex action.

3.6 Materials and Methods

Flame spray pyrolysis

Iron oxide nanoparticles were synthesized using a flame spray pyrolysis (FSP) reactor (Appendices, Figure A4) as previously reported. The liquid organometallic precursor containing of Fe-ions (0.5–0.6 mol L^{-1}) was prepared by mixing iron naphthenate (Strem chemicals, 80% in mineral spirits) in xylene (Fluka, purity > 98.5%). The solution was supplied through the FSP nozzle (at a rate of 3–5 mL min^{-1}) and dispersed with oxygen at (2–9 L min^{-1}) with a pressure drop of 5 bar. The resulting fine spray was ignited by an annular pre-mixed methane/oxygen pilot flame (CH_4 = 1.2 L min^{-1}, O_2 = 2 L min^{-1}). Powder samples were collected with a vacuum pump (ICME Type M80B4) on water-cooled glass fibre filters (Sartorius glass microfiber FT-3-01124-150, 160 mm diameter) placed at 40 cm height above the burner. The resulting iron oxide nano powders were used without further purification.

Functionalisation by lysine

The magnetic micro-bars were synthesized by encapsulating the FSP-made iron oxide nanoparticles in lysine in an aqueous buffer solution. The buffer composition and pH, and iron oxide/coating material mass ratios were altered. In all cases, 2 mg of iron oxide powder was added to 10 mL of deionized water/pH 4.65 acetate buffer (Sigma-Aldrich)/pH 7.4 phosphate buffered saline/pH 8.85 sodium borate buffer and mixed with appropriate mass of L-lysine (Sigma-Aldrich) according to the desired mass ratio formulation (0.2 mg, 2 mg and 20 mg). The resulting suspension was sonicated for 10 minutes, then wrapped in foil and placed on a stirring plate at 1500 rpm for 24 h, directly beneath a strong rare earth magnet (N35, cylindrical, 2.54cm x 2.54cm, ca. 5500 Gauss) supplying perpendicular vertical alignment field. The distance between the

top of the stirring plate and the bottom of the perpendicular magnet (HAS) was set according to experimental conditions.

Characterisation

X-ray diffraction analysis was performed with a Bruker D2 Phaser diffractometer operated at 30 kV, 10 mA at 2θ (Cu Kα) = 10–80°, step = 0.02° and scan speed 2.3° min^{-1}. The crystal size (d_{XRD}) was determined by Rietveld analysis with the structural parameters of identified iron oxide phases. The iron oxide powder specific surface area (SSA) was measured by BET analysis using a Micrometritics Tristar II after *ca.* 16 hours degassing under vacuum at 120 °C. The BET equivalent diameter was calculated assuming primary particles and using the weighted average densities of iron oxide phases identified in the XRD analysis. The resulting micro-structures were imaged using optical microscope (Nikon Eclipse E200; TV lens 0.55× DS). Count distributions of mean bar length, width and aspect ratio were produced by measuring 200 bars for each sample using Image J software. Transmission electron microscopy was performed using Hitachi 7100 at 125 kV.

Stirring performance

Microchannel experiments were performed within a PDMS microfluidic chip, diameter 500 μm. A dilute aqueous suspension of bars (*ca.* 1 mg/20 mL) was pumped into the microfluidic channel at 0.5 bar pressure (AF1 dual-microfluidic and vacuum pump, Elveflow). A magnet was placed at the centre of the chip to position the particles at the mixing point. Stirring was applied at 1500 rpm and photography performed using an iPhone 4s. Water, trypan blue dye (Sigma, 10 mg/10 mL in DI H_2O) and dilute microbar suspension (2 mg/10 mL) streams were injected using syringe pumps (New Era Pumps) at 30 μL min^{-1}. Rotation was once again performed at 1500 rpm (IKAMAG).

CHAPTER FOUR

Synthesis of conductive iron oxide microfilaments using polypyrrole encapsulation

Chapter Overview

This chapter will explore the synthesis of polypyrrole, an intrinsically conductive polymer of huge biomedical interest. In particular, it will focus on the electrical and photocatalytic properties of PPy with a view towards using this visible and near-infrared-sensitive material as an alternative to the UV-sensitive TiO_2 nanoparticles in previous chapters. The effect of including an amino acid (L-lysine or L-glutamic acid) on the resulting structural, chemical and optical properties is established over acidic, neutral and alkaline pH regimes. A Fluorescamine assay is used to assess the availability of free $–NH_2$ in this doped material. Finally, a nanocomposite is synthesised comprising a Fe_3O_4 core and (amino acid-doped) PPy outer layer resulting in a magnetically responsive material. It was discovered that growing PPy onto nanoparticle surfaces was not trivial, in contrast with literature to date, and an optimisation of reaction conditions is given to produce raspberry-like composite structures. The photothermal effect of these materials is investigated. A schematic of the encapsulation process is provided in figure 52.

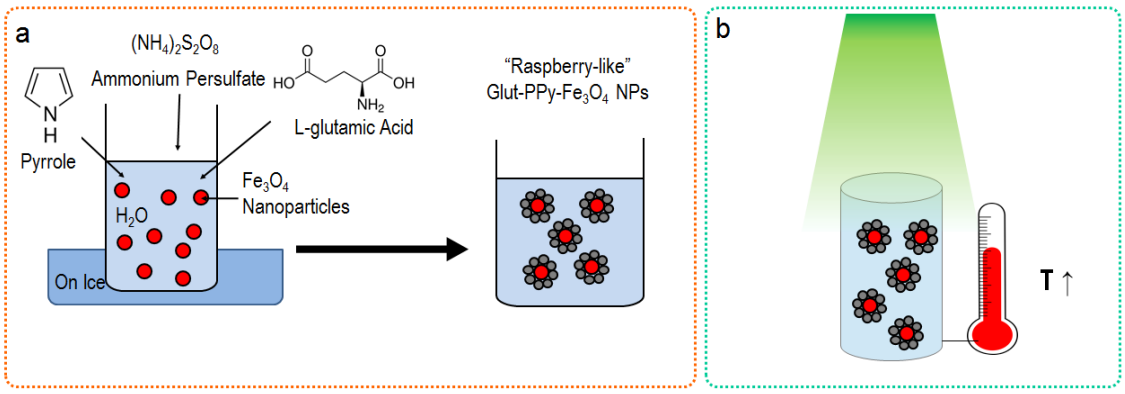

Figure 52. Chapter 5 overview. (a) Synthesis of nanocomposites with Fe_3O_4 cores and glutamic acid-doped polypyrrole coating (b) photothermal response of nanocomposites.

4.1 Amino acid doping of polypyrrole during chemical oxidative polymerisation

The inclusion of negatively charged anions into the polypyrrole mass as counter ions is a well-established route towards doping of polypyrrole with functional molecules. However, despite the usefulness of amino acid-doped polypyrrole in applications including biosensing[340] and controlled drug delivery[283], there is little work done on in this. This is particularly true for chemical polymerisation, which remains a less commonly used route to produce amino acid-doped polypyrrole despite the advantages of this method in potentially producing nanoscale, composite structures as compared with the bulk scale films typically produced by electrochemical synthesis routes. At present, a systematic study focussing optimising chemical polymerisation of polypyrrole with amino acid dopants present is not available in the literature and thus forms the first research question of this chapter.

It is expected that this synthesis process will be significantly influenced by the reaction pH, as for previous experiments using amino acids. It is known that pH has a strong effect on the synthesis of pure PPy, with greater extent of polymerisation favoured by lower pH.[341] This introduces an interesting conflict since higher pH is generally required to activate deprotonation of carboxyl groups (-COOH → $-COO^-$) of amino acids. For example, the pK_a for the carboxyls of L-lysine and L-glutamic acid are 9.0 and 4.3 respectively.[224] Therefore, it follows logically that there exists an optimal reaction condition that favours electrostatic inclusion of the amino acid without overly inhibiting the polymerisation process. A study optimising this reaction for the resulting material properties such as optical absorbance, photothermal effect, extent of

polymerisation, and availability of the terminal $–NH_2$ groups of the bound glutamate was conducted.

Three reaction pH (2, 7, 10) were studied for L-lysine, L-glutamic acid and no dopant cases. Other parameters such as reaction time, temperature, concentrations and choice of oxidant were kept constant. It was discovered that the reaction pH and inclusion of dopant had a significant effect on the extent of polymerisation and appearance of products after a 24-hour reaction period over ice (Table 11). Most significantly, solid products were only evolved for undoped and L-glutamic acid doped PPy synthesised at neutral or alkaline conditions. These results suggest that the extent of polymerisation may be strongly influenced by the presence of the amino acid and is dependent on its charge state. In the case of basic type amino acid L-lysine, which is positively charged or neutral across the pH range studied here, its presence hindered the formation of the solid polymer product significantly. On the other hand, the acidic type glutamic acid has the two negatively charged $–COO^-$ did not seem to negatively impact the yield of solid PPy.

Table 11. Initial observations for polypyrrole and doped polypyrrole synthesis after 24 hours at various reaction pH.

	No Dopant	**L-glutamic Acid**	**L-lysine**
pH 2	Black liquid	Black liquid	Black liquid
pH 7	Black solid	Black solid	Black liquid
pH 10	Black solid	Black solid	Black liquid

The optical absorbance of these products revealed more information about the chemical structure of the resulting materials. The chain length and oxidation state of the polymer leads to overall differences in the available transition bands available within the material. Thus, the optical absorbance spectra of polypyrrole samples are indicative

of the chain length and oxidation state (Table 12) of the material. This property was equally effected by the reaction pH and amino acid dopant inclusion.

Overall, neutral conditions (pH 7) promote dominance of lower energy absorption bands (2.67 – 2.76 eV) that are associated with the oxidised polymer form (Figure 53 a,b,c green lines). Additional bands at higher wavelength (1.81 eV; 1.35-1.56 eV) are indicative of di-cationic polymer and longer oligomers (tetramer). The appearance of these bands especially at neutral reaction media suggest the overall greater degree of oxidative polymerisation achieved at pH 7. The formation of this product is generally desirable as it is the form with the useful high conductivity (relevant for electrical and electrochemical applications) and optical absorbance in the useful visible and infrared regions. At both highly alkaline (blue lines) and highly acidic conditions (red lines), the bands associated with neutral oligomers (dimer, trimer) dominate.

Doping with 'basic-type' amino acid lysine inhibits the formation of polymer across all pH studied here (Figure 53 c). There is some emergence of the lower energy band at pH 10, where lysine exists in anionic form $NH_2/NH_2/COO^-$. The polymeric bands are overall higher for glutamic acid doping compared with lysine, due to the acidic nature of glutamate and associated negative molecular charge state (Figure 53 b). However, doping with glutamic acid still results in a slight inhibition of the extent of polymerisation compared with pure polypyrrole.

Table 12. Absorption bands of pyrrole derivatives and their assignation

Wavelength (nm)	Energy (eV)	Assignation
285-290	4.27 - 4.35	Dimer[342, 343]
300-303	4.09-4.13	Dimer[344]
316	3.92	Trimer[345]
450	2.76	Dicationic Polymer[346]
465-466	2.67	Cationic polymer (~10

		rings)[256]
685	1.81	Dicationic Tetramer[257] Dicationic Polymer[258]
850-920	1.35-1.46	Dicationic Polymer[347] [345]

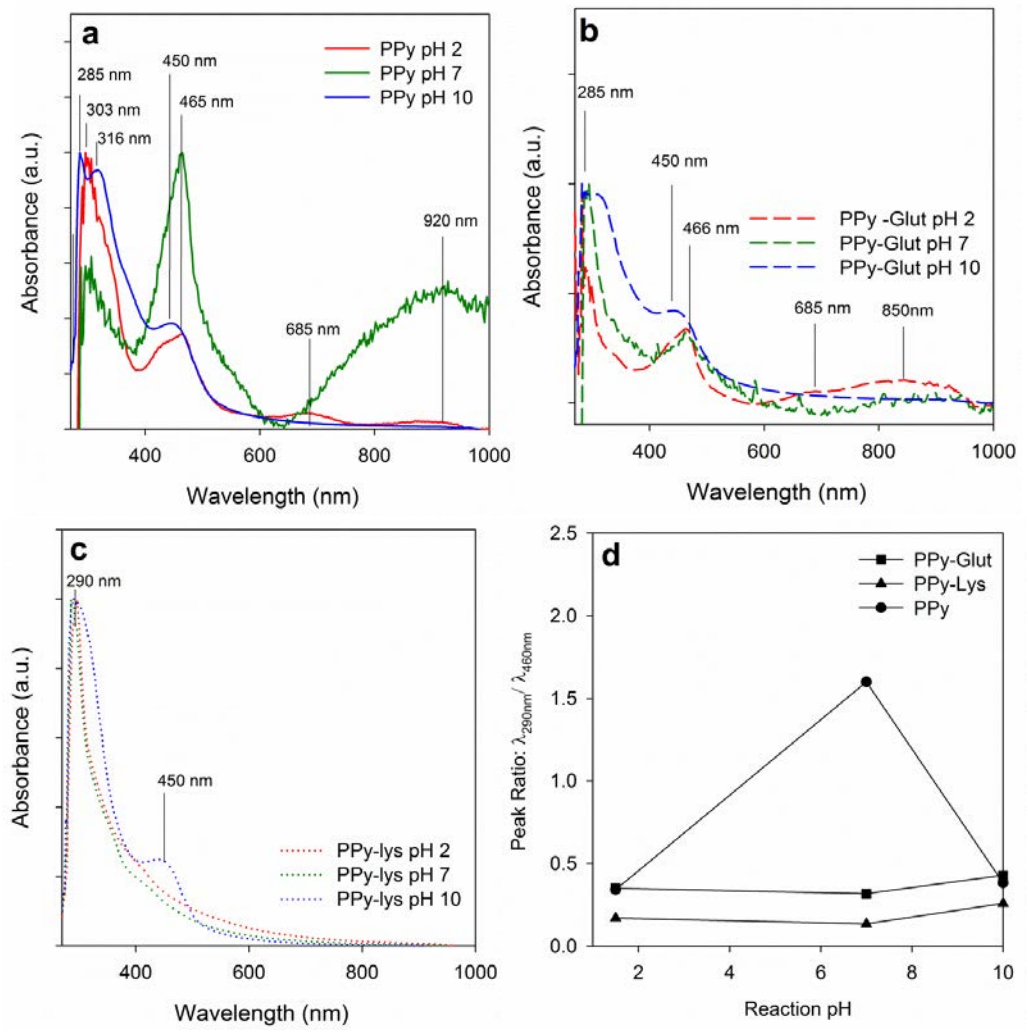

Figure 53. UV-vis absorption spectra of polymerisation products of (a) pure polypyrrole, (b) glutamic acid doped polypyrrole, and (c) lysine doped polypyrrole at pH 2, 7 and 10. (d) Calculation of absorbance band ratio $\lambda_{290nm}/\lambda_{460nm}$.

The morphology of the products was assessed using TEM and BET in the case of the solid powders evolved at pH 2 and pH 7 for the pure and glutamate-doped PPy. It was found that for pure PPy acidic conditions resulted in the formation of large granules of ca. 1μm diameter (Figure 54 a), while neutral conditions favoured granules of ca. 350

nm diameter (Figure 54 b). This result is largely consistent with previous studies of (electrochemically) polymerised PPy films whose surfaces showed a similar relation of PPy granular size depending on the reaction pH.[348] In the case of electrochemical synthesis, this was correlated with the overall rate of polymerisation which was lower for the finer granules observed at pH. In the case of the glutamate-doped PPy, both doped samples consisted of finer granules (< 50nm), with a significant increase in surface area for pH 7 compared with pH 2. This is consistent with previous reports on the role of pH on synthesis of pure PPy, but contrary to the expectations based on the pH-dependence of the charge state of the L-glutamic acid. After all, L-glutamic acid exists as a negatively charged molecule ($-COO^-$/ -COOH/$-NH_2$) at pH 7 and a neutral one (-COOH/-COOH/$-NH_2$) at pH 2. Therefore, following from the observations on the apparent charge-state dependant inhibition of L-lysine on the polymerisation of the doped PPy, it may be expected that the granules of glutamate-PPy produced at pH 7 should have an overall larger size/ lower surface area consistent with a faster growth rate.

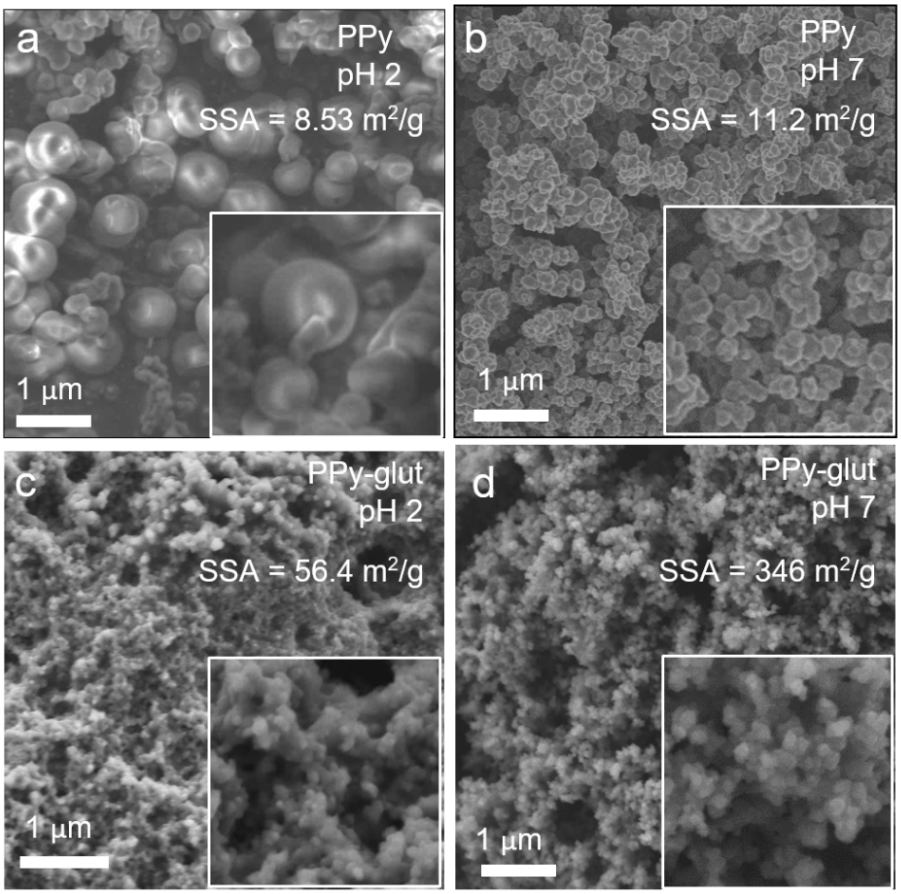

Figure 54. Scanning Electron Microscopy of (a) polypyrrole synthesised at pH 2, (b) polypyrrole synthesised at pH 7, (c) glutamic acid doped polypyrrole synthesised at pH 2, and (d) glutamic acid doped polypyrrole synthesised at pH 7.

Although the optical properties give a good indication of the polymer chain length and oxidation, they indicate nothing about the presence (or not, as the case may be) of the amino acid as the bound counter ion within the PPy mass. After all, there remains the possibility that the amino acid has not been included with the PPy preferring to take up the anions from the oxidant (SO_4^{2-}). Unfortunately, successful amino acid doping via a chemical polymerisation is currently not known in literature, although the electrochemical counterpart has been well-documented[349]. Therefore, FTIR spectra were collected for the washed and freeze dried glutamate-PPy samples to confirm the amino acid presence.

At both pH 2 and pH 7, the pure PPy spectra was a good match for the known spectra of pure PPy (Figure 56 a,b black lines) and consistent with previous data. The Emergence of $–CH_2$ bands ca. 3000 cm^{-1} that occurs for the glutamate-PPy samples (Figure 55 a,b green and red lines) may be indicative of binding of glutamic acid. $-COO^-$ bands at ca. 1400 appear only for glutamate-PPy samples. However, this peak is small and may be overlapped by nearby PPy peaks. Overall, these spectra suggest that the glutamate is present within the dried, solid PPy mass, indicating successful inclusion of the amino acid as a counterion dopant. The peak identifications used for indexing of these spectra has been given in Table 13.

Finally, to confirm the reactivity and content of the $–NH_2$ groups within the doped samples, a fluorescamine assay was used, following the same procedures as for lys-TiO_2 from previous chapters. Both samples showed a similar concentration of $–NH_2$ (Figure 56). Although a slightly higher value was recorded at pH 7 compared with pH 2, due to the significant offset on the baseline on the long wavelength side between the two spectra, this may not be meaningful. These results simply indicate that for both samples prepared, there is a content of reactive $-NH_2$.

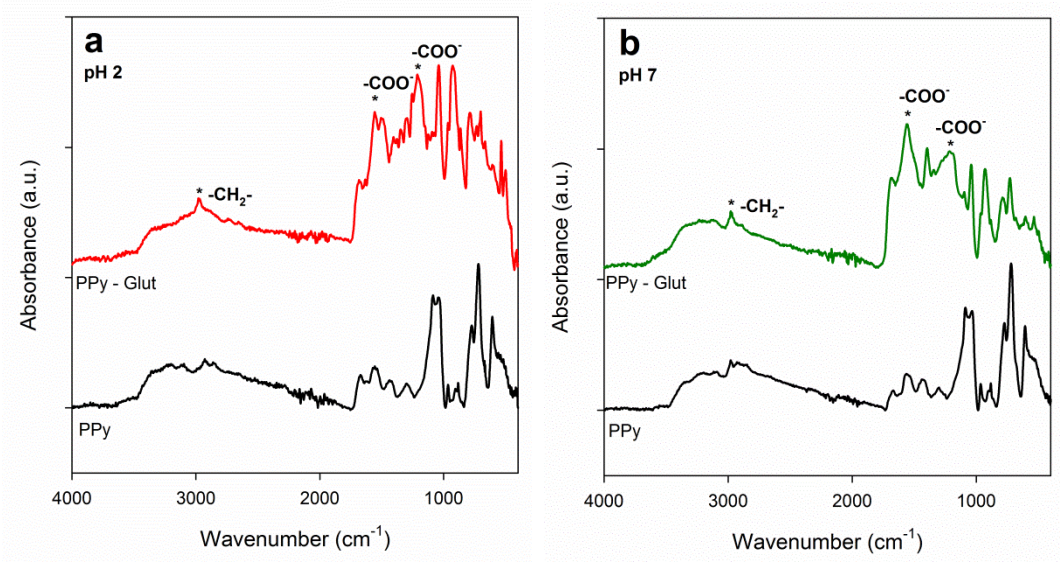

Figure 55. FTIR of PPy (black lines) and glutamate-doped PPy (red and green lines) polymerised at (a) pH 2 and (b) pH 7.

Table 13. Assignation of FTIR peaks

Wavenumber (cm^{-1})	Assignation	Reference
2970	$-CH_2$ stretch	[350]
1695	NH_3^+ stretch or α-COO^- stretch (Glut)	[351]
1560	Ring vibration (PPy)	[352]
1450	Ring vibration (PPy)	[352]
1397	α-COO^- or γ-COO^- stretch (Glut)	[351]
1197	$-CH_2$ rocking (Glut)	[351]
1090	C-N stretching (PPy)	[353]
1029	N-H in plane deformation (PPy)	[353]
920	Out of plane =CH vibration (PPy)	[354]
780	Out of plane =CH vibration (PPy)	[354]

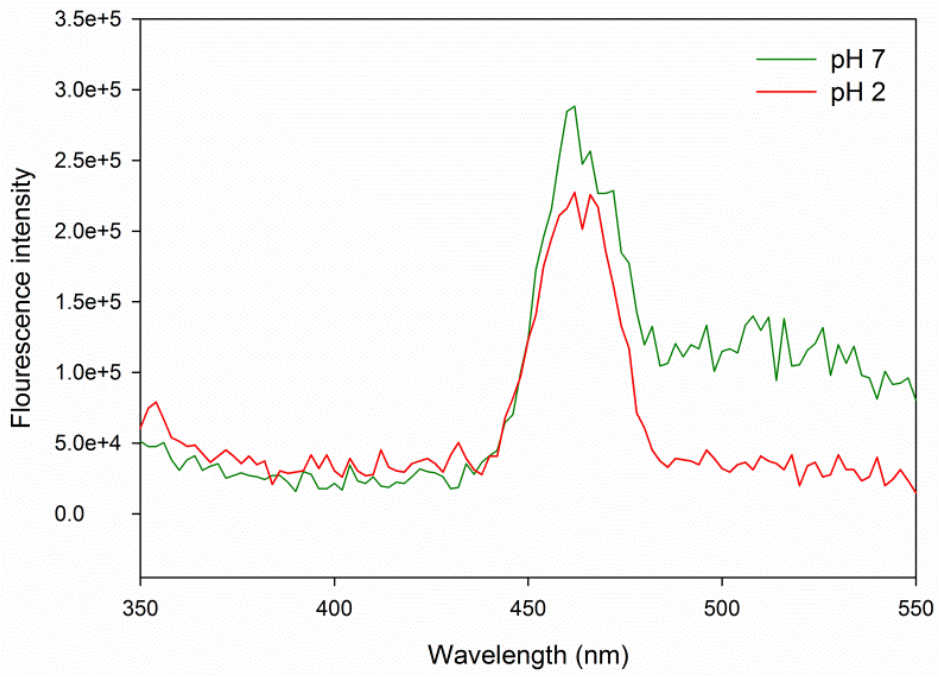

Figure 56. Fluorescamine assay of glutamate-doped PPy synthesised at pH 2 (red line) and pH 7 (green line)

4.2 Nanoparticles as seeds during polypyrrole polymerisation

Having established the successful doping of the PPy with glutamate ions, iron oxide nanoparticles were introduced as seeds during chemical polymerisation to create a composite material. A black particulate product was obtained and purified by a combination of magnetic separation and washing.

Transmission electron microscopy was performed on the resulting product, confirming the formation of a structure comprising an iron oxide nanoparticle core (dark phase) surrounded by the PPy (lighter phase) (Figure 58). This was further supported by the FTIR spectra that show the typical peaks of PPy (blue line) after polymerization reaction, compared with that of pure iron oxide (red line), with evidence of additional peaks that match well with those of PPy as reported in literature (Figure 59) These may be attributed to C=C/C-C stretching[355] (1560 cm^{-1}), C-H in-plane deformation (1190 cm^{-1}), N-H in-plane deformation (1040 cm^{-1}) and C-H out-of-plane deformation (910 cm^{-1}).[356]

The morphology of the resulting polypyrrole-Fe_3O_4 composite structures was found to be dependent on two factors: the choice of oxidant and the mass ratio between the pyrrole monomer and the Fe_3O_4 NPs. For the APS oxidant sample set (Figure 57), two different structures were observed. At high pyrrole:Fe_3O_4 ratios between 10:1 and 2:1 (Figure 57 a,b,c) a product comprising of an iron oxide core surrounded by small (<5nm) PPy nanoparticles was produced. This "raspberry-like" formation with a larger central Fe_3O_4 core surrounded by smaller, well-defined PPy granules has hitherto not been reported for composites of iron oxide and PPy. The granule size of the PPy was ca. 10-20 nm. This is significantly smaller than that typically reported for simple chemical synthesis of PPy using APS without dopants or micro-emulsion strategies, which is usually in the range of 200 – 700 nm.[357] At lower pyrrole:Fe_3O_4 ratios, the product consisted of an aggregated structure comprising polypyrrole partially surrounding but largely separate from the Fe_3O_4 NPs (Figure 57 d,e). This is more consistent with existing reports of PPy-Fe_3O_4 composites in the absence of copolymers or surfactants.

These structures observed were contrary to expectation. It was initially hypothesised that the nanoparticle would act as seeds for the polymerisation, and therefore that nucleation would begin preferentially at the nanoparticle surfaces. However, the results presented in Figure 57 directly oppose this hypothesis. The "raspberry-like" structure was created at higher concentrations of pyrrole and lower concentrations of the monomer resulted in aggregation away from the nanoparticle surface. Based on this observation, an alternative explanation is proposed. It is possible that the dominant mechanism is homogenous nucleation randomly throughout the solution. At higher pyrrole concentrations, there was a greater likelihood of some portion of the polymer granules growing upon the nanoparticle surface. This is supported by the observation that, in all cases except for 1:10 pyrrole: Fe_3O_4 ratio, there

was excess polymer formed that did not include Fe_3O_4 nanoparticles and were not able to be collected by magnetic separation.

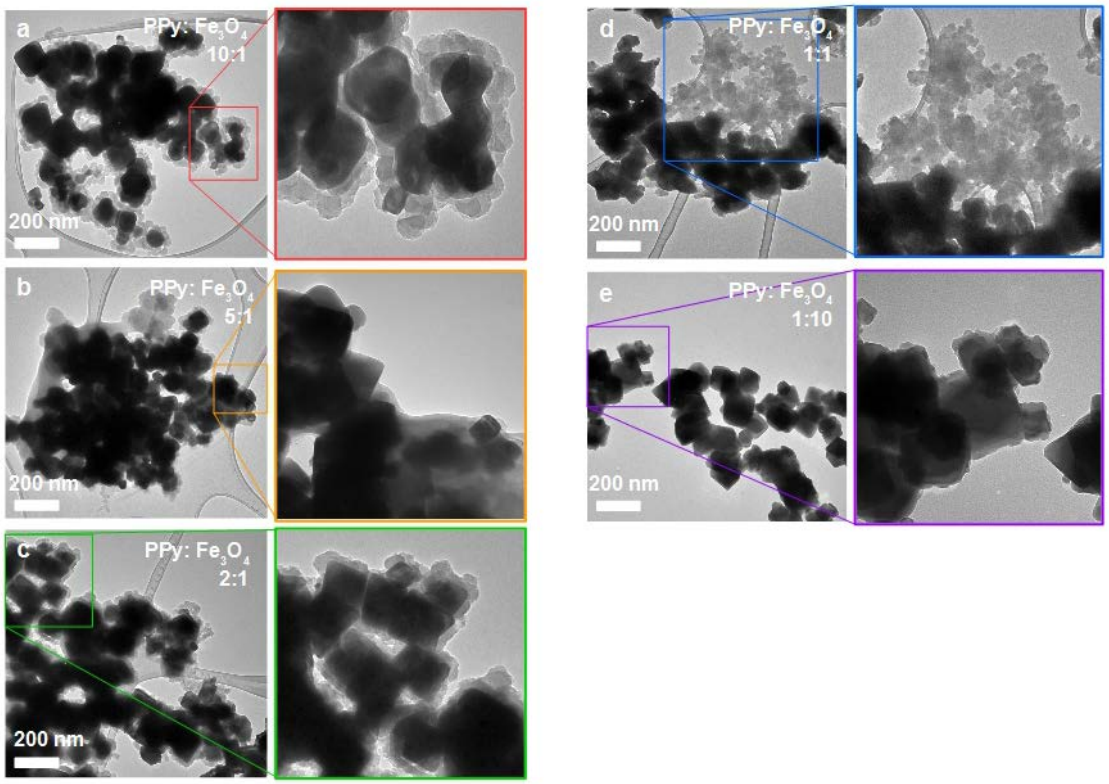

Figure 57. Transmission electron micrographs Fe_3O_4 NPs (dark phase) coated in PPy (light phase) via APS oxidant route at (a) 10:1, (b) 5:1, (c) 2:1, (d) 1:1 and (e) 1:10 pyrrole:Fe_3O_4 mass ratio.

An FTIR analysis of the raspberry-like structures resulting from APS oxidised synthesis (at 10:1 Pyrrole: Fe_3O_4 mass ratio) clearly identified the presence of PPy with its characteristic peaks (Figure 58, red line) that are absent in the pure Fe_3O_4 material (Figure 58, blue line).

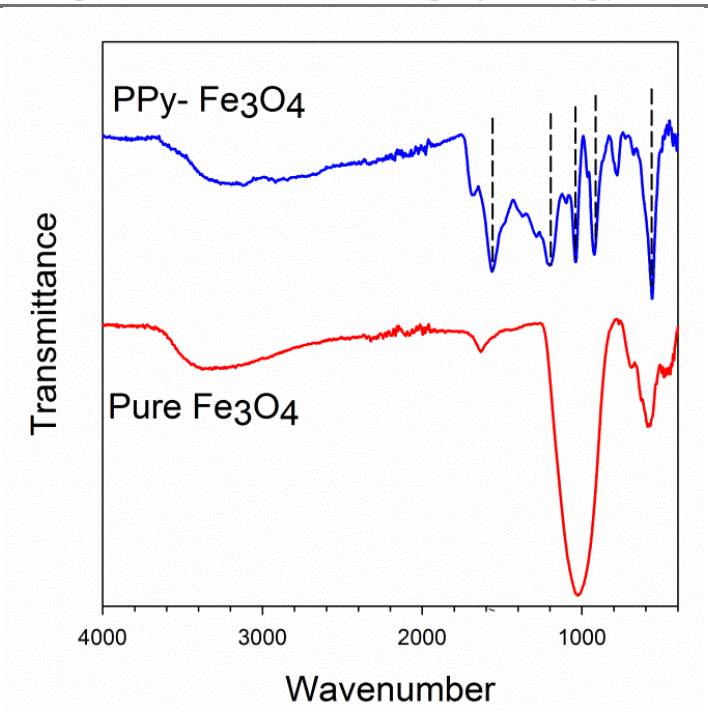

Figure 58. FTIR for Fe_3O_4 NPs (red line) and PPy-Fe_3O_4 composites created using APS synthesis route at 10:1 pyrrole: Fe_3O_4 mass ratio.

In an attempt to improve the polypyrrole coating, a sample set was produced using $FeCl_3.6H_2O$ as the oxidant. This is based on the current reports that the common ion effect will result in Fe^{3+} ions adsorbing onto the Fe_3O_4 NPs and thus serving as a site for polymerisation to begin at the seed particle surface[358]. The resulting products are presented below (Figure 59). The structures obtained were interesting and partially consistent with literature reports. It was discovered that with the $FeCl_3.6H_2O$ oxidant, an aggregated structure was only formed at high pyrrole ratios (Figure 59 a,b), while at ratios of 1:1 and below (Figure 59 c,d,e), a coating was observed on the nanoparticle surface. The morphology of this coating was unexpected, however. While Chen et al. observed a smooth, amorphous layer of PPy, here an urchin-like structure was observed. This is particularly prominent at 1:1 ratio (Figure 59 c), and is novel as far as the author is aware.

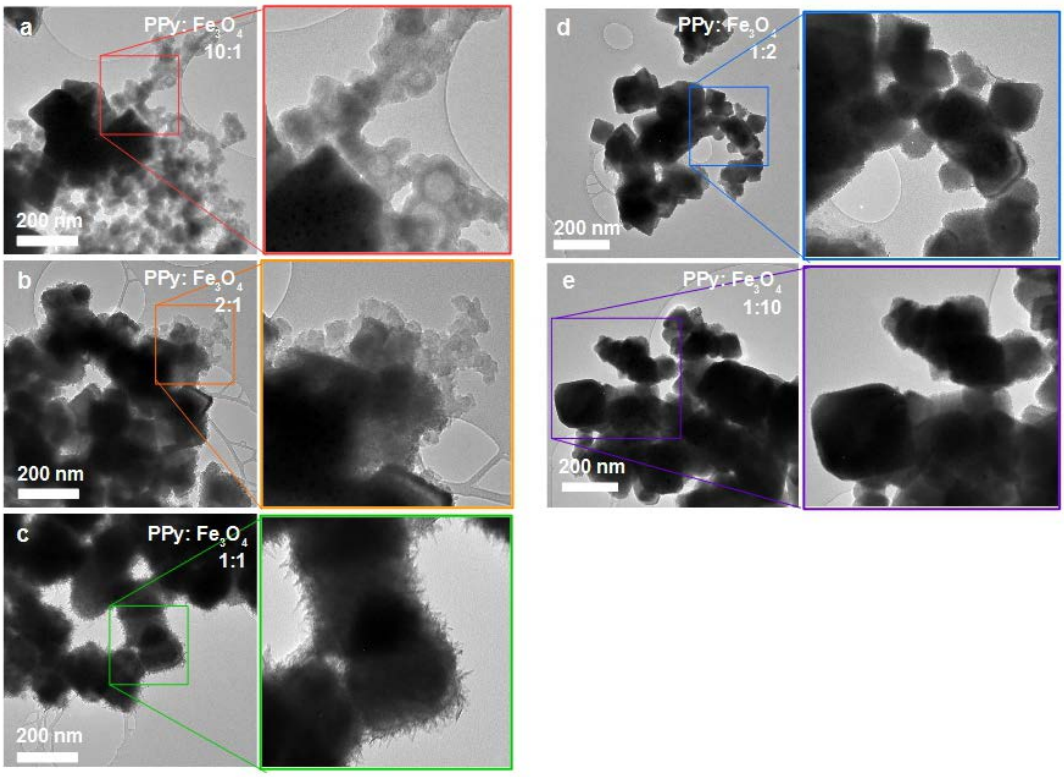

Figure 59. Transmission electron micrographs Fe_3O_4 NPs (dark phase) coated in PPy (light phase) via $FeCl_3.6H_2O$ oxidant route at (a) 10:1, (b) 2:1, (c) 1:1, (d) 1:2 and (e) 1:10 pyrrole:Fe_3O_4 mass ratio.

The experiment was then repeated using glutamic acid dopant synthesised at neutral (pH 7) conditions. The inclusion of a dopant did not seem to change the overall morphology of the composites (Figure 60 a) which appeared broadly similar to those without dopant (Figure 57 a). Upon close inspection, grains appeared slightly smaller in the doped sample (ca. 5nm for doped sample compared to ca. 20nm for undoped), which is in line with previous findings on doped PPy granular size (Figure 54). A slight change to the optical properties of the resulting doped composite was also recorded (Figure 60 b, green line), compared with the undoped composite (Figure 60 b, black line). The doped material shows a proportionately stronger absorbance in the visible compared to the infrared against the undoped standard. This may be of minor importance for photothermal applications.

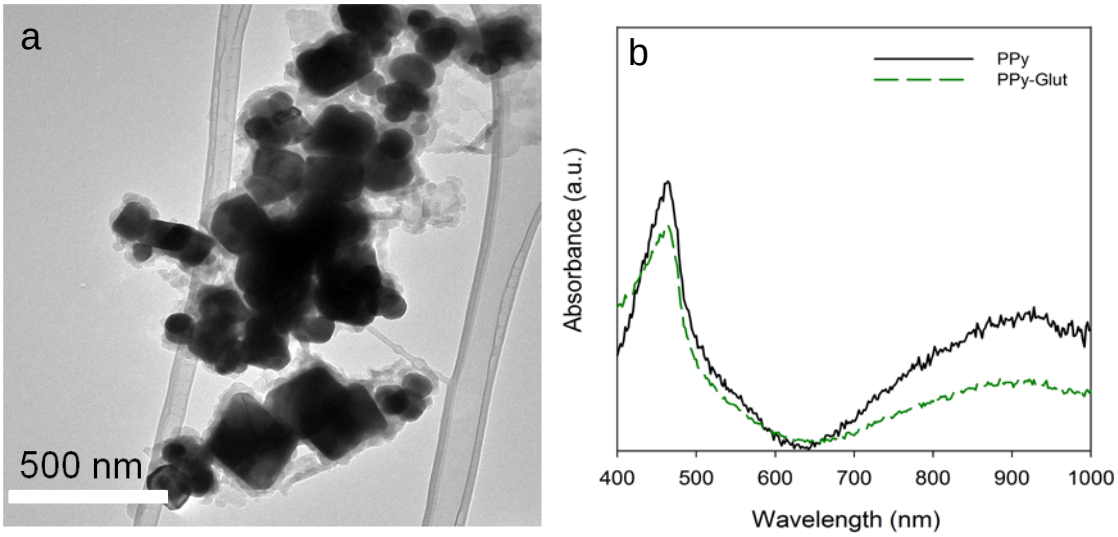

Figure 60. (a) TEM of glutamate-doped PPy granules in raspberry-like structure around iron oxide cores. (b) Optical absorbance spectra of PPy-Fe_3O_4 (black line) and Glut-PPy-Fe_3O_4 (green line).

The optical properties of the Fe_3O_4 -containing composites were assessed (Figure 61 b) and were consistent with those previously found for PPy and glutamate-PPy, showing a strong absorbance peak at 470 nm and a broad peak in the infrared beginning at 700 nm. An attempt was made to characterise the photothermal properties of this material using light at 470nm provided by an LED matching the sharp visible range absorption peak. Although most studies focus on the use of NIR lasers, in this particular case, the peak in the visible range appeared stronger than the broad infrared band. A mild photothermal effect was recorded for the polypyrrole-coated Fe_3O_4 NPs compared with the controls (Figure 62). This effect was stronger for the PPy-Fe_3O_4 composites produced from a higher PPy to Fe_3O_4 ratio resulting in the aggregated products (Figure 58 c). This may be attributed to the overall greater photothermal PPy content in these samples compared to the samples produced at a lower PPy:Fe_3O_4 ratio. An additional effect may be the distribution and effective surface area of these

composites. For the "raspberry-like" structures obtained at 10:1 PPy:Fe_3O_4, the even distribution of the granules and their increased effective surface area compared with the aggregated case at 1:1 may enhance the heat transfer out of the granules and into the surrounding liquid.

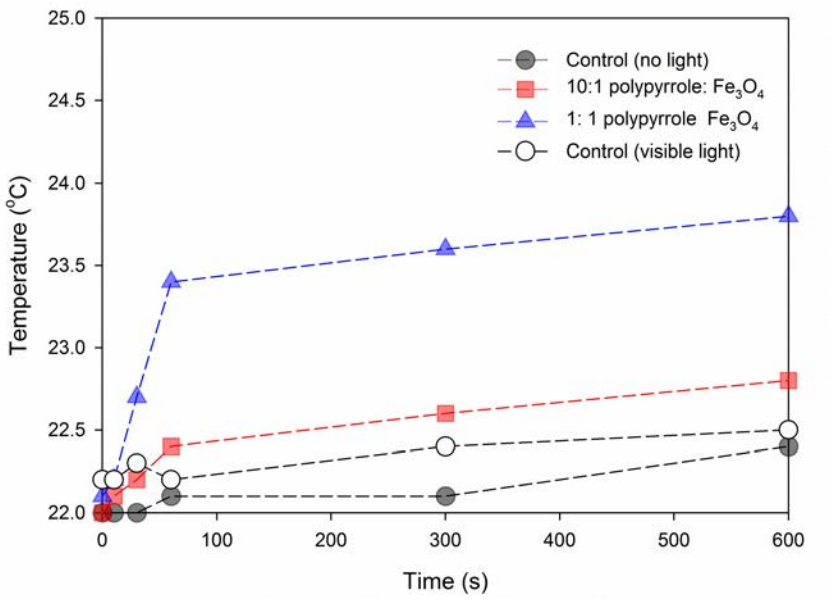

Figure 61. Photothermal effect of PPy-Fe_3O_4 nanocomposites in raspberry-like (red squares) and aggregated (blue triangle) structures compared against control without light (black circle) and control with visible light (470nm) and no nanoparticles (white circle).

Overall, this photothermal effect is less strong than that typically reported in literature for PPy. For example, Chen et al. was able to reach 50°C within 10 minutes at even lower concentrations of PPy.[359] The threshold for cellular death (of cancerous and noncancerous cells alike) is generally reported to be in the order of 70 - 80°C. The weak photothermal response reported here is therefore not directly useful for photothermal therapies. This difference in performance may result from the light source used here. It should be noted that 808nm lasers are overwhelmingly preferred in literature for the activation of PPy, and is feasibly that the low-energy LED light used here is the primary cause of the difference observed. However, there are applications that can make use of a

small temperature increase as seen here. For example, a temperature increase of 5°C is enough to trigger a payload release out of a hydrogel.[360]

Chapter Summary

The initial hypothesis that the pH will have a significant effect on the doping of PPy with amino acids was proven to be correct. It was found that between pH 2 – 10, including L-lysine in the polymerisation reaction strongly inhibits the formation of a solid polypyrrole product. For L-glutamic acid, a solid product was formed at pH 2 and 7. The product consisted of overall smaller granules than the undoped equivalent that is indicative of a decreased polymerisation rate. It was found that the polymerisation rate for glutamate-PPy may be enhanced at pH 2 compared to pH 7. However, the content of reactive $–NH_2$ groups may be a small degree higher at pH 7 due to dominant effect of the molecule's more negative charge state at this pH on its incorporation into the PPy mass. To date, a systematic study of the effect of the reaction pH on these resulting properties has not been presented in literature, and the results here represent a novel contribution that that may be broadly applicable for applications that use amino acid doped polypyrrole.

The chemical synthesis of solid granules of (glutamic acid-doped) PPy was adapted to create nanocomposites with iron oxide using a one-step nanoparticle-seeded polymerisation. Two main morphologies (raspberry-like and aggregated) were documented, and the pyrrole-to-Fe_3O_4 NP mass ratio was found to be crucially important to the resulting morphology. The raspberry-like formation was new and has not been previously observed by other scholars for such a simple, surfactant-free synthesis. This composite material displayed a photothermal effect when exposed to an LED source matching its main absorbance peak in the optical wavelength range (ca. 470nm). However, it should be acknowledged that this effect was weak compared with

the state-of-the-art as reported in literature. The weakness of this response is attributed to the LED light source being of lower power. A tuneable NIR laser is standard in literature.

4.3 Materials and Methods

Materials

Pyrrole (98% purity), Ammonium Persulfate (98% purity), Iron (III) Chloride (97% purity), Hydrochloric Acid (37% solution), Sodium Hydroxide (97% purity), L-glutamic acid (99% purity) and L-lysine (98% purity) were purchased from Sigma-Aldrich and used without further purification.

Polymerisation of PPy with amino acid dopants

A 10 mL sample of DI water was measured and placed over ice. To this, 10 mg of amino acid (L-glutamic acid or L-lysine) was added and stirred until dissolved. 100 µg of pyrrole was then added and stirred vigorously using a magnetic stirring bar and plate (1500 rpm) until a uniform emulsion is formed. Then the solution was titrated to the correct pH by adding either 0.1 mol/L NaOH or 0.1 mol/L HCl while monitored by a pH probe (Oakton pH 700). In a separate vial, 10 mg of APS was measured out and then added to the above. The reaction was kept in dark conditions over ice with 1500 rpm stirring for 24 hours unless otherwise stated. The sample was collected using gravity filtration and washed in methanol (1x), ethanol (3x) and water (3x) before being freeze dried.

Polymerisation of PPy with nanoparticle seeds

A 1 mg sample of Fe_3O_4 NPs was added to 10 mL of DI water and ultrasonicated for 3-5 minutes until a uniform suspension was formed. Then a measure of either APS or $FeCl_36H_2O$ was added and mixed over ice until the oxidant dissolved. To this, a measure of pyrrole (10 mg, 5 mg, 2 mg, 1 mg, 100 µg) was added. The mixture was

kept in dark conditions over ice with 1500 rpm stirring for 24 hours. The mass ratio of oxidant to pyrrole was 1:1. The sample was collected by placing a magnet on one side of the vessel and removing the excess reagents by pipet. The sample was washed in methanol (1x), ethanol (3x) and water (3x) by adding the wash liquid and shaking vigorously before repeating the magnetic separation. The samples were then freeze dried.

Characterisation

The resulting products were imaged using scanning electron microscopy (Zeiss Ultra) and transmission electron microscopy (Hitachi 7100, 125kV). FTIR was performed using Bruker Alpha. Optical absorbance spectra were obtained from a Tecan M200 Pro.

Fluorescamine Assay

A 1 mL solution containing 100 µg /mL of the product was prepared by weighing the freeze-dried product and ultrasonicating for 3 minutes in water. 300µL of this was taken and added to 100µL of 1mg/mL Fluorescamine solution in DMSO. The mixture was shaken vigorously then left for 10 minutes to react before being transferred to a well plate (96 well Costar, flat bottom) for UV-vis analysis (Tecan M200 Pro).

Photothermal Experiments

A 1 mL solution containing 100 µg /mL of the product was prepared by weighing the freeze-dried product and ultrasonicating for 3 minutes in water. This was placed in a 1.5mL Eppendorf tube. An LED (either 479nm or 800 nm, operated at 10mA) was placed at the side of the sample at a distance of 5mm. Temperature readings were taken by a probe that was inserted in the Eppendorf at ca. 5mm below the surface of the solution. Prior to the experiment, the temperature was allowed to stabilise for 30-60minutes (as required until a constant value was reached).

CHAPTER FIVE

Polypyrrole-coated iron oxide filaments for rotation-assisted release

Chapter Overview

In this chapter, the findings of previous chapters are combined to create a magnetically, electrochemically and optically responsive material that can be used to not only release functional molecules upon stimulation, but also can be used to enhance diffusion of those materials away from the carrier much more quickly than traditional diffusion-limited systems. A strategy to synthesise a magnetic filament comprising Fe_3O_4 cores surrounded by PPy is described and the directionally-dependant electrical properties of the resulting materials are characterised. L-glutamate is doped into the PPy, and electrochemical stimulation of the filament is used to activate release of the functional amino acid. Finally, FITC dye is used to visualise the rotation-enhanced diffusion rate of molecules out of the nanoplatform. The overall process of encapsulation, alignment, conductivity testing and release experimentation is illustrated in figure 63.

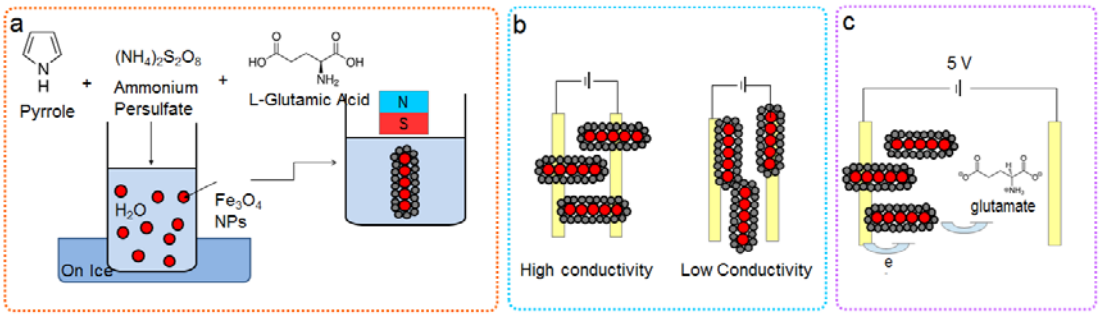

Figure 62. Chapter 6 overview. (a) Synthesis of glutamic acid-doped polyrrole-coated Fe_3O_4 filaments, (b) directional conducitivity, (b) electrochemical dedoping of glutamate.

5.1 Synthesis of PPy-Fe_3O_4 filament structures

The typical PPy synthesis was adapted for magnetically aligned filament synthesis by adapting the strategy discovered in Chapter 3 combined with the nanocomposite synthesis explored in Chapter 4 using the APS oxidisation pathway. It was found that direct synthesis of the microfilaments in one-step (seeded polymerisation of polypyrrole under a direct applied magnetic field) was less effective in the creation of filaments when using a polypyrrole coating compared to the amino acid coating in chapter 3. Significant polymerisation was initiated away from the nanoparticle surface even a the conditions previously established to create core-shell, raspberry-like structures when done without the aligning magnetic field.

Instead, a two-step procedure is preferred. Here, the premade core-shell nanomaterials are arranged by applying a parallel, horizontal magnetic field, as per Bharti et. al.[166]. This resulted in the formation of long filament-like structures (Figure 64 b) compared with the typically spheroid products usually produced by PPy encapsulation of Fe_3O_4 (Figure 64 a) and is similar time with previous results on amino acid coated iron oxide nanomaterials as presented in chapter 3. The filament-like structures had an average length of ca. 138μm. The filaments were highly disperse, showing a high standard deviation in filament length (σ_g = 1.83) (Figure 65) that is consistent with grow mechanism that is dominated by random collision followed by successful adhesion.

The TEM (Figure 64 c,d) showed the microstructure of the filament with evidence of the encapsulation polypyrrole coating (light phase). It was found that the PPy was not in a raspberry-like form around the Fe_3O_4 cores as for the isotropic encapsulation at the same pyrrole:Fe_3O_4 ratios (Chapter 5, Figure 58a), but rather in an

aggregated, amorphous form. It is not clear why this difference was observed. One possibility is that the raspberry-like form is not robust enough to withstand the magnetic field induced collisions.

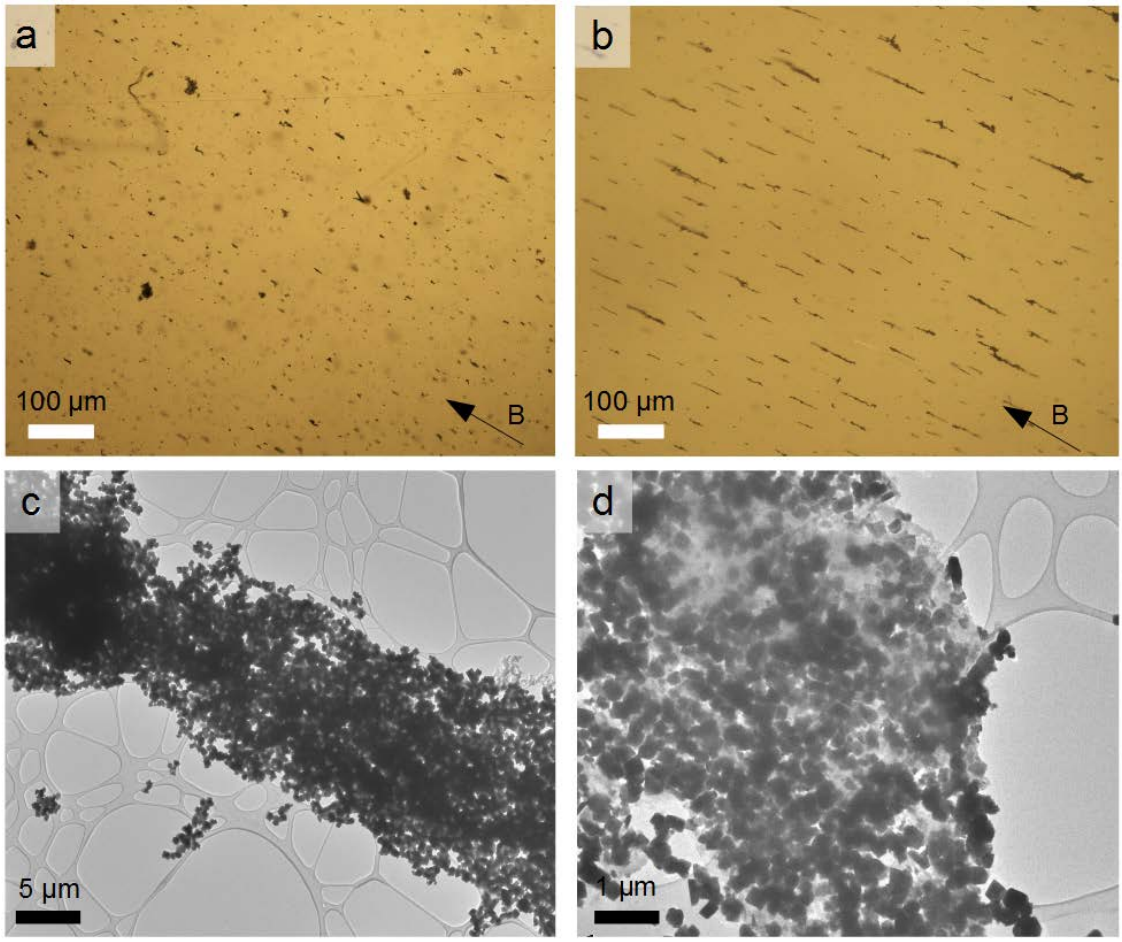

Figure 63. Optical micrograph showing (a) isotropic product typical of synthesis in the absence of magnetic field and (b) filament-like structures aligned in applied magnetic field direction. (b) Length distribution and (c, d) transmission electron micrographs of the same.

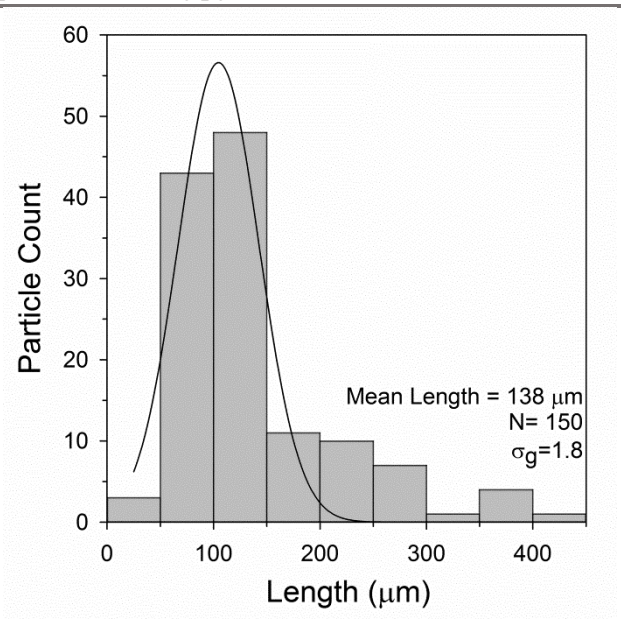

Figure 64. Length distribution of PPy-Fe_3O_4 microfilaments.

5.2 Electrical properties of anisotropic structures

The filaments displayed highly anisotropic electrical conductivity arising from the PPy coating. When aligned parallel to the interdigitated electrode array by the action of an externally applied magnetic field (Figure 66 a), the relatively high discontinuity in the filament arrangement leads to a high resistance recorded of 5.3 MΩ. However, upon rotating the field to act in the perpendicular direction, resulting in higher continuity between the electrodes, the resistance decreases by a factor of 300 down to 16.5kΩ (Figure 66c). It was found that the conductivity scales linearly with the concentration of filaments (Figure 67), as may be expected.

This result is novel as far as the author is aware. This direction-dependant conductivity may be useful for magnetically-actuated switching of microcircuitry. However, in this dissertation, it is relevant to the electrochemically activated dedoping /drug release mechanism.

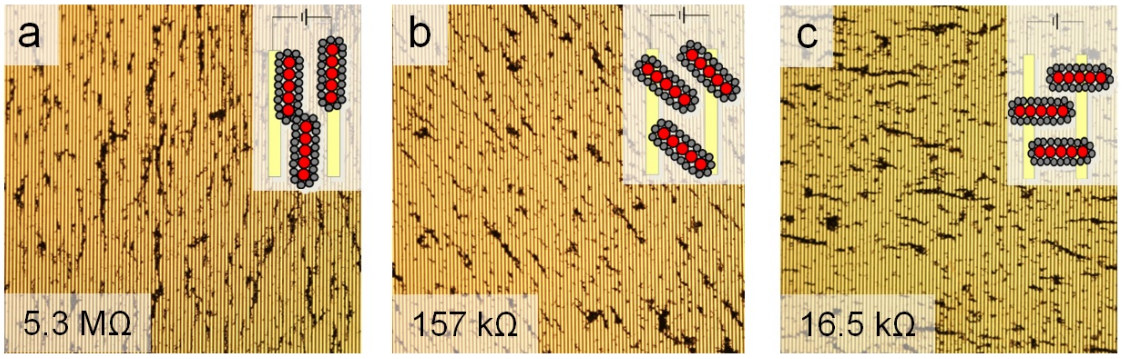

Figure 65. Micrographs showing alignment and corresponding resistance of PPy-Fe_3O_4 microfilaments in (a) parallel, (b) 45° oblique and (c) perpendicular to electrode array.

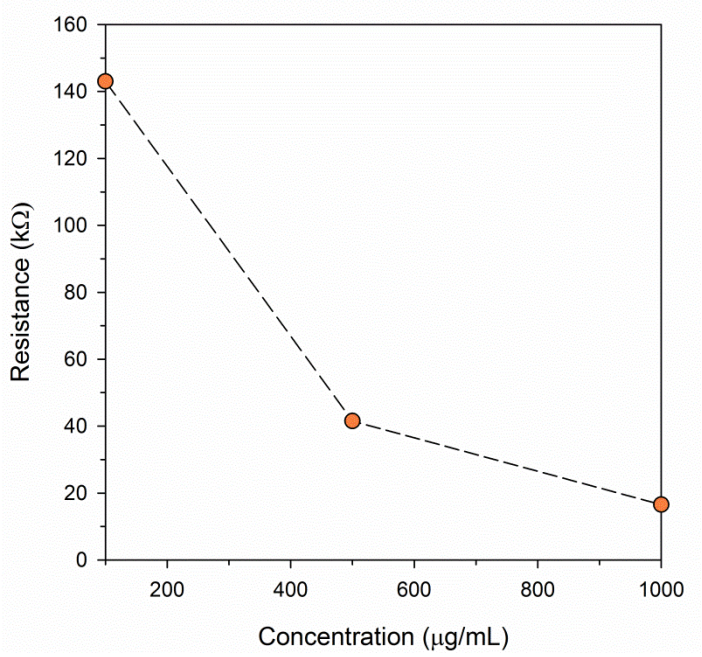

Figure 66. Recorded resistance of PPy-Fe_3O_4 microfilaments arranged perpendicular to the electrode array at various concentrations.

5.3 Electrochemical dedoping of glutamate

Given the promising electrical properties that were discovered, an electrochemical drug release experiment was devised using a glutamate-PPy coated Fe_3O_4 filament that was produced by including L-glutamic acid in the typical polymerization solution, as per *Chapter 4*. The filament product was then aligned over electrodes in a PBS solution (in the more conductive, perpendicular arrangement (Figure 67 a) and a -5V potential

applied in order to forcibly reduce the PPy and thus release the glutamate dopant electrochemically (Figure 68 a,b).

The glutamate was assayed by taking aliquots of the particle-free solution and then using the same fluorescamine assay as in previous chapters. A significant increase in the free glutamate content was confirmed after applying the potential compared with the control over the same conditions (Figure 68 c), illustrating the effect of electrochemical dedoping action. It should be noted that the control did not show a zero glutamate baseline. This can be attributed to the passive leaching of glutamate out of the PPy. A similar passive release effect has been consistently reported for other dopants into PBS solution. For example, dexamethasone[361] and ciprofloxacin[362] will both show a passive diffusion profile. In fact, this passive, slow sustained release is itself useful method of drug delivery. However, the ability to enhance this and create an increased burst of the loaded molecule as required, such as is shown here, creates additional possibilities and is a significant result.

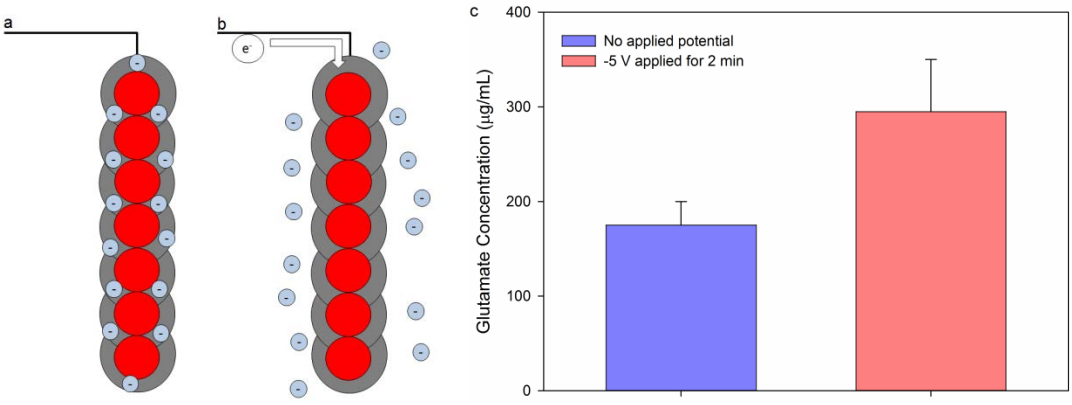

Figure 67. (a, b) Schematic illustrating electrochemical dedoping of bound glutamate anions by applying a negative potential. (c) Fluorescamine assay of particle-free solution for perpendicular aligned glut-PPy-Fe_3O_4 filaments in PBS after 2 min with no applied potential (black line) and -5V (red line).

5.4 Magnetic-rotation assisted delivery

In *Chapter 3*, the ability of rotating filaments to create local mixing vortices was shown. In the previous section, a sustained passive release of the dopant from the PPy was observed. Following these two observations, an experiment was devised combining these observations in order to use the microscale vortexing of rotating filaments to improve the diffusion rate of materials out of the polypyrrole coating, thus giving another method of creating controlled, burst release.

Here, to visualise the possibility of enhanced release, a fluorescent dye (FITC) was bound to the PPy-Fe_3O_4 filaments by including the dye during standard chemical polymerisation. The elution of this dye out of the filaments in PBS was observed with and without a rotating magnetic field (Figure 69 a,b). It was hypothesised that, since the passive elution is usually diffusion-limited, introducing the rotating action will enhance the diffusion rate by introducing eddy mixing local to the microfilament. Figure 69c shows the time lapse of this dye as it diffuses away from the microfilaments and confirmed this hypothesis. A significantly faster rate was observed for the rotating filaments compared to the stationary control case. The release rate was correlated to the rotation speed, increasing with increasing rotation rate as expected.

This is a significant result as it gives an alternative pathway for loading and release that has not been previously proposed in literature to date. It is possible to imagine a system that uses a stationary magnetic field source to locate and move the loaded microfilaments to location and then creates controlled, fast release by rotating the field. Such a system would be a potentially impactful lab tool. However, the author wishes to acknowledge that further studies are required before this may be implemented

to in vivo experimentation. Firstly, the currently large size of the microfilaments (in the 100 µm scale) is not compatible with biological systems due to mobility issues. Secondly, the rapid, propeller-like motion may cause significant cellular damage, although studies are lacking in this area. If properly controlled, this may create a synergistic effect that is suitable for cancer treatment as per other cytotoxic methods such as photothermal treatment[363]. However, this remains a distant application at this stage and is far beyond the reach of this dissertation.

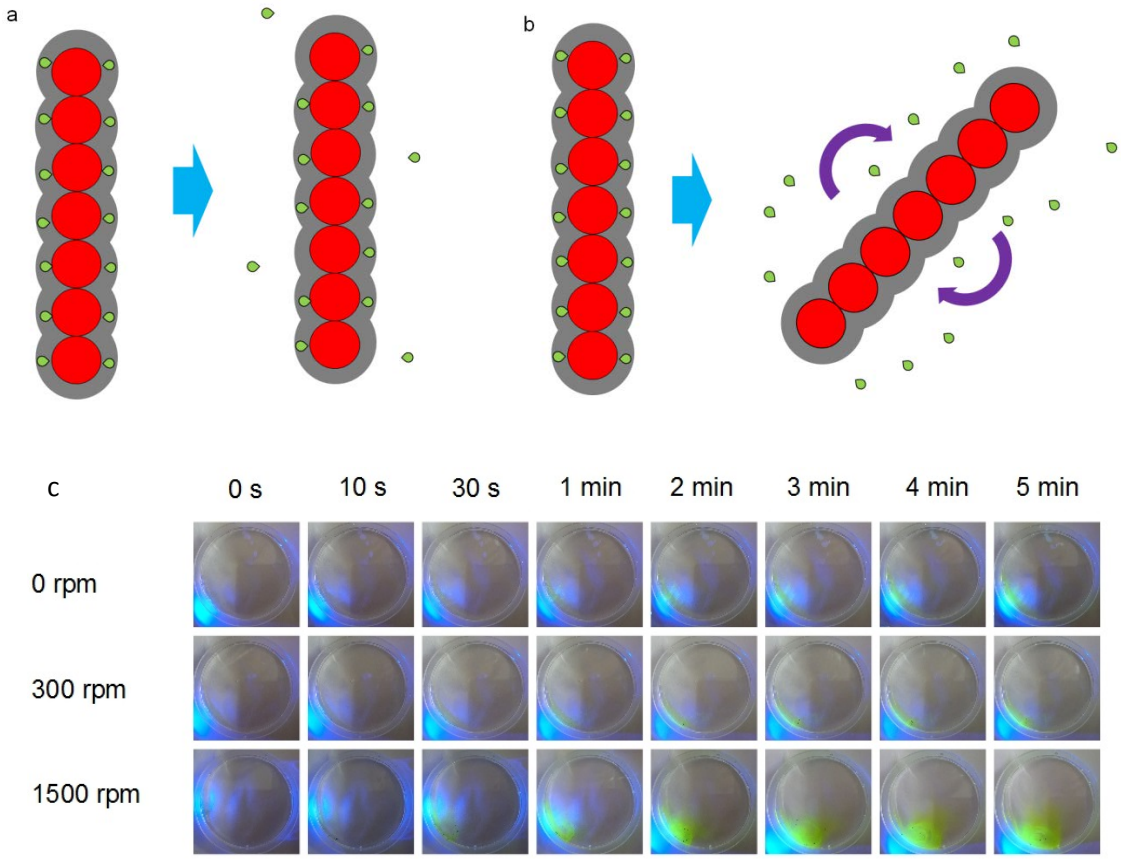

Figure 68. Timelapse of eltuion of FITC from PPy-Fe_3O_4 filaments at variable rotation rates.

Chapter Summary

In this chapter, a synthesis for PPy-encapsulated Fe_3O_4 filaments was presented based on successfully adapting protocols established in previous chapters. It was found that the morphology of the anisotropic material was different from the isotropic material at the same experimental conditions and may point to the significance of the seed surface area-to-pyrrole monomer ratio.

The resulting material displayed interesting anisotropic electrical properties deriving from the PPy coating. By manipulating the externally applied magnetic field, it is possible to control the direction of the magnetic filament relative to the electrodes and obtain a 300 fold change in conductivity by rotating through 90^o.

By applying a negative potential to a filament structure with a doped glutamate-PPy coating, it was possible to induce a burst release of the glutamate ion into solution via electrochemical reduction. This presents another, electrochemical route towards controlled delivery.

Finally, the filament-like structures showed similar responses to a dynamic magnet field as before. The rotation behaviour was used here to improve the elution rate of a model molecule (FITC dye) whose release from a PPy matrix is ordinarily diffusion-limited, demonstrating the concept of rotation-assisted delivery from such a system.

5.5 Materials and Methods

Synthesis of PPy-Fe_3O_4 filaments

A 1mL sample of Fe_3O_4 NPs was dispersed in 10 mL of DI water by ultrasonication for 3 minutes until an even suspension was formed. 100 µg of pyrrole was added this and mixed until an emulsion formed. Where appropriate, 100 µg of L-glutamic acid was added to the above and stirred until fully dissolved. Then 100 µg of APS was dissolved in 0.1 mL of DI water. The solution containing Fe_3O_4 NPs/ Pyrrole was placed into a wide, shallow vessel above a magnetic stirring plate operating at 1500 rpm. A rare earth magnet was placed above the vessel at a distance of ca. 2.5 cm above the stirring plate (see *Appendices Section 3. Magnetic alignment setup*). The solution containing APS was then added dropwise to the solution contain Fe_3O_4 NPs/ Pyrrole. The reaction was kept in dark conditions and allowed to react for 24 hours. The resulting materials were removed using a pipette and placed into a conical tube (Falcon, 50mL). A magnet was placed on the side of the sample and the excess solution removed by pipette. The material was washed in methanol (1x), ethanol (3x) and water (3x) by gently shaking with the wash liquid, then repeating the magnetic separation.

Material Characterisation

The filaments were characterised using an optical microscope at 10x magnification and transmission electron microscope (Hitachi 7100, 125kV).

Electrical conductivity

A 50µL drop containing 100 µg/ mL of the filaments was placed on top of an interdigitated electrode array (Dropsens). A rare earth magnet was then used to align the filaments relative to the electrodes with aid of an optical microscope. The sample was

allowed to dry overnight before resistance measurements were made using a multimeter (Keithley)

Electrochemical Dedoping

A sample comprising a dried arrangement of glutamic acid-doped polypyrrole Fe_3O_4 filaments on a Dropsens electrode array was placed at the bottom of a vessel containg ca. 1mL PBS. A -5V potential was passed through the electrode with a Pt counter electrode for 2 min. Then, a 100µL sample of the PBS solution was taken and added to 30µL of 1mg/1mL fluorescamine in DMSO and reacted for 10 min before UV-vis analysis (Tecan M200Pro).

Binding and dispersion of FITC dye

A dye was included in the synthesis of PPy-Fe_3O_4 bars by first preparing 1mg FITC in 10mL H_2O. 1 mg of Fe_3O_4 was then added to this and sonicated for 3 minutes. 100µg of pyrrole was added and shaken until an emulsion formed. This mixture was placed in the same setup as before (Appendices Section 1). 100µg of APS was dissolved in 100µL of DI water and added to the above dropwise. The reaction was allowed to proceed for 24 hours in dark conditions with a constant 1500 rpm. The sample was collected and washed as previously. A 50 µL sample of solution containing 100µg/mL of the product was injected into a 45mm petri dish containing 10mL of PBS buffer solution using a Gilson P200. The photography was recorded on a Sony Xperia Z5. A blue LED was used to improve the visibility of the fluorescent dye.

CHAPTER SIX

Conclusions and Outlook

In this dissertation, a broad range of results pertaining to several important topics in nanomaterials for drug release were shown.

Firstly, a photocatalytic system based on amino acid-functionalised TiO_2 was presented. This system was able to bind and release $–NH_2$ reactive molecules as modelled by FITC dye and anti-inflammatory drug ketoprofen. The overarching importance of reaction pH in directing the interaction of amino acids with metal oxide surfaces determined. An acidic condition favours binding of the amino acid by the –COOH group(s) to the metal oxide surfaces, a configuration that is favourable for subsequent binding of useful moieties to the terminal $–NH_2$. The mechanism of the photocatalytic release of adsorbed molecules was clarified by experimentation. Upon illumination with UV-A, there is simultaneous release and redox cyclization of the amino acid recorded. Where the amino acid is terminated by the model drug ketoprofen, it is possible to release the drug via this photocatalytic pathway. In all experiments conducted, there exists an optimal illumination time after which the degradation of the surrounding organic materials overtakes their release into solution. This time period was found to be between 5-10s. This is a novel observation so far not reported in literature.

The reaction pH of amino acid functionalization will also cause a significant effect on the flocculation dynamics of the nanoparticles in question. Aggregation is promoted by higher pH and higher concentrations of the amino acids. The mechanism is most likely electrostatic interaction between nearby $–NH_3^+$ and $–COO^-$ groups. This flocculation may be exploited to assembly anisotropic filaments of Fe_3O_4 nanoparticles under a directing magnetic field. These magnetic filaments responded to an applied rotating magnetic field to create microscale vortices that aid local mixing and may be helpful in overcoming typically diffusion-limited delivery applications.

The doping of polypyrrole with amino acids was also discovered to be pH-governed with favourable oxidation of pyrrole monomer and doping of the resulting polymer only occurring at pH where the amino acid existing in an anionic form. Conversely, protonated, cationic $–NH_3^+$ groups present will inhibit the oxidative polymerisation of polypyrrole. When polypyrrole is used as a coating for the magnetic filament structure, a directionally dependant conductivity is observed that can be controlled by changing the direction of the external magnetic field. The glutamic acid-doped polypyrrole can be electrochemically dedoped, presenting an alternate controlled delivery route. With an appropriate payload adsorbed in the PPy matrix (modelled with FITC dye), the rapid vortexing motion of the magnetic filaments can be used for a rotation-enhanced delivery mode that is novel in literature to date.

Although several important results were obtained, there remain several unanswered questions and avenues for future scholarship. Going forward, the following directions may y

1. Improve the structure of the magnetic filaments

The magnetic filament structures created in Chapter 3 and Chapter 5 should be improved. In particular, their large size distribution is currently far from ideal. Due to the proposed growth mechanism by collision, a random event following a natural distribution, it is unlikely that the structures can be improved during the synthesis stage. Instead, post-separation should be investigated. Horizontal travel under an accelerating magnetic field has been successfully applied by other researchers to size-sort magnetic nanoparticles and may be useful here.[364]

Additionally, it is clear that assembly under an in-situ magnetic field is preferable to a long one-step synthesis as is presented in chapter 3. Therefore, the amino

acid coated iron oxide fibres should be reconsidered in this context. Is it possible, for example, to create first a functionalised nanoparticle and then assemble these temporarily under a stationary parallel magnetic field, as per the polypyrrole-coated material? This would potentially allow more flexibility in terms of the magnetic fibre size as it can be live-monitered and controlled.

Furthermore, some studies on additional methods of synthesising similar anisotropic structures bears investigation. In particular, will precipitation of Fe_3O_4 NPs under a strong magnetic result in anisotropic structures?

2. Exploit photothermal character of Polypyrrole-coated Fe_3O_4

A slight photothermal response was recorded in Chapter 4. This should first be investigated further. Particularly, the methodology may be improved to fully exclude any environmental effects. A fully temperature controlled system (e.g. water bath) should be used and the experiment should be scaled up to minimise the error. The parameters of material type (e.g. raspberry versus agglomerate), material concentration, rotation rate, and wavelength of light used should be explored, decouple and optimised before these results are published. It is expected that the heating rate will scale with concentration. It would be of interest to confirm that these particular materials absorb in the NIR as per literature reports and a similar heating rate should be recorded at these wavelengths and compared against visible wavelengths Finally, the effect of having a rotating magnetic field in place while the photothermal effect is in action should be investigated. It is possible that the heating rate at some distance from the filaments can be improved by micro-vortexing as heat transfer is also a diffusion-limited process. After this is established, the nanoplatform should be coupled with a heat-sensitive component to open another avenue for stimuli-responsive release. A micro-hydrogel

bead impregnated with a soluble drug and small enough to sit on the surface of the filaments without impeding their rotation is a potential platform.

3. Patterned release of pharmaceuticals

Although it appears that the glutamate ions may be ejected from the filaments by applying a negative potential, it is important to follow this by attaching a useful moiety to the end of the glutamate linker, as per the ketoprofen model drug in other experiments in this dissertation. It would also be of impact to show that the release can be made directional by controlling the magnetic field.

4. Polypyrrole-coated Fe_3O_4 as dynamic platforms for neuron growth

Related to the above, a growth factor should be attached to the glut-PPy-Fe_3O_4 filaments and used for dynamic neuron growth platforms. It is known that neurons will grow on growth factor-containing PPy substrates. This is especially enhanced when there is current passing through the PPy. The ability to preferentially grow neurons on the magnetic filaments with neurite extension along the filament length, followed by the ability to move the magnetic platform would be an important achievement.

References

1. Wu, J. and M.J. Sailor, *Chitosan Hydrogel-Capped Porous SiO2 as a pH Responsive Nano-Valve for Triggered Release of Insulin.* Advanced Functional Materials, 2009. **19**(5): p. 733-741.

2. Xia, L.-W., et al., *Nano-structured smart hydrogels with rapid response and high elasticity.* Nature Communications, 2013. **4**.

3. Hu, Q., P.S. Katti, and Z. Gu, *Enzyme-responsive nanomaterials for controlled drug delivery.* Nanoscale, 2014. **6**(21): p. 12273-12286.

4. Ganta, S., et al., *A review of stimuli-responsive nanocarriers for drug and gene delivery.* Journal of Controlled Release, 2008. **126**(3): p. 187-204.

5. Murakami, Y. and M. Maeda, *DNA-responsive hydrogels that can shrink or swell.* Biomacromolecules, 2005. **6**(6): p. 2927-2929.

6. Ruiz-Hernández, E., A. Baeza, and M. Vallet-Regí, *Smart Drug Delivery through DNA/Magnetic Nanoparticle Gates.* ACS nano, 2011. **5**(2): p. 1259-1266.

7. Wen, H., et al., *Engineered Redox-Responsive PEG Detachment Mechanism in PEGylated Nano-Graphene Oxide for Intracellular Drug Delivery.* Small, 2012. **8**(5): p. 760-769.

8. Mura, S., J. Nicolas, and P. Couvreur, *Stimuli-responsive nanocarriers for drug delivery.* Nature materials, 2013. **12**(11): p. 991-1003.

9. El-Sayed, I.H., X. Huang, and M.A. El-Sayed, *Selective laser photo-thermal therapy of epithelial carcinoma using anti-EGFR antibody conjugated gold nanoparticles.* Cancer Letters, 2006. **239**(1): p. 129-135.

10. Zhang, F., et al., *Mesoporous multifunctional upconversion luminescent and magnetic "nanorattle" materials for targeted chemotherapy.* Nano Letters, 2011. **12**(1): p. 61-67.

11. Hergt, R., et al., *Magnetic particle hyperthermia: nanoparticle magnetism and materials development for cancer therapy.* Journal of Physics: Condensed Matter, 2006. **18**(38): p. S2919.

12. Chiang, C.-Y., et al., *Formation of TiO 2 nano-network on titanium surface increases the human cell growth.* dental materials, 2009. **25**(8): p. 1022-1029.

13. Gao, L., D. Zhang, and M. Chen, *Drug nanocrystals for the formulation of poorly soluble drugs and its application as a potential drug delivery system.* Journal of Nanoparticle Research, 2008. **10**(5): p. 845-862.

14. Hillaireau, H. and P. Couvreur, *Nanocarriers' entry into the cell: relevance to drug delivery.* Cellular and Molecular Life Sciences, 2009. **66**(17): p. 2873-2896.

15. Bae, Y.H. and K. Park, *Targeted drug delivery to tumors: myths, reality and possibility.* Journal of Controlled Release, 2011. **153**(3): p. 198.

16. Shrestha, N.K., et al., *Magnetically Guided Titania Nanotubes for Site-Selective Photocatalysis and Drug Release.* Angewandte Chemie International Edition, 2009. **48**(5): p. 969-972.

17. Tarn, D., et al., *Mesoporous silica nanoparticle nanocarriers: biofunctionality and biocompatibility.* Accounts of Chemical Research, 2013. **46**(3): p. 792-801.

18. Mahmoudi, M., et al., *Assessing the In Vitro and In Vivo Toxicity of Superparamagnetic Iron Oxide Nanoparticles.* Chemical Reviews, 2012. **112**(4): p. 2323-2338.

19. Di Paola, A., et al., *Highly Active Photocatalytic TiO2 Powders Obtained by Thermohydrolysis of TiCl4 in Water*. The Journal of Physical Chemistry C, 2009. **113**(34): p. 15166-15174.

20. Nakata, K. and A. Fujishima, *TiO 2 photocatalysis: design and applications.* Journal of Photochemistry and Photobiology C: Photochemistry Reviews, 2012. **13**(3): p. 169-189.

21. Shrestha, N.K., et al., *Magnetically Guided Titania Nanotubes for Site-Selective Photocatalysis and Drug Release.* Angewandte Chemie International Edition, 2009. **48**(5): p. 969-972.

22. Kwak, D.-H., J.-B. Yoo, and D.J. Kim, *Drug release behavior from nanoporous anodic aluminum oxide.* Journal of nanoscience and nanotechnology, 2010. **10**(1): p. 345-348.

23. Wang, T., et al., *Potential application of functional porous TiO2 nanoparticles in light-controlled drug release and targeted drug delivery.* Acta Biomaterialia, 2015. **13**: p. 354-363.

24. Mendive, C.B., et al., *Oxalic acid at the TiO2/water interface under UV(A) illumination: Surface reaction mechanisms.* Journal of Catalysis, 2015. **322**: p. 60-72.

25. Tachikawa, T., et al., *Photocatalytic Cleavage of Single TiO2/DNA Nanoconjugates.* Chemistry – A European Journal, 2008. **14**(5): p. 1492-1498.

26. Zhang, J. and Y. Nosaka, *Mechanism of the OH radical generation in photocatalysis with TiO2 of different crystalline types.* The Journal of Physical Chemistry C, 2014. **118**(20): p. 10824-10832.

27. Gupta, S.M. and M. Tripathi, *A review of TiO2 nanoparticles.* Chinese Science Bulletin, 2011. **56**(16): p. 1639.

28. Li, W., et al., *A Perspective on Mesoporous TiO2 Materials.* Chemistry of Materials, 2014. **26**(1): p. 287-298.

29. Liu, N., et al., *A review on TiO2-based nanotubes synthesized via hydrothermal method: Formation mechanism, structure modification, and photocatalytic applications.* Catalysis Today, 2014. **225**: p. 34-51.

30. Jiang, D., S. Zhang, and H. Zhao, *Photocatalytic degradation characteristics of different organic compounds at TiO2 nanoporous film electrodes with mixed anatase/rutile phases.* Environmental science & technology, 2007. **41**(1): p. 303-308.

31. Song, Y.-Y., et al., *Amphiphilic TiO2 Nanotube Arrays: An Actively Controllable Drug Delivery System.* Journal of the American Chemical Society, 2009. **131**(12): p. 4230-4232.

32. Wang, J.-X., et al., *TiO 2 nanoparticles translocation and potential toxicological effect in rats after intraarticular injection.* Biomaterials, 2009. **30**(27): p. 4590-4600.

33. Signoretto, M., et al., *Effect of textural properties on the drug delivery behaviour of nanoporous TiO2 matrices.* Microporous and Mesoporous Materials, 2011. **139**(1–3): p. 189-196.

34. Qin, Y., et al., *Highly water-dispersible TiO2 nanoparticles for doxorubicin delivery: effect of loading mode on therapeutic efficacy.* Journal of Materials Chemistry, 2011. **21**(44): p. 18003-18010.

35. Gynther, M., et al., *Brain uptake of ketoprofen–lysine prodrug in rats.* International Journal of Pharmaceutics, 2010. **399**(1): p. 121-128.

36. Anderson, R.R. and J.A. Parrish, *The Optics of Human Skin.* Journal of Investigative Dermatology, 1981. **77**(1): p. 13-19.

37. Cai, R., et al., *Induction of cytotoxicity by photoexcited TiO2 particles.* Cancer research, 1992. **52**(8): p. 2346-2348.

38. Zhang, H., et al., *Daunorubicin-TiO(2) nanocomposites as a "smart" pH-responsive drug delivery system.* International Journal of Nanomedicine, 2012. **7**: p. 235-242.

39. Gulati, K., et al., *Biocompatible polymer coating of titania nanotube arrays for improved drug elution and osteoblast adhesion.* Acta Biomaterialia, 2012. **8**(1): p. 449-456.

40. Tang, H., et al., *Electrical and optical properties of TiO2 anatase thin films.* Journal Of Applied Physics, 1994. **75**(4): p. 2042-2047.

41. Clydesdale, G.J., G.W. Dandie, and H.K. Muller, *Ultraviolet light induced injury: immunological and inflammatory effects.* Immunology and Cell Biology, 2001. **79**(6): p. 547-568.

42. Schmidt-Stein, F., et al., *X-ray induced photocatalysis on TiO2 and TiO2 nanotubes: Degradation of organics and drug release.* Electrochemistry Communications, 2009. **11**(11): p. 2077-2080.

43. Schmidt-Stein, F., et al., *X-ray induced photocatalysis on TiO 2 and TiO 2 nanotubes: degradation of organics and drug release.* Electrochemistry Communications, 2009. **11**(11): p. 2077-2080.

44. Kielbassa, C., L. Roza, and B. Epe, *Wavelength dependence of oxidative DNA damage induced by UV and visible light.* Carcinogenesis, 1997. **18**(4): p. 811-816.

45. Peidaee, P., et al., *The Cytotoxic Effects of Low Intensity Visible and Infrared Light on Human Breast Cancer (MCF7) cells.* Computational and Structural Biotechnology Journal, 2013. **6**: p. e201303015.

46. Enwemeka, C.S., *ATTENUATION AND PENETRATION OF VISIBLE 632.8nm AND INVISIBLE INFRA-RED 904nm LIGHT IN SOFT TISSUES.* LASER THERAPY, 2000. **13**(1): p. 95-101.

47. Ohno, T., et al., *Photocatalytic oxidation of water by visible light using ruthenium-doped titanium dioxide powder.* Journal of Photochemistry and Photobiology A: Chemistry, 1999. **127**(1–3): p. 107-110.

48. Wu, J.C.S. and C.-H. Chen, *A visible-light response vanadium-doped titania nanocatalyst by sol–gel method.* Journal of Photochemistry and Photobiology A: Chemistry, 2004. **163**(3): p. 509-515.

49. Yu, J., Q. Xiang, and M. Zhou, *Preparation, characterization and visible-light-driven photocatalytic activity of Fe-doped titania nanorods and first-principles study for electronic structures.* Applied Catalysis B: Environmental, 2009. **90**(3–4): p. 595-602.

50. Dong, F., et al., *Enhancement of the Visible Light Photocatalytic Activity of C-Doped TiO2 Nanomaterials Prepared by a Green Synthetic Approach.* The Journal of Physical Chemistry C, 2011. **115**(27): p. 13285-13292.

51. Sato, S., R. Nakamura, and S. Abe, *Visible-light sensitization of TiO2 photocatalysts by wet-method N doping.* Applied Catalysis A: General, 2005. **284**(1–2): p. 131-137.

52. Tang, X. and D. Li, *Sulfur-Doped Highly Ordered TiO2 Nanotubular Arrays with Visible Light Response.* The Journal of Physical Chemistry C, 2008. **112**(14): p. 5405-5409.

53. In, S., et al., *Effective Visible Light-Activated B-Doped and B,N-Codoped TiO2 Photocatalysts.* Journal of the American Chemical Society, 2007. **129**(45): p. 13790-13791.

54. Asahi, R., et al., *Visible-light photocatalysis in nitrogen-doped titanium oxides.* Science, 2001. **293**(5528): p. 269-271.

55. Jagadale, T.C., et al., *N-Doped TiO2 Nanoparticle Based Visible Light Photocatalyst by Modified Peroxide Sol−Gel Method.* The Journal of Physical Chemistry C, 2008. **112**(37): p. 14595-14602.

56. Grätzel, M., *Dye-sensitized solar cells.* Journal of Photochemistry and Photobiology C: Photochemistry Reviews, 2003. **4**(2): p. 145-153.

57. Abe, R., et al., *Steady hydrogen evolution from water on Eosin Y-fixed TiO 2 photocatalyst using a silane-coupling reagent under visible light irradiation.*

Journal of Photochemistry and Photobiology A: Chemistry, 2000. **137**(1): p. 63-69.

58. Wang, L., et al., *Rhodamine B-conjugated encrypted vipericidin nonapeptide is a potent toxin to zebrafish and associated with in vitro cytotoxicity.* Biochimica et Biophysica Acta (BBA) - General Subjects, 2015. **1850**(6): p. 1253-1260.

59. PERONE, V.B., *The natural occurrence and uses of toxic coumarins.* Microbial Toxins. Kadis, S., Ciegler, A., and Ajl, S. J.(Eds), 2016: p. 67-88.

60. Wachter, E., et al., *Light-activated ruthenium complexes photobind DNA and are cytotoxic in the photodynamic therapy window.* Chemical Communications, 2012. **48**(77): p. 9649-9651.

61. Nishijima, Y., et al., *Plasmon-assisted photocurrent generation from visible to near-infrared wavelength using a Au-nanorods/TiO2 electrode.* The Journal of Physical Chemistry Letters, 2010. **1**(13): p. 2031-2036.

62. Christopher, P., H. Xin, and S. Linic, *Visible-light-enhanced catalytic oxidation reactions on plasmonic silver nanostructures.* Nature chemistry, 2011. **3**(6): p. 467-472.

63. Hu, M., et al., *Gold nanostructures: engineering their plasmonic properties for biomedical applications.* Chemical Society Reviews, 2006. **35**(11): p. 1084-1094.

64. Yin, M., et al., *Upconverting Nanoparticles with a Mesoporous TiO2 Shell for Near-Infrared-Triggered Drug Delivery and Synergistic Targeted Cancer Therapy.* Chemistry – A European Journal, 2014. **20**(43): p. 14012-14017.

65. Arturo, A.A., et al., *Drug loading of nanoporous TiO 2 films.* Biomedical Materials, 2006. **1**(4): p. L11.

66. Peng, L., et al., *Long-Term Small Molecule and Protein Elution from TiO2 Nanotubes.* Nano Letters, 2009. **9**(5): p. 1932-1936.

67. Ma, M., et al., *Local delivery of antimicrobial peptides using self-organized TiO2 nanotube arrays for peri-implant infections.* Journal of biomedical materials research Part A, 2012. **100A**(2): p. 278-285.

68. Popat, K.C., et al., *Titania Nanotubes: A Novel Platform for Drug-Eluting Coatings for Medical Implants?* Small, 2007. **3**(11): p. 1878-1881.

69. Vincent, C., *Process for producing low-bulk density silica*. 1971, Google Patents.

70. Slowing, I.I., et al., *Mesoporous silica nanoparticles for drug delivery and biosensing applications.* Advanced Functional Materials, 2007. **17**(8): p. 1225-1236.

71. Slowing, I.I., et al., *Mesoporous silica nanoparticles as controlled release drug delivery and gene transfection carriers.* Advanced drug delivery reviews, 2008. **60**(11): p. 1278-1288.

72. Wu, C., et al., *Synthesis of Fe3O4@ SiO2@ polymer nanoparticles for controlled drug release.* Science China Chemistry, 2010. **53**(3): p. 514-518.

73. Jucker, B., et al., *Adsorption of bacterial surface polysaccharides on mineral oxides is mediated by hydrogen bonds.* Colloids and Surfaces B: Biointerfaces, 1997. **9**(6): p. 331-343.

74. Mellaerts, R., et al., *Physical State of Poorly Water Soluble Therapeutic Molecules Loaded into SBA-15 Ordered Mesoporous Silica Carriers: A Case Study with Itraconazole and Ibuprofen.* Langmuir, 2008. **24**(16): p. 8651-8659.

75. Manzano, M., et al., *Studies on MCM-41 mesoporous silica for drug delivery: Effect of particle morphology and amine functionalization.* Chemical Engineering Journal, 2008. **137**(1): p. 30-37.

76. Meng, H., et al., *Autonomous in vitro anticancer drug release from mesoporous silica nanoparticles by pH-sensitive nanovalves.* Journal of the American Chemical Society, 2010. **132**(36): p. 12690-12697.

77. Zhu, Y., et al., *Stimuli-responsive controlled drug release from a hollow mesoporous silica sphere/polyelectrolyte multilayer core–shell structure.* Angewandte Chemie, 2005. **117**(32): p. 5213-5217.

78. Liu, C., et al., *Magnetic mesoporous silica microspheres with thermo-sensitive polymer shell for controlled drug release.* Journal of Materials Chemistry, 2009. **19**(27): p. 4764-4770.

79. Nandiyanto, A.B.D., et al., *Synthesis of spherical mesoporous silica nanoparticles with nanometer-size controllable pores and outer diameters.* Microporous and Mesoporous Materials, 2009. **120**(3): p. 447-453.

80. Morel, A.-L., et al., *Sonochemical approach to the synthesis of Fe3O4@ SiO2 core− shell nanoparticles with tunable properties.* ACS nano, 2008. **2**(5): p. 847-856.

81. Selvan, S.T., T.T. Tan, and J.Y. Ying, *Robust, Non-Cytotoxic, Silica-Coated CdSe Quantum Dots with Efficient Photoluminescence.* Advanced Materials, 2005. **17**(13): p. 1620-1625.

82. Ung, T., L.M. Liz-Marzán, and P. Mulvaney, *Controlled method for silica coating of silver colloids. Influence of coating on the rate of chemical reactions.* Langmuir, 1998. **14**(14): p. 3740-3748.

83. Liz-Marzán, L.M., M. Giersig, and P. Mulvaney, *Synthesis of nanosized gold-silica core-shell particles*. Langmuir, 1996. **12**(18): p. 4329-4335.

84. Gerion, D., et al., *Synthesis and properties of biocompatible water-soluble silica-coated CdSe/ZnS semiconductor quantum dots.* The Journal of Physical Chemistry B, 2001. **105**(37): p. 8861-8871.

85. Bravo, J., et al., *Transparent superhydrophobic films based on silica nanoparticles.* Langmuir, 2007. **23**(13): p. 7293-7298.

86. Stöber, W., A. Fink, and E. Bohn, *Controlled growth of monodisperse silica spheres in the micron size range.* Journal of colloid and interface science, 1968. **26**(1): p. 62-69.

87. Nozawa, K., et al., *Smart control of monodisperse Stöber silica particles: effect of reactant addition rate on growth process.* Langmuir, 2005. **21**(4): p. 1516-1523.

88. Gao, J., H. Gu, and B. Xu, *Multifunctional magnetic nanoparticles: design, synthesis, and biomedical applications.* Accounts of Chemical Research, 2009. **42**(8): p. 1097-1107.

89. Huang, H., et al., *Remote control of ion channels and neurons through magnetic-field heating of nanoparticles.* Nature nanotechnology, 2010. **5**(8): p. 602-606.

90. Neuberger, T., et al., *Superparamagnetic nanoparticles for biomedical applications: possibilities and limitations of a new drug delivery system.* Journal of Magnetism and Magnetic Materials, 2005. **293**(1): p. 483-496.

91. Sensenig, R., et al., *Magnetic nanoparticle-based approaches to locally target therapy and enhance tissue regeneration in vivo.* Nanomedicine (London, England), 2012. **7**(9): p. 1425-1442.

92. Chertok, B., et al., *Iron oxide nanoparticles as a drug delivery vehicle for MRI monitored magnetic targeting of brain tumors.* Biomaterials, 2008. **29**(4): p. 487-496.

93. Li, L., et al., *Superparamagnetic iron oxide nanoparticles as MRI contrast agents for non-invasive stem cell labeling and tracking.* Theranostics, 2013. **3**(8): p. 595-615.

94. Brazel, C.S., *Magnetothermally-responsive nanomaterials: combining magnetic nanostructures and thermally-sensitive polymers for triggered drug release.* Pharmaceutical research, 2009. **26**(3): p. 644-656.

95. Laurent, S., et al., *Magnetic fluid hyperthermia: Focus on superparamagnetic iron oxide nanoparticles.* Advances in Colloid and Interface Science, 2011. **166**(1–2): p. 8-23.

96. Jain, T.K., et al., *Biodistribution, clearance, and biocompatibility of iron oxide magnetic nanoparticles in rats.* Molecular pharmaceutics, 2008. **5**(2): p. 316-327.

97. Liu, Z.-p., et al., *Complex-Surfactant-Assisted Hydrothermal Route to Ferromagnetic Nickel Nanobelts.* Advanced Materials, 2003. **15**(22): p. 1946-1948.

98. Reiss, B.D., et al., *Biological routes to metal alloy ferromagnetic nanostructures.* Nano Letters, 2004. **4**(6): p. 1127-1132.

99. Vold, M.J., *Van der Waals' attraction between anisometric particles.* Journal of Colloid Science, 1954. **9**(5): p. 451-459.

100. Zhang, H. and D. Wang, *Controlling the growth of charged-nanoparticle chains through interparticle electrostatic repulsion.* Angewandte Chemie, 2008. **120**(21): p. 4048-4051.

101. Kendall, K. and M.R. Kosseva, *Nanoparticle aggregation influenced by magnetic fields.* Colloids and Surfaces A: Physicochemical and Engineering Aspects, 2006. **286**(1–3): p. 112-116.

102. Verrecchia, T., et al., *Non-stealth (poly (lactic acid/albumin)) and stealth (poly (lactic acid-polyethylene glycol)) nanoparticles as injectable drug carriers.* Journal of Controlled Release, 1995. **36**(1): p. 49-61.

103. Schröder, U. and B.A. Sabel, *Nanoparticles, a drug carrier system to pass the blood-brain barrier, permit central analgesic effects of iv dalargin injections.* Brain research, 1996. **710**(1): p. 121-124.

104. Lu, F., et al., *Size Effect on Cell Uptake in Well-Suspended, Uniform Mesoporous Silica Nanoparticles.* Small, 2009. **5**(12): p. 1408-1413.

105. Charnay, C., et al., *Inclusion of ibuprofen in mesoporous templated silica: drug loading and release property.* European journal of pharmaceutics and biopharmaceutics, 2004. **57**(3): p. 533-540.

106. Radomski, A., et al., *Nanoparticle-induced platelet aggregation and vascular thrombosis.* British Journal of Pharmacology, 2005. **146**(6): p. 882-893.

107. Chen, Q. and Z.J. Zhang, *Size-dependent superparamagnetic properties of MgFe2O4 spinel ferrite nanocrystallites.* Applied Physics Letters, 1998. **73**: p. 3156.

108. Dunlop, D., *Superparamagnetic and single-domain threshold sizes in magnetite.* Journal of Geophysical Research, 1973. **78**(11): p. 1780-1793.

109. Mooney, K.E., J.A. Nelson, and M.J. Wagner, *Superparamagnetic cobalt ferrite nanocrystals synthesized by alkalide reduction.* Chemistry of Materials, 2004. **16**(16): p. 3155-3161.

110. Wahajuddin and S. Arora, *Superparamagnetic iron oxide nanoparticles: magnetic nanoplatforms as drug carriers.* International Journal of Nanomedicine, 2012. **7**: p. 3445-3471.

111. Yang, X., et al., *cRGD-functionalized, DOX-conjugated, and 64Cu-labeled superparamagnetic iron oxide nanoparticles for targeted anticancer drug delivery and PET/MR imaging.* Biomaterials, 2011. **32**(17): p. 4151-4160.

112. Laurent, S., et al., *Magnetic fluid hyperthermia: focus on superparamagnetic iron oxide nanoparticles.* Advances in Colloid and Interface Science, 2011. **166**(1): p. 8-23.

113. Hayashi, K., et al., *Superparamagnetic nanoparticle clusters for cancer theranostics combining magnetic resonance imaging and hyperthermia treatment.* Theranostics, 2013. **3**(6): p. 366-376.

114. Hu, S.-H., et al., *Core/Single-Crystal-Shell Nanospheres for Controlled Drug Release via a Magnetically Triggered Rupturing Mechanism.* Advanced Materials, 2008. **20**(14): p. 2690-2695.

115. Hu, M.J., B. Lin, and S.H. Yu, *Magnetic field-induced solvothermal synthesis of one-dimensional assemblies of Ni-Co alloy microstructures.* Nano research, 2008. **1**(4): p. 303-313.

116. Satarkar, N.S. and J.Z. Hilt, *Magnetic hydrogel nanocomposites for remote controlled pulsatile drug release.* Journal of Controlled Release, 2008. **130**(3): p. 246-251.

117. Sershen, S., et al., *Temperature-sensitive polymer–nanoshell composites for photothermally modulated drug delivery.* Journal of biomedical materials research, 2000. **51**(3): p. 293-298.

118. Yu, M.K., et al., *Drug-Loaded Superparamagnetic Iron Oxide Nanoparticles for Combined Cancer Imaging and Therapy In Vivo.* Angewandte Chemie International Edition, 2008. **47**(29): p. 5362-5365.

119. Kayal, S. and R. Ramanujan, *Doxorubicin loaded PVA coated iron oxide nanoparticles for targeted drug delivery.* Materials Science and Engineering: C, 2010. **30**(3): p. 484-490.

120. Jain, T.K., et al., *Iron Oxide Nanoparticles for Sustained Delivery of Anticancer Agents.* Molecular pharmaceutics, 2005. **2**(3): p. 194-205.

121. Quan, Q., et al., *HSA Coated Iron Oxide Nanoparticles as Drug Delivery Vehicles for Cancer Therapy.* Molecular pharmaceutics, 2011. **8**(5): p. 1669-1676.

122. Munnier, E., et al., *Novel method of doxorubicin–SPION reversible association for magnetic drug targeting.* International Journal of Pharmaceutics, 2008. **363**(1–2): p. 170-176.

123. Liu, D., et al., *Conjugation of paclitaxel to iron oxide nanoparticles for tumor imaging and therapy.* Nanoscale, 2012. **4**(7): p. 2306-2310.

124. Hwu, J.R., et al., *Targeted Paclitaxel by Conjugation to Iron Oxide and Gold Nanoparticles.* Journal of the American Chemical Society, 2009. **131**(1): p. 66-68.

125. Cho, H.-S., et al., *Fluorescent, Superparamagnetic Nanospheres for Drug Storage, Targeting, and Imaging: A Multifunctional Nanocarrier System for Cancer Diagnosis and Treatment.* ACS nano, 2010. **4**(9): p. 5398-5404.

126. Kievit, F.M., et al., *PEI–PEG–Chitosan-Copolymer-Coated Iron Oxide Nanoparticles for Safe Gene Delivery: Synthesis, Complexation, and Transfection.* Advanced Functional Materials, 2009. **19**(14): p. 2244-2251.

127. Oliveira, H., et al., *Magnetic field triggered drug release from polymersomes for cancer therapeutics.* Journal of Controlled Release, 2013. **169**(3): p. 165-170.

128. Derfus, A.M., et al., *Remotely Triggered Release from Magnetic Nanoparticles.* Advanced Materials, 2007. **19**(22): p. 3932-3936.

129. Hayashi, K., et al., *High-Frequency, Magnetic-Field-Responsive Drug Release from Magnetic Nanoparticle/Organic Hybrid Based on Hyperthermic Effect.* ACS Applied Materials & Interfaces, 2010. **2**(7): p. 1903-1911.

130. Che Rose, L., et al., *A SPION-eicosane protective coating for water soluble capsules: Evidence for on-demand drug release triggered by magnetic hyperthermia.* Scientific Reports, 2016. **6**: p. 20271.

131. Upadhyay, D., et al., *Magnetised Thermo Responsive Lipid Vehicles for Targeted and Controlled Lung Drug Delivery.* Pharmaceutical research, 2012. **29**(9): p. 2456-2467.

132. Park, H., et al., *Inactivation of Pseudomonas aeruginosa PA01 biofilms by hyperthermia using superparamagnetic nanoparticles.* Journal of Microbiological Methods, 2011. **84**(1): p. 41-45.

133. Le Renard, P.-E., et al., *Magnetic and in vitro heating properties of implants formed in situ from injectable formulations and containing superparamagnetic iron oxide nanoparticles (SPIONs) embedded in silica microparticles for magnetically induced local hyperthermia.* Journal of Magnetism and Magnetic Materials, 2011. **323**(8): p. 1054-1063.

134. Le Renard, P.-E., et al., *The in vivo performance of magnetic particle-loaded injectable, in situ gelling, carriers for the delivery of local hyperthermia.* Biomaterials, 2010. **31**(4): p. 691-705.

135. Sonvico, F., et al., *Folate-Conjugated Iron Oxide Nanoparticles for Solid Tumor Targeting as Potential Specific Magnetic Hyperthermia Mediators: Synthesis, Physicochemical Characterization, and in Vitro Experiments.* Bioconjugate chemistry, 2005. **16**(5): p. 1181-1188.

136. Guardia, P., et al., *Water-Soluble Iron Oxide Nanocubes with High Values of Specific Absorption Rate for Cancer Cell Hyperthermia Treatment.* ACS nano, 2012. **6**(4): p. 3080-3091.

137. Thomas, R.G., et al., *Hyaluronic acid conjugated superparamagnetic iron oxide nanoparticle for cancer diagnosis and hyperthermia therapy.* Carbohydrate Polymers, 2015. **131**: p. 439-446.

138. Alphandéry, E., et al., *Chains of Magnetosomes Extracted from AMB-1 Magnetotactic Bacteria for Application in Alternative Magnetic Field Cancer Therapy.* ACS nano, 2011. **5**(8): p. 6279-6296.

139. Ma, X., et al., *Exploring a new SPION-based MRI contrast agent with excellent water-dispersibility, high specificity to cancer cells and strong MR imaging efficacy.* Colloids and Surfaces B: Biointerfaces, 2015. **126**: p. 44-49.

140. Andreas, K., et al., *Highly efficient magnetic stem cell labeling with citrate-coated superparamagnetic iron oxide nanoparticles for MRI tracking.* Biomaterials, 2012. **33**(18): p. 4515-4525.

141. Lee, Y.T., K. Woo, and K.S. Choi, *Preparation of Water-Dispersible and Biocompatible Iron Oxide Nanoparticles for MRI Agent.* IEEE Transactions on Nanotechnology, 2008. **7**(2): p. 111-114.

142. Yang, X., et al., *Tumor-targeting, superparamagnetic polymeric vesicles as highly efficient MRI contrast probes.* Journal of Materials Chemistry, 2009. **19**(32): p. 5812-5817.

143. Jae-Ho, L., et al., *Enhanced stem cell tracking via electrostatically assembled fluorescent SPION–peptide complexes.* Nanotechnology, 2009. **20**(35): p. 355102.

144. Kim, H., et al., *A highly sensitive magnetite nanoparticle as a simple and rapid stem cell labelling agent for MRI tracking.* Journal of Materials Chemistry, 2011. **21**(21): p. 7742-7747.

145. Liu, C.H., et al., *Noninvasive delivery of gene targeting probes to live brains for transcription MRI.* The FASEB Journal, 2008. **22**(4): p. 1193-1203.

146. Vu-Quang, H., et al., *Carboxylic mannan-coated iron oxide nanoparticles targeted to immune cells for lymph node-specific MRI in vivo.* Carbohydrate Polymers, 2012. **88**(2): p. 780-788.

147. Lu, X., H. Mao, and W. Zhang, *Fabrication of core-shell Fe3O4/polypyrrole and hollow polypyrrole microspheres.* Polymer Composites, 2009. **30**(6): p. 847-854.

148. Chen, A., et al., *The preparation of polypyrrole–Fe3O4 nanocomposites by the use of common ion effect.* Synthetic metals, 2003. **139**(2): p. 411-415.

149. Tian, Q., et al., *Multifunctional Polypyrrole@Fe3O4 Nanoparticles for Dual-Modal Imaging and In Vivo Photothermal Cancer Therapy.* Small, 2014. **10**(6): p. 1063-1068.

150. Wuang, S.C., et al., *Synthesis and functionalization of polypyrrole-Fe 3 O 4 nanoparticles for applications in biomedicine.* Journal of Materials Chemistry, 2007. **17**(31): p. 3354-3362.

151. Fujiwara, M., et al., *On the Movement of Paramagnetic Ions in an Inhomogeneous Magnetic Field.* The Journal of Physical Chemistry B, 2004. **108**(11): p. 3531-3534.

152. Alphandéry, E., *Applications of Magnetosomes Synthesized by Magnetotactic Bacteria in Medicine.* Frontiers in Bioengineering and Biotechnology, 2014. **2**(5).

153. Sun, J.-B., et al., *In vitro and in vivo antitumor effects of doxorubicin loaded with bacterial magnetosomes (DBMs) on H22 cells: The magnetic bio-nanoparticles as drug carriers.* Cancer Letters, 2007. **258**(1): p. 109-117.

154. Wang, J., et al., *Magnetic-Field-Induced Growth of Single-Crystalline Fe3O4 Nanowires.* Advanced Materials, 2004. **16**(2): p. 137-140.

155. Abu-Much, R. and A. Gedanken, *Sonochemical Synthesis under a Magnetic Field: Structuring Magnetite Nanoparticles and the Destabilization of a Colloidal Magnetic Aqueous Solution under a Magnetic Field.* The Journal of Physical Chemistry C, 2008. **112**(1): p. 35-42.

156. Pol, S.V., et al., *External Magnetic Field-Induced Mesoscopic Organization of Fe3O4 Pyramids and Carbon Sheets.* Inorganic chemistry, 2007. **46**(12): p. 4951-4959.

157. Athanassiou, E., et al., *Template free, large scale synthesis of cobalt nanowires using magnetic fields for alignment.* Nanotechnology, 2007. **18**(16): p. 165606.

158. Chong, W.H., et al., *Stirring in Suspension: Nanometer-Sized Magnetic Stir Bars.* Angewandte Chemie International Edition, 2013. **52**(33): p. 8570-8573.

159. He, Z., et al., *Magnetic-Field-Induced Phase-Selective Synthesis of Ferrosulfide Microrods by a Hydrothermal Process: Microstructure Control and Magnetic Properties.* Advanced Functional Materials, 2006. **16**(8): p. 1105-1111.

160. Wang, M., et al., *Assembly of non-crystalline cobalt particles into crystalline tricobalt tetroxide nanowires under an external magnetic field.* CrystEngComm, 2010. **12**(10): p. 3262-3266.

161. Attan, N., et al., *Well-aligned titanium dioxide with very high length-to-diameter ratio synthesized under magnetic field.* Chemistry Letters, 2012. **41**(11): p. 1468-1470.

162. Xu, Y., et al., *Magnetic-field-assisted solvothermal growth of single-crystalline bismuth nanowires.* Nanotechnology, 2008. **19**(11): p. 115602.

163. Liu, Y., et al., *Magnetic-field induced formation of 1D Fe 3 O 4/C/CdS coaxial nanochains as highly efficient and reusable photocatalysts for water treatment.* Journal of Materials Chemistry, 2011. **21**(45): p. 18359-18364.

164. Li, P., et al., *Thermodynamic phase formation of morphology and size controlled Ni nanochains by temperature and magnetic field.* The Journal of Physical Chemistry C, 2010. **114**(17): p. 7721-7726.

165. Ho, D., et al., *Magnetic field directed fabrication of conducting polymer nanowires.* Chemical Communications, 2013. **49**(64): p. 7138-7140.

166. Bharti, B., et al., *Nanocapillarity-mediated magnetic assembly of nanoparticles into ultraflexible filaments and reconfigurable networks.* Nat Mater, 2015. **14**(11): p. 1104-1109.

167. Kim, J.S., et al., *In Situ Magnetic Field-Assisted Low Temperature Atmospheric Growth of GaN Nanowires via the Vapor–Liquid–Solid Mechanism.* ACS Applied Materials & Interfaces, 2013. **6**(1): p. 116-121.

168. Volotskova, O., et al., *Tailored distribution of single-wall carbon nanotubes from arc plasma synthesis using magnetic fields.* ACS nano, 2010. **4**(9): p. 5187-5192.

169. Bharti, B., A.-L. Fameau, and O.D. Velev, *Magnetophoretic assembly of flexible nanoparticles/lipid microfilaments.* Faraday Discussions, 2015. **181**(0): p. 437-448.

170. Lam, S.J., et al., *Combating multidrug-resistant Gram-negative bacteria with structurally nanoengineered antimicrobial peptide polymers.* Nature Microbiology, 2016. **1**: p. 16162.

171. Mädler, L., et al., *Controlled synthesis of nanostructured particles by flame spray pyrolysis.* Journal of Aerosol Science, 2002. **33**(2): p. 369-389.

172. Mueller, R., L. Mädler, and S.E. Pratsinis, *Nanoparticle synthesis at high production rates by flame spray pyrolysis.* Chemical Engineering Science, 2003. **58**(10): p. 1969-1976.

173. Pawinrat, P., O. Mekasuwandumrong, and J. Panpranot, *Synthesis of Au–ZnO and Pt–ZnO nanocomposites by one-step flame spray pyrolysis and its application for photocatalytic degradation of dyes.* Catalysis Communications, 2009. **10**(10): p. 1380-1385.

174. Chiarello, G.L., E. Selli, and L. Forni, *Photocatalytic hydrogen production over flame spray pyrolysis-synthesised TiO 2 and Au/TiO 2.* Applied Catalysis B: Environmental, 2008. **84**(1): p. 332-339.

175. Mädler, L., et al., *Direct formation of highly porous gas-sensing films by in situ thermophoretic deposition of flame-made Pt/SnO 2 nanoparticles.* Sensors and Actuators B: Chemical, 2006. **114**(1): p. 283-295.

176. Teoh, W.Y., et al., *Direct (one-step) synthesis of and nanoparticles for photocatalytic mineralisation of sucrose.* Chemical Engineering Science, 2005. **60**(21): p. 5852-5861.

177. Strobel, R. and S.E. Pratsinis, *Direct synthesis of maghemite, magnetite and wustite nanoparticles by flame spray pyrolysis.* Advanced Powder Technology, 2009. **20**(2): p. 190-194.

178. Teleki, A., et al., *Distinguishing between aggregates and agglomerates of flame-made TiO2 by high-pressure dispersion.* Powder Technology, 2008. **181**(3): p. 292-300.

179. Kho, Y.K., et al., *Photocatalytic H2 Evolution over TiO2 Nanoparticles. The Synergistic Effect of Anatase and Rutile.* The Journal of Physical Chemistry C, 2010. **114**(6): p. 2821-2829.

180. Trommer, R.M. and C.P. Bergmann, *Flame Spray Technology*. 2015: Springer.

181. Tricoli, A., et al., *Scalable flame synthesis of SiO2 nanowires: dynamics of growth.* Nanotechnology, 2010. **21**(46): p. 465604.

182. Lasseter, T.L., et al., *Covalently modified silicon and diamond surfaces: resistance to nonspecific protein adsorption and optimization for biosensing.* Journal of the American Chemical Society, 2004. **126**(33): p. 10220-10221.

183. Petrie, T.A., et al., *Multivalent integrin-specific ligands enhance tissue healing and biomaterial integration.* Science translational medicine, 2010. **2**(45): p. 45ra60-45ra60.

184. Lu, H., et al., *Synthesis and characterization of multi-functional nanoparticles possessing magnetic, up-conversion fluorescence and bio-affinity properties.* Journal of Materials Chemistry, 2004. **14**(8): p. 1336-1341.

185. Yang, P., S. Gai, and J. Lin, *Functionalized mesoporous silica materials for controlled drug delivery.* Chemical Society Reviews, 2012. **41**(9): p. 3679-3698.

186. Liu, S. and M. Han, *Synthesis, functionalization, and bioconjugation of monodisperse, Silica-Coated gold nanoparticles: Robust bioprobes.* Advanced Functional Materials, 2005. **15**(6): p. 961-967.

187. Li, S.-C., et al., *Hydrogen bonding controls the dynamics of catechol adsorbed on a TiO2 (110) surface.* Science, 2010. **328**(5980): p. 882-884.

188. Roddick-Lanzilotta, A.D., P.A. Connor, and A.J. McQuillan, *An In Situ Infrared Spectroscopic Study of the Adsorption of Lysine to TiO2 from an Aqueous Solution.* Langmuir, 1998. **14**(22): p. 6479-6484.

189. Liu, J.-F., Z.-s. Zhao, and G.-b. Jiang, *Coating Fe3O4 magnetic nanoparticles with humic acid for high efficient removal of heavy metals in water.* Environmental science & technology, 2008. **42**(18): p. 6949-6954.

190. Zeng, T., et al., *Fe3O4 nanoparticles: a robust and magnetically recoverable catalyst for three-component coupling of aldehyde, alkyne and amine.* Green Chemistry, 2010. **12**(4): p. 570-573.

191. Sahoo, B., S.K. Sahu, and P. Pramanik, *A novel method for the immobilization of urease on phosphonate grafted iron oxide nanoparticle.* Journal of Molecular Catalysis B: Enzymatic, 2011. **69**(3): p. 95-102.

192. Ahangaran, F., A. Hassanzadeh, and S. Nouri, *Surface modification of Fe3O4@ SiO2 microsphere by silane coupling agent.* International Nano Letters, 2013. **3**(1): p. 1-5.

193. Cai, K., et al., *Surface functionalized titanium thin films: Zeta-potential, protein adsorption and cell proliferation.* Colloids and Surfaces B: Biointerfaces, 2006. **50**(1): p. 1-8.

194. Milanesi, F., et al., *Siloxane− TiO2 Hybrid Nanocomposites. The Structure of the Hydrophobic Layer.* The Journal of Physical Chemistry C, 2010. **114**(18): p. 8287-8293.

195. Ramanathan, T., et al., *Amino-Functionalized Carbon Nanotubes for Binding to Polymers and Biological Systems.* Chemistry of Materials, 2005. **17**(6): p. 1290-1295.

196. Goodman, C.M., et al., *DNA-binding by Functionalized Gold Nanoparticles: Mechanism and Structural Requirements.* Chemical Biology & Drug Design, 2006. **67**(4): p. 297-304.

197. Sperling, R.A. and W. Parak, *Surface modification, functionalization and bioconjugation of colloidal inorganic nanoparticles.* Philosophical Transactions of the Royal Society of London A: Mathematical, Physical and Engineering Sciences, 2010. **368**(1915): p. 1333-1383.

198. Sperling, R.A. and W.J. Parak, *Surface modification, functionalization and bioconjugation of colloidal inorganic nanoparticles.* Philosophical Transactions of the Royal Society A: Mathematical, Physical and Engineering Sciences, 2010. **368**(1915): p. 1333-1383.

199. Luschtinetz, R., et al., *Adsorption of phosphonic acid at the TiO2 anatase (101) and rutile (110) surfaces.* The Journal of Physical Chemistry C, 2009. **113**(14): p. 5730-5740.

200. Mutin, P.H., G. Guerrero, and A. Vioux, *Hybrid materials from organophosphorus coupling molecules.* Journal of Materials Chemistry, 2005. **15**(35-36): p. 3761-3768.

201. Neouze, M.-A. and U. Schubert, *Surface modification and functionalization of metal and metal oxide nanoparticles by organic ligands.* Monatshefte für Chemie-Chemical Monthly, 2008. **139**(3): p. 183-195.

202. del Campo, A., et al., *Multifunctional magnetite and silica–magnetite nanoparticles: synthesis, surface activation and applications in life sciences.* Journal of Magnetism and Magnetic Materials, 2005. **293**(1): p. 33-40.

203. Pere, E., et al., *Low-temperature reaction of trialkoxysilanes on silica gel: a mild and controlled method for modifying silica surfaces.* Journal of colloid and interface science, 2005. **281**(2): p. 410-416.

204. Balasundaram, G., C. Yao, and T.J. Webster, *TiO2 nanotubes functionalized with regions of bone morphogenetic protein-2 increases osteoblast adhesion.* Journal of biomedical materials research Part A, 2008. **84**(2): p. 447-453.

205. Kang, J.-S., C. Yu, and F.-A. Zhang, *Effect of silane modified SiO2 particles on poly (MMA-HEMA) soap-free emulsion polymerization.* Iran Polym J, 2009. **18**(22): p. 927-935.

206. Sodipo, B.K. and A.A. Aziz, *A sonochemical approach to the direct surface functionalization of superparamagnetic iron oxide nanoparticles with (3-aminopropyl) triethoxysilane.* Beilstein Journal of Nanotechnology, 2014. **5**(1): p. 1472-1476.

207. Zhang, L., R. He, and H.-C. Gu, *Oleic acid coating on the monodisperse magnetite nanoparticles.* Applied Surface Science, 2006. **253**(5): p. 2611-2617.

208. Qu, Q., et al., *Chemically Binding Carboxylic Acids onto TiO2 Nanoparticles with Adjustable Coverage by Solvothermal Strategy.* Langmuir, 2010. **26**(12): p. 9539-9546.

209. Viota, J.L., et al., *Electrokinetic characterization of magnetite nanoparticles functionalized with amino acids.* Journal of colloid and interface science, 2010. **344**(1): p. 144-149.

210. Ghosh, P.S., et al., *Efficient Gene Delivery Vectors by Tuning the Surface Charge Density of Amino Acid-Functionalized Gold Nanoparticles.* ACS nano, 2008. **2**(11): p. 2213-2218.

211. Thomas, A.G. and K.L. Syres, *Adsorption of organic molecules on rutile TiO 2 and anatase TiO 2 single crystal surfaces.* Chemical Society Reviews, 2012. **41**(11): p. 4207-4217.

212. Roddick-Lanzilotta, A.D. and A.J. McQuillan, *An in situ Infrared Spectroscopic Study of Glutamic Acid and of Aspartic Acid Adsorbed on TiO2: Implications for the Biocompatibility of Titanium.* Journal of colloid and interface science, 2000. **227**(1): p. 48-54.

213. Schmidt, M. and S.G. Steinemann, *XPS studies of amino acids adsorbed on titanium dioxide surfaces.* Fresenius' Journal of Analytical Chemistry, 1991. **341**(5): p. 412-415.

214. Albanese, A., P.S. Tang, and W.C. Chan, *The effect of nanoparticle size, shape, and surface chemistry on biological systems.* Annual review of biomedical engineering, 2012. **14**: p. 1-16.

215. Jiang, J., G. Oberdörster, and P. Biswas, *Characterization of size, surface charge, and agglomeration state of nanoparticle dispersions for toxicological studies.* Journal of Nanoparticle Research, 2009. **11**(1): p. 77-89.

216. Schmidt, M., *X-ray photoelectron spectroscopy studies on adsorption of amino acids from aqueous solutions onto oxidised titanium surfaces.* Archives of Orthopaedic and Trauma Surgery, 2001. **121**(7): p. 403-410.

217. Ojamäe, L., et al., *IR and quantum-chemical studies of carboxylic acid and glycine adsorption on rutile TiO2 nanoparticles.* Journal of colloid and interface science, 2006. **296**(1): p. 71-78.

218. Tran, T.H., A.Y. Nosaka, and Y. Nosaka, *Adsorption and photocatalytic decomposition of amino acids in TiO2 photocatalytic systems.* The Journal of Physical Chemistry B, 2006. **110**(50): p. 25525-25531.

219. Sousa, M.H., et al., *Biocompatible magnetic fluid precursors based on aspartic and glutamic acid modified maghemite nanostructures.* Journal of Magnetism and Magnetic Materials, 2001. **225**(1–2): p. 67-72.

220. Vieira, A.P., et al., *Adsorption of cysteine on hematite, magnetite and ferrihydrite: FT-IR, Mössbauer, EPR spectroscopy and X-ray diffractometry studies.* Amino Acids, 2011. **40**(1): p. 205-214.

221. Bürger, A., U. Magdans, and H. Gies, *Adsorption of amino acids on the magnetite-(111)-surface: a force field study.* Journal of Molecular Modeling, 2013. **19**(2): p. 851-857.

222. Park, J.Y., et al., *Colloidal stability of amino acid coated magnetite nanoparticles in physiological fluid.* materials letters, 2009. **63**(3–4): p. 379-381.

223. Pušnik, K., et al., *Adsorption of Amino Acids, Aspartic Acid and Lysine onto Iron-Oxide Nanoparticles.* The Journal of Physical Chemistry C, 2016.

224. Schwaminger, S.P., et al., *Nature of Interactions of Amino Acids with Bare Magnetite Nanoparticles.* The Journal of Physical Chemistry C, 2015. **119**(40): p. 23032-23041.

225. Auroux, A. and A. Gervasini, *Microcalorimetric study of the acidity and basicity of metal oxide surfaces.* The Journal of Physical Chemistry, 1990. **94**(16): p. 6371-6379.

226. Kosmulski, M., *Compilation of PZC and IEP of sparingly soluble metal oxides and hydroxides from literature.* Advances in Colloid and Interface Science, 2009. **152**(1–2): p. 14-25.

227. Peng, Z.G., K. Hidajat, and M.S. Uddin, *Adsorption of bovine serum albumin on nanosized magnetic particles.* Journal of colloid and interface science, 2004. **271**(2): p. 277-283.

228. Huang, S.-H. and D.-H. Chen, *Rapid removal of heavy metal cations and anions from aqueous solutions by an amino-functionalized magnetic nano-adsorbent.* Journal of hazardous materials, 2009. **163**(1): p. 174-179.

229. Ziyang, L., et al., *Monodisperse magnetizable silica composite particles from heteroaggregate of carboxylic polystyrene latex and Fe 3 O 4 nanoparticles.* Nanotechnology, 2008. **19**(5): p. 055602.

230. Banerjee, S.S. and D.-H. Chen, *Fast removal of copper ions by gum arabic modified magnetic nano-adsorbent.* Journal of hazardous materials, 2007. **147**(3): p. 792-799.

231. Kosmulski, M., J. Gustafsson, and J.B. Rosenholm, *Correlation between the Zeta Potential and Rheological Properties of Anatase Dispersions.* Journal of colloid and interface science, 1999. **209**(1): p. 200-206.

232. Mandzy, N., E. Grulke, and T. Druffel, *Breakage of TiO2 agglomerates in electrostatically stabilized aqueous dispersions.* Powder Technology, 2005. **160**(2): p. 121-126.

233. Fazio, S., et al., *Colloidal stability of nanosized titania aqueous suspensions.* Journal of the European Ceramic Society, 2008. **28**(11): p. 2171-2176.

234. Penn, R.L. and J.F. Banfield, *Morphology development and crystal growth in nanocrystalline aggregates under hydrothermal conditions: insights from titania.* Geochimica et Cosmochimica Acta, 1999. **63**(10): p. 1549-1557.

235. Jonsson, C.M., et al., *Adsorption of l-aspartate to rutile (α-TiO2): Experimental and theoretical surface complexation studies.* Geochimica et Cosmochimica Acta, 2010. **74**(8): p. 2356-2367.

236. Jonsson, C.M., et al., *Attachment of l-Glutamate to Rutile (α-TiO2): A Potentiometric, Adsorption, and Surface Complexation Study.* Langmuir, 2009. **25**(20): p. 12127-12135.

237. MacDiarmid, A.G., *Synthetic metals: a novel role for organic polymers.* Synthetic metals, 2001. **125**(1): p. 11-22.

238. Svirskis, D., et al., *Electrochemically controlled drug delivery based on intrinsically conducting polymers.* Journal of Controlled Release, 2010. **146**(1): p. 6-15.

239. Bredas, J., et al., *Polarons and bipolarons in polypyrrole: Evolution of the band structure and optical spectrum upon doing.* Physical Review B, 1984. **30**(2): p. 1023.

240. Zha, Z., et al., *Uniform polypyrrole nanoparticles with high photothermal conversion efficiency for photothermal ablation of cancer cells.* Advanced Materials, 2013. **25**(5): p. 777-782.

241. Zhang, H., et al., *Controlled-Release System of Small Molecules Triggered by the Photothermal Effect of Polypyrrole.* Macromolecular rapid communications, 2016. **37**(2): p. 149-154.

242. Wang, X., et al., *Evaluation of biocompatibility of polypyrrole in vitro and in vivo.* Journal of biomedical materials research Part A, 2004. **68**(3): p. 411-422.

243. Liu, Y.-C. and B.-J. Hwang, *Mechanism of conductivity decay of polypyrrole exposed to water and enhancement of conductivity stability of copper (I)-modified polypyrrole.* Journal of Electroanalytical Chemistry, 2001. **501**(1): p. 100-106.

244. Huang, W.-S., B.D. Humphrey, and A.G. MacDiarmid, *Polyaniline, a novel conducting polymer. Morphology and chemistry of its oxidation and reduction in aqueous electrolytes.* Journal of the Chemical Society, Faraday Transactions 1: Physical Chemistry in Condensed Phases, 1986. **82**(8): p. 2385-2400.

245. Snook, G.A., P. Kao, and A.S. Best, *Conducting-polymer-based supercapacitor devices and electrodes.* Journal of Power Sources, 2011. **196**(1): p. 1-12.

246. Somboonsub, B., et al., *Comparison of the thermally stable conducting polymers PEDOT, PANi, and PPy using sulfonated poly(imide) templates.* Polymer, 2010. **51**(20): p. 4472-4476.

247. Guo, Z., et al., *Fabrication and characterization of iron oxide nanoparticles filled polypyrrole nanocomposites.* Journal of Nanoparticle Research, 2009. **11**(6): p. 1441-1452.

248. Thiéblemont, J., J. Gabelle, and M. Planche, *Polypyrrole overoxidation during its chemical synthesis.* Synthetic metals, 1994. **66**(3): p. 243-247.

249. Lee, J., et al., *Synthesis and characterization of soluble polypyrrole.* Synthetic metals, 1997. **84**(1): p. 137-140.

250. Armes, S.P., *Optimum reaction conditions for the polymerization of pyrrole by iron (III) chloride in aqueous solution.* Synthetic metals, 1987. **20**(3): p. 365-371.

251. Kanazawa, K.K., et al., *Polypyrrole: an electrochemically synthesized conducting organic polymer.* Synthetic metals, 1980. **1**(3): p. 329-336.

252. Kumar, A.M. and N. Rajendran, *Electrochemical aspects and in vitro biocompatibility of polypyrrole/TiO 2 ceramic nanocomposite coatings on 316L SS for orthopedic implants.* Ceramics International, 2013. **39**(5): p. 5639-5650.

253. Bredas, J.L. and G.B. Street, *Polarons, bipolarons, and solitons in conducting polymers.* Accounts of Chemical Research, 1985. **18**(10): p. 309-315.

254. Brédas, J.L., et al., *Polarons and bipolarons in polypyrrole: Evolution of the band structure and optical spectrum upon doing.* Physical Review B, 1984. **30**(2): p. 1023-1025.

255. Yakushi, K., et al., *Optical study of polypyrrole perchlorate.* The Journal of Chemical Physics, 1983. **79**(10): p. 4774-4778.

256. Pugh, S. and D. Bloor, *The use of short chain oligomers as a model for soluble polypyrrole.* Synthetic metals, 1989. **28**(1): p. 187-192.

257. Guyard, L., P. Hapiot, and P. Neta, *Redox chemistry of bipyrroles: Further insights into the oxidative polymerization mechanism of pyrrole and oligopyrroles.* The Journal of Physical Chemistry B, 1997. **101**(29): p. 5698-5706.

258. Fink, J., et al., *Electronic structure of pyrrole-based conducting polymers: An electron-energy-loss-spectroscopy study.* Physical Review B, 1986. **34**(2): p. 1101.

259. George, P.M., et al., *Electrically Controlled Drug Delivery from Biotin-Doped Conductive Polypyrrole.* Advanced Materials, 2006. **18**(5): p. 577-581.

260. Sirinrath, S., P. Rajesh, and J.W. Thomas, *Electrically controlled drug release from nanostructured polypyrrole coated on titanium.* Nanotechnology, 2011. **22**(8): p. 085101.

261. Thompson, B.C., et al., *Effect of the dopant anion in polypyrrole on nerve growth and release of a neurotrophic protein.* Biomaterials, 2011. **32**(15): p. 3822-3831.

262. Sharma, M., et al., *High surface area polypyrrole scaffolds for tunable drug delivery.* International Journal of Pharmaceutics, 2013. **443**(1): p. 163-168.

263. Gomez, N. and C.E. Schmidt, *Nerve growth factor-immobilized polypyrrole: Bioactive electrically conducting polymer for enhanced neurite extension.* Journal of biomedical materials research Part A, 2007. **81**(1): p. 135-149.

264. Richardson, R.T., et al., *The effect of polypyrrole with incorporated neurotrophin-3 on the promotion of neurite outgrowth from auditory neurons.* Biomaterials, 2007. **28**(3): p. 513-523.

265. John, R. and G.G. Wallace, *Doping-dedoping of polypyrrole: a study using current-measuring and resistance-measuring techniques.* Journal of Electroanalytical Chemistry, 1993. **354**(1): p. 145-160.

266. Ge, J., et al., *Drug Release from Electric-Field-Responsive Nanoparticles.* ACS nano, 2012. **6**(1): p. 227-233.

267. Jiang, H., et al., *Conjugation of methotrexate onto dedoped Fe3O4/PPy nanospheres to produce magnetic targeting drug with controlled drug release and targeting specificity for HeLa cells.* Synthetic metals, 2015. **207**: p. 18-25.

268. Attia, M.F., et al., *One-step synthesis of iron oxide polypyrrole nanoparticles encapsulating ketoprofen as model of hydrophobic drug.* International Journal of Pharmaceutics, 2016. **508**(1–2): p. 61-70.

269. Wang, C., et al., *Iron oxide@ polypyrrole nanoparticles as a multifunctional drug carrier for remotely controlled cancer therapy with synergistic antitumor effect.* ACS nano, 2013. **7**(8): p. 6782-6795.

270. Meteleva-Fischer, Y.V., E. Von Hauff, and J. Parisi, *Electrochemical synthesis of polypyrrole layers doped with glutamic ions.* Journal of Applied Polymer Science, 2009. **114**(6): p. 4051-4058.

271. Valencia Castro, L.E., et al., *Chemical polymerization of pyrrole in the presence of l-serine or l-glutamic acid: Electrically controlled amoxicillin release from composite hydrogel.* Journal of Applied Polymer Science, 2015. **132**(15).

272. Zha, Z., et al., *Polypyrrole Hollow Microspheres as Echogenic Photothermal Agent for Ultrasound Imaging Guided Tumor Ablation.* Scientific Reports, 2013. **3**: p. 2360.

273. Jin, Y., et al., *Encapsulating tantalum oxide into polypyrrole nanoparticles for X-ray CT/photoacoustic bimodal imaging-guided photothermal ablation of cancer.* Biomaterials, 2014. **35**(22): p. 5795-5804.

274. Zhang, M., et al., *Near-Infrared Light and pH-Responsive Polypyrrole@Polyacrylic acid/Fluorescent Mesoporous Silica Nanoparticles for Imaging and Chemo-Photothermal Cancer Therapy.* Chemistry – A European Journal, 2015. **21**(45): p. 16162-16171.

275. Yang, K., et al., *In Vitro and In Vivo Near-Infrared Photothermal Therapy of Cancer Using Polypyrrole Organic Nanoparticles.* Advanced Materials, 2012. **24**(41): p. 5586-5592.

276. Chen, R., et al., *Polypyrrole confined in dendrimer-like silica nanoparticles for combined photothermal and chemotherapy of cancer.* RSC Advances, 2016. **6**(45): p. 38931-38942.

277. Luo, R.-C., et al., *Near-infrared photothermal activation of microgels incorporating polypyrrole nanotransducers through droplet microfluidics.* Chemical Communications, 2013. **49**(72): p. 7887-7889.

278. Chiang, W.-L., et al., *A rapid drug release system with a NIR light-activated molecular switch for dual-modality photothermal/antibiotic treatments of subcutaneous abscesses.* Journal of Controlled Release, 2015. **199**: p. 53-62.

279. Wang, J., et al., *The preparation, drug loading and in vitro NIR photothermal-controlled release behavior of raspberry-like hollow polypyrrole microspheres.* Journal of Materials Chemistry B, 2015. **3**(47): p. 9186-9193.

280. Seyfoddin, A., et al., *Electro-responsive macroporous polypyrrole scaffolds for triggered dexamethasone delivery.* European journal of pharmaceutics and biopharmaceutics, 2015. **94**: p. 419-426.

281. Li, Y., K. Neoh, and E. Kang, *Controlled release of heparin from polypyrrole-poly (vinyl alcohol) assembly by electrical stimulation.* Journal of biomedical materials research Part A, 2005. **73**(2): p. 171-181.

282. Thompson, B.C., et al., *Optimising the incorporation and release of a neurotrophic factor using conducting polypyrrole.* Journal of Controlled Release, 2006. **116**(3): p. 285-294.

283. Valencia Castro, L.E., et al., *Chemical polymerization of pyrrole in the presence of l-serine or l-glutamic acid: Electrically controlled amoxicillin release from composite hydrogel.* Journal of Applied Polymer Science, 2015. **132**(15): p. n/a-n/a.

284. Samanta, D., J.L. Meiser, and R.N. Zare, *Polypyrrole nanoparticles for tunable, pH-sensitive and sustained drug release.* Nanoscale, 2015. **7**(21): p. 9497-9504.

285. Chouly, C., et al., *Development of superparamagnetic nanoparticles for MRI: effect of particle size, charge and surface nature on biodistribution.* Journal of microencapsulation, 1996. **13**(3): p. 245-255.

286. Hong, R., et al., *Glutathione-mediated delivery and release using monolayer protected nanoparticle carriers.* Journal of the American Chemical Society, 2006. **128**(4): p. 1078-1079.

287. Brunner, T.J., et al., *In vitro cytotoxicity of oxide nanoparticles: comparison to asbestos, silica, and the effect of particle solubility.* Environmental science & technology, 2006. **40**(14): p. 4374-4381.

288. Zhu, Y., et al., *Rattle-Type Fe3O4@SiO2 Hollow Mesoporous Spheres as Carriers for Drug Delivery.* Small, 2010. **6**(3): p. 471-478.

289. Xu, H., et al., *Development of high magnetization Fe3O4/polystyrene/silica nanospheres via combined miniemulsion/emulsion polymerization.* Journal of the American Chemical Society, 2006. **128**(49): p. 15582-15583.

290. Fonner, J.M., et al., *Biocompatibility Implications of Polypyrrole Synthesis Techniques.* Biomedical materials (Bristol, England), 2008. **3**(3): p. 034124-034124.

291. Cui, X., et al., *In vivo studies of polypyrrole/peptide coated neural probes.* Biomaterials, 2003. **24**(5): p. 777-787.

292. Singh, N., et al., *NanoGenotoxicology: The DNA damaging potential of engineered nanomaterials.* Biomaterials, 2009. **30**(23–24): p. 3891-3914.

293. Simon, H.-U., A. Haj-Yehia, and F. Levi-Schaffer, *Role of reactive oxygen species (ROS) in apoptosis induction.* Apoptosis, 2000. **5**(5): p. 415-418.

294. Xiong, S., et al., *Size of TiO2 nanoparticles influences their phototoxicity: an in vitro investigation.* Archives of toxicology, 2013. **87**(1): p. 99-109.

295. Uchino, T., et al., *Quantitative determination of OH radical generation and its cytotoxicity induced by TiO 2–UVA treatment.* Toxicology in Vitro, 2002. **16**(5): p. 629-635.

296. Kim, S., et al., *Cytotoxicity of, and innate immune response to, size-controlled polypyrrole nanoparticles in mammalian cells.* Biomaterials, 2011. **32**(9): p. 2342-2350.

297. Song, M., et al., *The in vitro inhibition of multidrug resistance by combined nanoparticulate titanium dioxide and UV irradition.* Biomaterials, 2006. **27**(23): p. 4230-4238.

298. Pan, Y., et al., *Size-dependent cytotoxicity of gold nanoparticles.* Small, 2007. **3**(11): p. 1941-1949.

299. Nel, A., et al., *Toxic Potential of Materials at the Nanolevel.* Science, 2006. **311**(5761): p. 622-627.

300. Karlsson, H.L., et al., *Size-dependent toxicity of metal oxide particles—A comparison between nano- and micrometer size.* Toxicology Letters, 2009. **188**(2): p. 112-118.

301. Warheit, D.B., et al., *Pulmonary Instillation Studies with Nanoscale TiO2 Rods and Dots in Rats: Toxicity Is not Dependent upon Particle Size and Surface Area.* Toxicological Sciences, 2006. **91**(1): p. 227-236.

302. Fröhlich, E., *The role of surface charge in cellular uptake and cytotoxicity of medical nanoparticles.* Int J Nanomedicine, 2012. **7**: p. 5577-5591.

303. Suttiponparnit, K., et al., *Role of Surface Area, Primary Particle Size, and Crystal Phase on Titanium Dioxide Nanoparticle Dispersion Properties.* Nanoscale Res Lett, 2010. **6**(1): p. 27.

304. Liu, F., et al., *Synthesis, characterization, and application of Fe3O4@SiO2-NH2 nanoparticles.* RSC Advances, 2015. **5**(23): p. 18128-18136.

305. Bini, R.A., et al., *Synthesis and functionalization of magnetite nanoparticles with different amino-functional alkoxysilanes.* Journal of Magnetism and Magnetic Materials, 2012. **324**(4): p. 534-539.

306. Win, K.Y. and S.-S. Feng, *Effects of particle size and surface coating on cellular uptake of polymeric nanoparticles for oral delivery of anticancer drugs.* Biomaterials, 2005. **26**(15): p. 2713-2722.

307. Storm, G., et al., *Surface modification of nanoparticles to oppose uptake by the mononuclear phagocyte system.* Advanced drug delivery reviews, 1995. **17**(1): p. 31-48.

308. Huang, X., et al., *The Shape Effect of Mesoporous Silica Nanoparticles on Biodistribution, Clearance, and Biocompatibility in Vivo.* ACS nano, 2011. **5**(7): p. 5390-5399.

309. Giri, S., et al., *Stimuli-Responsive Controlled-Release Delivery System Based on Mesoporous Silica Nanorods Capped with Magnetic Nanoparticles.* Angewandte Chemie International Edition, 2005. **44**(32): p. 5038-5044.

310. Sill, T.J. and H.A. von Recum, *Electrospinning: applications in drug delivery and tissue engineering.* Biomaterials, 2008. **29**(13): p. 1989-2006.

311. Thevenot, P., et al., *SURFACE CHEMISTRY INFLUENCE CANCER KILLING EFFECT OF TiO(2) NANOPARTICLES.* Nanomedicine : nanotechnology, biology, and medicine, 2008. **4**(3): p. 226-236.

312. Nitin, N., et al., *Functionalization and peptide-based delivery of magnetic nanoparticles as an intracellular MRI contrast agent.* JBIC Journal of Biological Inorganic Chemistry, 2004. **9**(6): p. 706-712.

313. Yang, K., et al., *In Vitro and In Vivo Near-Infrared Photothermal Therapy of Cancer Using Polypyrrole Organic Nanoparticles.* Advanced Materials, 2012. **24**(41): p. 5586-5592.

314. Akagi, T., et al., *Protein direct delivery to dendritic cells using nanoparticles based on amphiphilic poly (amino acid) derivatives.* Biomaterials, 2007. **28**(23): p. 3427-3436.

315. Conover, C.D., et al., *Camptothecin delivery systems: the utility of amino acid spacers for the conjugation of camptothecin with polyethylene glycol to create prodrugs.* Anti-cancer drug design, 1999. **14**(6): p. 499-506.

316. Jang, H.D., et al., *Synthesis of SiO2 nanoparticles from sprayed droplets of tetraethylorthosilicate by the flame spray pyrolysis.* Current Applied Physics, 2006. **6, Supplement 1**: p. e110-e113.

317. Luttrell, T., et al., *Why is anatase a better photocatalyst than rutile? - Model studies on epitaxial TiO2 films.* Scientific Reports, 2014. **4**: p. 4043.

318. Kho, Y.K., et al., *Photocatalytic H2 evolution over TiO2 nanoparticles. The synergistic effect of anatase and rutile.* The Journal of Physical Chemistry C, 2010. **114**(6): p. 2821-2829.

319. Kavitha, R., S. Meghani, and V. Jayaram, *Synthesis of titania films by combustion flame spray pyrolysis technique and its characterization for photocatalysis.* Materials Science and Engineering: B, 2007. **139**(2–3): p. 134-140.

320. Jun, Y.-w., et al., *Nanoscale size effect of magnetic nanocrystals and their utilization for cancer diagnosis via magnetic resonance imaging.* Journal of the American Chemical Society, 2005. **127**(16): p. 5732-5733.

321. Aryal, S., et al., *Study of electrolyte induced aggregation of gold nanoparticles capped by amino acids.* Journal of colloid and interface science, 2006. **299**(1): p. 191-197.

322. Costa, D., L. Savio, and C.-M. Pradier, *Adsorption of Amino Acids and Peptides on Metal and Oxide Surfaces in Water Environment: A Synthetic and*

Prospective Review. The Journal of Physical Chemistry B, 2016. **120**(29): p. 7039-7052.

323. Jadhav, S.A. and R. Bongiovanni, *Synthesis and organic functionalization approaches for magnetite (Fe3O4) nanoparticles.* Adv Mat Lett, 2012. **3**(5): p. 356-361.

324. Szegedi, A., et al., *Effect of amine functionalization of spherical MCM-41 and SBA-15 on controlled drug release.* Journal of Solid State Chemistry, 2011. **184**(5): p. 1201-1207.

325. Mudunkotuwa, I.A. and V.H. Grassian, *Citric Acid Adsorption on TiO2 Nanoparticles in Aqueous Suspensions at Acidic and Circumneutral pH: Surface Coverage, Surface Speciation, and Its Impact on Nanoparticle−Nanoparticle Interactions.* Journal of the American Chemical Society, 2010. **132**(42): p. 14986-14994.

326. Murthy, V.S., et al., *Charge-Driven Flocculation of Poly(l-lysine)Gold Nanoparticle Assemblies Leading to Hollow Microspheres.* Journal of the American Chemical Society, 2004. **126**(16): p. 5292-5299.

327. Keskinen, H., et al., *Size-selected agglomerates of SnO2 nanoparticles as gas sensors.* Journal Of Applied Physics, 2009. **106**(8): p. -.

328. Rozenberg, M. and G. Shoham, *FTIR spectra of solid poly-l-lysine in the stretching NH mode range.* Biophysical chemistry, 2007. **125**(1): p. 166-171.

329. Bellamy, L.J., *The infrared spectra of complex molecules*. 1957, London: John Wiley and Sons.

330. Köppen, S., O. Bronkalla, and W. Langel, *Adsorption configurations and energies of amino acids on anatase and rutile surfaces.* The Journal of Physical Chemistry C, 2008. **112**(35): p. 13600-13606.

331. Hidaka, H., et al., *Fate of amino acids upon exposure to aqueous titania irradiated with UV-A and UV-B radiation Photocatalyzed formation of NH< sub> 3</sub>, NO< sub> 3</sub>< sup>−</sup>, and CO< sub> 2</sub>.* Journal of Photochemistry and Photobiology A: Chemistry, 1997. **108**(2): p. 197-205.

332. Ohtani, B., B. Pal, and S. Ikeda, *Photocatalytic Organic Syntheses: Selective Cyclization of Amino Acids in Aqueous Suspensions.* Catalysis Surveys from Asia, 2003. **7**(2): p. 165-176.

333. Palmisano, G., et al., *Photocatalysis: a promising route for 21st century organic chemistry.* Chemical Communications, 2007(33): p. 3425-3437.

334. Pal, B., et al., *Photocatalytic redox-combined synthesis of L-pipecolinic acid from L-lysine by suspended titania particles: effect of noble metal loading on the selectivity and optical purity of the product.* Journal of Catalysis, 2003. **217**(1): p. 152-159.

335. Hoffmann, N., *Photocatalysis with TiO2 applied to organic synthesis.* Australian Journal of Chemistry, 2015. **68**(11): p. 1621-1639.

336. da Silveira, E.F., et al., *Ketoprofen-loaded polymeric nanocapsules selectively inhibit cancer cell growth in vitro and in preclinical model of glioblastoma multiforme.* Investigational New Drugs, 2013. **31**(6): p. 1424-1435.

337. Gynther, M., et al., *Large Neutral Amino Acid Transporter Enables Brain Drug Delivery via Prodrugs.* Journal of medicinal chemistry, 2008. **51**(4): p. 932-936.

338. Bini, R.A., et al., *Synthesis and functionalization of magnetite nanoparticles with different amino-functional alkoxysilanes.* Journal of Magnetism and Magnetic Materials, 2012. **324**(4): p. 534-539.

339. Szymański, J., et al., *Diffusion and Viscosity in a Crowded Environment: from Nano- to Macroscale.* The Journal of Physical Chemistry B, 2006. **110**(51): p. 25593-25597.

340. Dipojono, H.K., I. Syafitri, and A.G. Saputro. *Immobilization of leucine on polypyrrole for biosensor applications: A density functional theory study*. in *Instrumentation, Communications, Information Technology, and Biomedical Engineering (ICICI-BME), 2009 International Conference on*. 2009: IEEE.

341. Shimoda, S. and E. Smela, *The effect of pH on polymerization and volume change in PPy(DBS).* Electrochimica Acta, 1998. **44**(2–3): p. 219-238.

342. Diaz, A.F., et al., *Electrooxidation of aromatic oligomers and conducting polymers.* Journal of Electroanalytical Chemistry and Interfacial Electrochemistry, 1981. **121**: p. 355-361.

343. Street, G., et al., *Preparation and characterization of neutral and oxidized polypyrrole films.* Molecular Crystals and Liquid Crystals, 1982. **83**(1): p. 253-264.

344. Birnbaum, D. and B.E. Kohler, *Electronic structure of thiophene and pyrrole dimers: 2, 2'-bithiophene, 2, 2'-thienylpyrrole, and 2, 2'-bipyrrole.* The Journal of Chemical Physics, 1991. **95**(7): p. 4783-4789.

345. Zotti, G., et al., *Well-defined pyrrole oligomers: Electrochemical and UV/vis studies.* Advanced Materials, 1992. **4**(12): p. 798-801.

346. Yakushi, K., et al., *Optical study of polypyrrole perchlorate.* The Journal of Chemical Physics, 1983. **79**(10): p. 4774-4778.

347. Rapta, P., et al., *In situ EPR/UV–VIS spectroelectrochemistry of polypyrrole redox cycling.* Journal of the Chemical Society, Faraday Transactions, 1998. **94**(24): p. 3625-3630.

348. Unsworth, J., et al., *The influence of electrolyte pH on the surface morphology of polypyrrole.* Synthetic metals, 1992. **53**(1): p. 59-69.

349. Meteleva-Fischer, Y.V., E. Von Hauff, and J. Parisi, *Electrochemical synthesis of polypyrrole layers doped with glutamic ions.* Journal of Applied Polymer Science, 2009. **114**(6): p. 4051-4058.

350. Sumayya, A., et al., *Vibrational spectroscopic studies and ab initio calculations of L-glutamic acid 5-amide.* RJC Rasayan J. Chem, 2008. **1**(3): p. 548-555.

351. Parikh, S.J., et al., *Evaluating glutamate and aspartate binding mechanisms to rutile (α-TiO2) via ATR-FTIR spectroscopy and quantum chemical calculations.* Langmuir : the ACS journal of surfaces and colloids, 2011. **27**(5): p. 1778-1787.

352. Vishnuvardhan, T., et al., *Synthesis, characterization and ac conductivity of polypyrrole/Y2O3 composites.* Bulletin of Materials Science, 2006. **29**(1): p. 77-83.

353. Omastová, M., et al., *Synthesis and structural study of polypyrroles prepared in the presence of surfactants.* Synthetic metals, 2003. **138**(3): p. 447-455.

354. Blinova, N.V., et al., *Polyaniline and polypyrrole: A comparative study of the preparation.* European Polymer Journal, 2007. **43**(6): p. 2331-2341.

355. Tabačiarová, J., et al., *Study of polypyrrole aging by XPS, FTIR and conductivity measurements.* Polymer Degradation and Stability, 2015. **120**: p. 392-401.

356. Eisazadeh, H., *Studying the characteristics of polypyrrole and its composites.* World journal of Chemistry, 2007. **2**(2): p. 67-74.

357. Chitte, H.K., et al., *Synthesis of Polypyrrole Using Ammonium Peroxy Disulfate (APS) as Oxidant Together with Some Dopants for Use in Gas Sensors.* Materials Sciences and Applications, 2011. **Vol.02No.10**: p. 9.

358. Chen, A., H. Wang, and X. Li, *Influence of concentration of FeCl3 solution on properties of polypyrrole–Fe3O4 composites prepared by common ion absorption effect.* Synthetic metals, 2004. **145**(2–3): p. 153-157.

359. Chen, M., et al., *Polypyrrole nanoparticles for high-performance in vivo near-infrared photothermal cancer therapy.* Chemical Communications, 2012. **48**(71): p. 8934-8936.

360. Maitland, D., et al., *Controlling the resolution and duration of pulsatile release from injectable magnetic 'plum-pudding'nanocomposite hydrogels.* RSC Advances, 2016. **6**(19): p. 15770-15781.

361. Leprince, L., et al., *Dexamethasone electrically controlled release from polypyrrole-coated nanostructured electrodes.* Journal of Materials Science: Materials in Medicine, 2010. **21**(3): p. 925-930.

362. Esrafilzadeh, D., et al., *Multifunctional conducting fibres with electrically controlled release of ciprofloxacin.* Journal of Controlled Release, 2013. **169**(3): p. 313-320.

363. Wang, Y., et al., *Multifunctional mesoporous silica-coated graphene nanosheet used for chemo-photothermal synergistic targeted therapy of glioma.* Journal of the American Chemical Society, 2013. **135**(12): p. 4799-4804.

364. Rogers, H.B., et al., *Exploiting Size-Dependent Drag and Magnetic Forces for Size-Specific Separation of Magnetic Nanoparticles.* International journal of molecular sciences, 2015. **16**(8): p. 20001-20019.

Appendices

1. Titration of TiO_2

As-prepared TiO_2 NPs and lysine-functionalised TiO_2 NPs (prepared in acidic conditions) were titrated in order to find their isoelectric points (Figure A1) The isoelectric point occurred at 3.5 for as-prepared TiO_2.

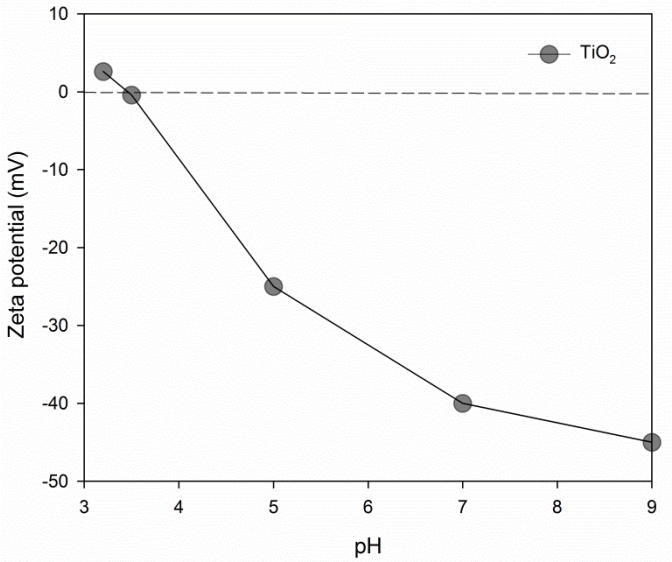

Figure A1. Titration of TiO_2 and lysine-TiO_2 NPs to determine their isoelectric points.

2. Injection of FITC-lys-TiO_2 materials into neurons for imaging and excitation

The FITC-conjugated lysine-functionalised TiO_2 NPs created in ***Chapter 2*** were then injected into a neuron for imaging to prove that they are compatible with living cells. It was found that the optimisation procedure established (using acidic pH, optimising the lysine concentration and reaction time) significantly improve the fluorescence of the injected particles (Figure A2 b), as expected, compared against the lysine-functionalised TiO_2 synthesised at non-optimal conditions (Figure A1 a). This significant difference in apparent fluorescence of the nanoparticles is attributed to the dual factors of greater overall $–NH_2$ content of the optimised structure along with its smaller overall particle size that allows for larger surface area for the dye conjugation and greater ability to diffuse through the cell.

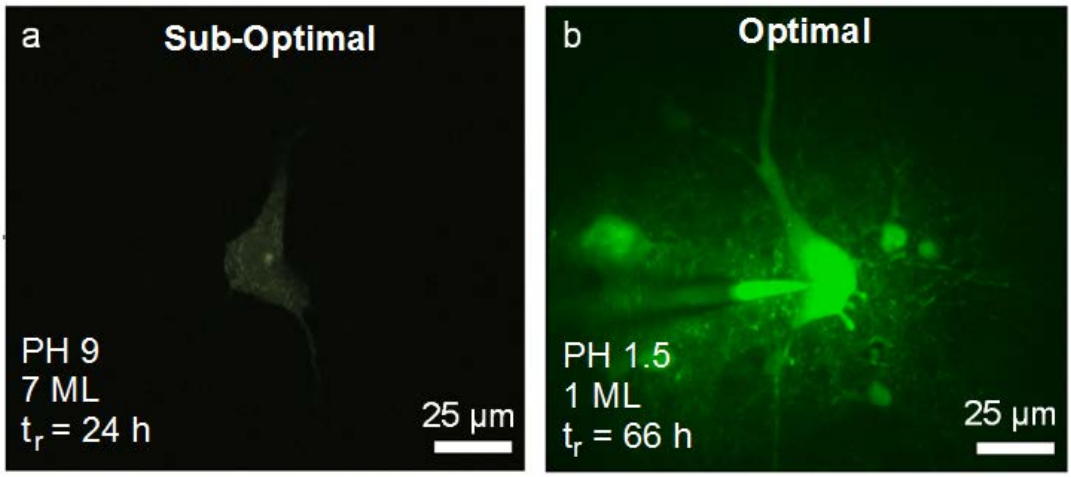

Figure A2. Microscope images of (a) sub-optimal and (b) optimal FITC-lys-TiO_2 nanoparticles injected in a neuron displaying fluorescence.

3. *Calibration curves for Fluorescamine assay of L-glutamic acid and L-lysine*

The Fluorescamine assay procedure was calibrated for reaction with L-glutamic acid and L-lysine standards at various pH. The following curves were produce and used for concentration estimates (Figure A3) which were performed at pH 7.6 (green line).

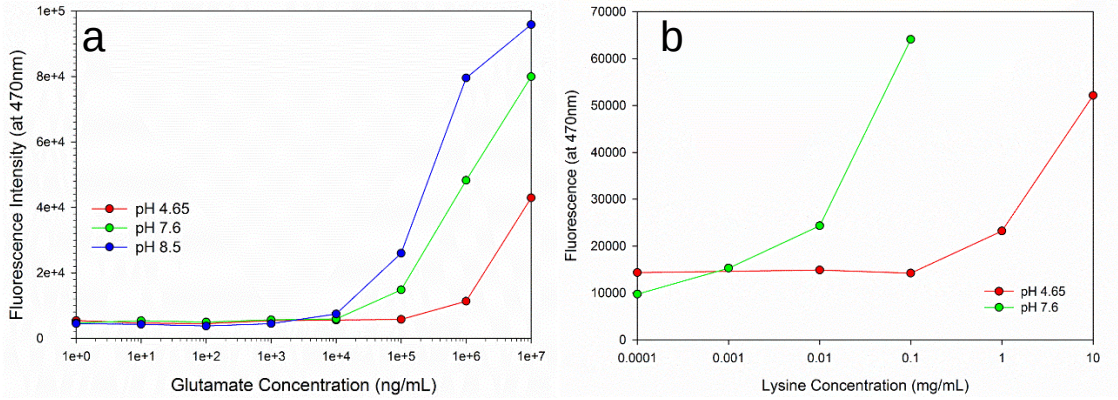

Figure A3. Calibration curves for reaction of Fluorescamine against standard concentrations of (a) L-glutamic acid and (b) L-lysine at pH 4.65 (red line), pH 7.65 (green line) and pH 8.5 (blue line).

4. *Magnetic alignment setup*

A schematic of the experimental setup for the magnetically aligned synthesis of anistropic Fe_3O_4 filaments is given below (Figure A4). It was found that a stirring plate is required to maintain dispersion of the particles during synthesis.

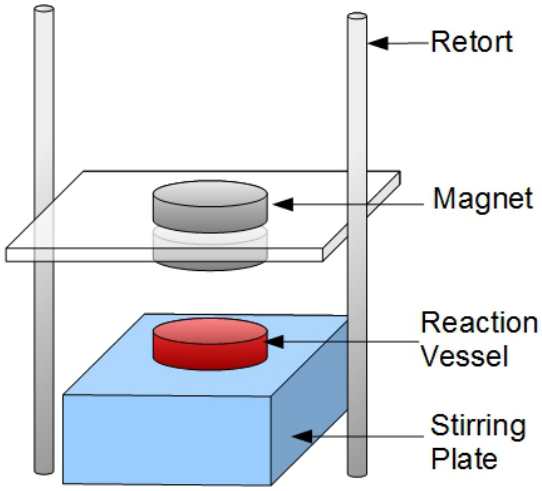

Figure A4. Schematic experiment setup of magnetically aligned synthesis of anisotropic Fe_3O_4 filaments.

5. *Derivation of nanoparticle motion under an applied magnetic field*

The force on the iron oxide agglomerate can be derived from (S1) considering the driving magnetic force (S2) applied at a certain distance from a cylindrical magnet and counterbalanced by the drag force (S4).

$$F = \rho V \vec{a} = \overrightarrow{F_m} + \overrightarrow{F_s} \quad \text{(S1)}$$

Where ρ = density of agglomerate; V = volume of the agglomerate.

F_m is the magnetic force, given as follows:

$$F_m = \frac{V\chi}{\mu}\left(\overrightarrow{B} \cdot \nabla\right)\vec{B} \quad \text{(S2)}$$

Where μ = permittivity of medium; χ = magnetic susceptibility of the iron oxide.

The magnetic field, B, for a cylindrical magnet is given:

$$\vec{B} = -\frac{\mu m}{4\pi x^2} \quad \text{(S3)}$$

Where x = distance from the magnet; m = strength of the magnet.

The drag force, Fs, is defined as:

$$F_s = -6\pi\eta r\vec{v} \tag{S4}$$

Where η = dynamic viscosity; r = radius of agglomerate; v = velocity of agglomerate.

Substituting (S2), (S3), (S4) into (S1), we arrive at (S5)

$$\rho V\vec{a} = \frac{\chi V}{\mu}\left(\vec{B}\cdot\nabla\right)\vec{B} - 6\pi\eta r\vec{v} \tag{S5}$$

Performing the differentiation and approximating agglomerates as perfect spheres of radius r yields the following relation.

$$\frac{\rho 4\pi r^3}{3}\vec{a} = \frac{\chi 4\pi r^3}{\mu}\left(\frac{\mu^2 m^2}{8\pi^2 x^5}\right) - 6\pi\eta r\vec{v} \tag{S6}$$

This can be rearranged into the following first order differential equation

$$\vec{a} = \frac{d\vec{v}}{dt} = -\frac{r\chi\mu m^2}{6\pi x^5} - \frac{18\eta\vec{v}}{4r^2} \tag{S7}$$

This can be solved in the following form

$$\frac{dv}{dt} + \beta v = \alpha \tag{S8}$$

$$v = \alpha + Ce^{-\beta t} \tag{S9}$$

Where

$$\beta = -\frac{18\eta}{4r^2} \tag{S10}$$

$$\alpha = -\frac{r\chi\mu m^2}{6\pi x^5} \tag{S11}$$

This leads to

$$v = Ce^{-\frac{18\eta}{4r^2}t} + \frac{3\chi\mu m^2}{8\pi^2 x^5\rho} \tag{S12}$$

Where C is the integration constant.

Combining (S12) and (1), the collision frequency of agglomerates (2) in the direction of the perpendicular applied field may be computed. Note that for r = 100nm, the exponential term approaches 0 and may be neglected.

$$v \sim \frac{3\chi\mu m^2}{8\pi^2 x^5 \rho} \quad \text{(S13)}$$

Applying conditions $\chi = 0.1$, $\mu = 710^{-12}$ $C^2N^{-1}m^{-2}$, m =1 T , x = 0.01 m, ρ=1000 kg m^3 yields

$$v \sim 0.0003\ m/s \quad \text{(S14)}$$

The Peclet number can then be computed for the system:

$$Pe = \frac{vr}{D} \quad \text{(S15)}$$

Where D is the diffusion coefficient, given by Stokes-Einstein equation:

$$D = \frac{k_B T}{6\pi\eta r} \quad \text{(S16)}$$

Where k_B = Boltzmann constant

Substituting r = 100nm as a characteristic length scale, Pe ~ 22. Thus, this system is in the ballistic regime. Diffusion of the nanoparticles may be neglected. Therefore, the final expression for the collision frequency is simply stated as:

$$Z_{AB} = 4N_A N_B r^2 \pi \left(Ce^{-\frac{18\eta}{4r^2}t} + \frac{3\chi\mu m^2}{8\pi^2 x^5 \rho} \right) \quad (2)$$

6. Dynamic conductivity of PPy-Fe_3O_4 filaments at variable magnetic rotation speeds

In Chapter 5, the strong directional dependence of the PPy-Fe_3O_4 filaments was observed in the static situation of a sample of filaments that were allowed to dry on the electrode arrays. Some initial experiments on recording the conductivity of the filaments while wet under a rotating magnetic field seem to indicate that this directionality can also be observed in a dynamic system. The i-t curves (Figure A5) showed a periodic behaviour that is consistent with the rotation frequency. Although these results have no direct application in this thesis, they have been included in appendices in the hope that they will inspire future work on the dynamically tuneable conductivity of PPy-Fe_3O_4 filaments.

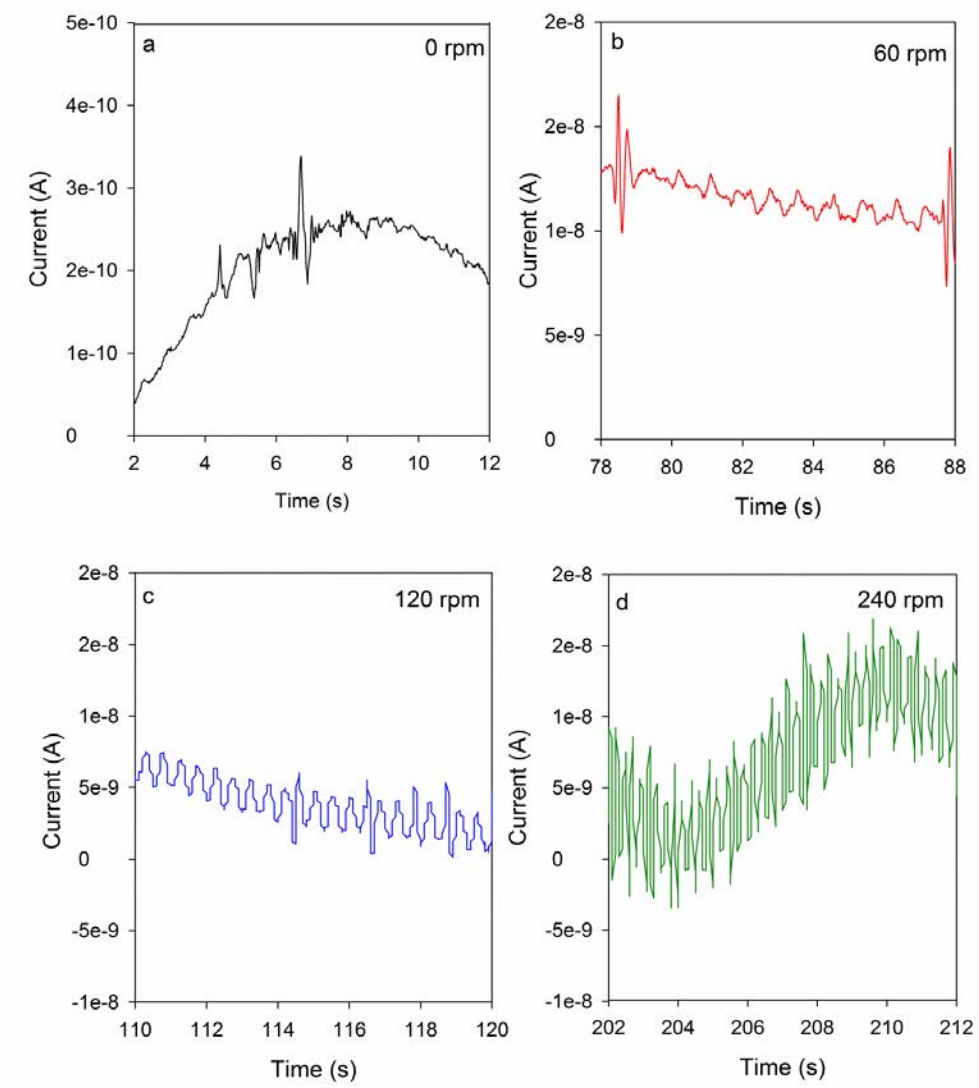

Figure A5. Recorded i-t curves for PPy-Fe_3O_4 filaments suspended in water with a dynamic rotating magnetic field at (a) 0, (b) 60, (c) 120) and (d) 240 rpm.

7. Supplementary Videos V1 and V2

Video footage showing rotation of the microfilaments (V1) and randomly shaped agglomerates (V2) has been included in the attached file.

In the case of file corruption, the supporting videos can be downloaded at:

https://www.dropbox.com/s/0dyewlm5uajk8ea/Thesis%20Supplementary%20Videos.zip?dl=0